Technische Universität München

Excellence Cluster Universe

The link between galaxy morphology and star formation activity and its evolution

Laura Morselli

Vollständiger Abdruck der von der Fakultät für Physik der Technischen Universität München zur Erlangung des akademischen Grades eines

Doktors der Naturwissenschaften (Dr. rer. nat.)

genehmigten Dissertation.

Vorsitzender:		Prof. Dr. Björn Garbrecht
Prüfer der Dissertation:	1.	Prof. Dr. Elisa Resconi
	2.	Prof. Dr. Sherry Suyu

Die Dissertation wurde am 16.01.2018 bei der Technischen Universität München eingereicht und durch die Fakultät für Physik am 12.03.2018 angenommen.

To my family

Contents

List of Figures

List of Tables

Tante cose ho imparato da voi uomini... Ho imparato che tutti quanti vogliono vivere sulla cima della montagna, senza sapere che la vera felicitá sta nel come questa montagna é stata scalata. Ho imparato che quando un bambino appena nato stringe con il suo piccolo pugno, per la prima volta, il dito del padre, lo racchiude per sempre. Ho imparato che un uomo ha diritto a guardarne un altro dall'alto solo per aiutarlo ad alzarsi.

Gabriel Garcia Marquez

1 A framework for galaxy formation and evolution

In the northern hemisphere, the night sky is riddled with specks of light of varying colours. Most of these points are stars belonging to the galaxy where our Solar System is located: the Milky Way. In the southern hemisphere two extended concentrations of stars are visible with the naked eye. They are systems outside our Galaxy: the Small Magellanic Cloud and the Large Magellanic Cloud. For long humans believed that the Milky Way was the only galaxy in the Universe. At the end of the 18th century, the first catalogue of nebulae (diffuse celestial objects) appeared. The author of the catalogue, Charles Messier, still believed that nebulae were objects belonging to the Milky Way. In the following decades, the number of observed nebulae increased steeply, and the first distinctions based on their shape were made. Only at the beginning of the 20th century, spectroscopic studies and measurements of the luminosity of nebulae revealed that some of them were moving away from the Earth and were characterised by a weaker luminosity with respect to the typical luminosity of nebulae closer to the Earth. Edwin Hubble interpreted nebulae properties to conclude that they were sources outside the Milky Way. Due to that interpretation, together with the work of several astronomers, the idea of multiple galaxies in the Universe started spreading.

Nowadays it is well known that galaxies characterise the largest part of the Universe's history. Galactic structures, in fact, are observed up to redshift ≈ 11, when the Universe was only 3% of its current age (Oesch et al., 2016). Latest studies estimate that in the Universe there are approximately 2 trillion galaxies (Conselice et al., 2016). Fig. 1.1 shows the deepest-ever image of the Universe, taken with the Hubble Space Telescope: the Hubble eXtreme Deep Field (Illingworth et al., 2013). This image, taken with more than 500 observing hours, contains approximately 5,500 galaxies, in an area that has a diameter one tenth that of the Moon. In the next Sections, an overview of the knowledge gained so far on galaxies will be given: from their formation, that necessarily needs to be considered in a cosmological context, to their properties in the local Universe and their evolution across cosmic time.

Figure 1.1: The Hubble eXtreme Deep Field (XDF), the deepest-ever view of the Universe. This image alone contains about 5,500 galaxies. The faintest sources are one ten-billionth the minimum brightness observable by the human eye. [Credit: www.nasa.gov]

1.1 Galaxy Formation

A galaxy is defined as a gravitationally bound system made of stars, stellar remnants (e.g. neutron stars, white dwarfs and black holes), gas in different phases (cold, warm and hot) that constitutes the so called interstellar medium (ISM), dust grains, and of course, dark matter (DM). To be able to summarise the current knowledge on how galaxies form, it is necessary to introduce the cosmological framework in which this happens, since cosmology provides initial conditions for structure formation.

1.1.1 The cosmological framework

In the current cosmological picture, the ΛCDM model, the Universe in which the Milky Way is located is an expanding space-time originated $\sim$ 13.7 billion years ago from a singularity: the Big Bang. The Universe has the property of being *homogenous* and *isotropic* (Cosmological Principle) and is governed by Einstein's Theory of General Relativity. The ΛCDM Universe is composed of dark energy (the vacuum energy density associated to the cosmological constant Λ), cold dark matter (CDM), baryonic matter, and radiation. The temperature of the Universe is a monotonically decreasing function of time (with t = 0 corresponding to the Big Bang), and is estimated to have been larger than 10^{12} K immediately after the initial singularity. The "luminous" matter, observed as stars and galaxies, formed in large majority $\approx$ 200 seconds after the Big Bang, during the primordial nucleosynthesis that took place when the temperature dropped to 10^9 K (Alpher et al., 1948; Gamow, 1948). At early stages, matter was fully ionised and coupled with radiation resulting in the two components having the same temperature. When the characteristic timescale for collisions between photons and neutral hydrogen atoms becomes smaller than the Hubble expansion time (age of the Universe), the H and He atoms recombine, and matter and radiation decouple. Prior to decoupling, photons were continuously scattered. After experiencing the last scattering event, photons can then travel within the Universe now transparent to radiation. These photons are referred to as cosmic radiation background (CMB), that at the time of discovery (Penzias & Wilson, 1965) played a major role in validating the Big Bang model. In fact, the CMB can be interpreted as the afterglow radiation left over from the hot Big Bang, and the tiny fluctuations in its temperature carry the information on how galaxies form.

The Universe is mathematically described by the Einstein Field Equation (EFE), that binds the geometry of the space-time and its matter content:

$$R_{\mu\nu} - \frac{1}{2} R g_{\mu\nu} + \Lambda g_{\mu\nu} = \frac{8\pi G}{c^4} T_{\mu\nu}, \tag{1.1}$$

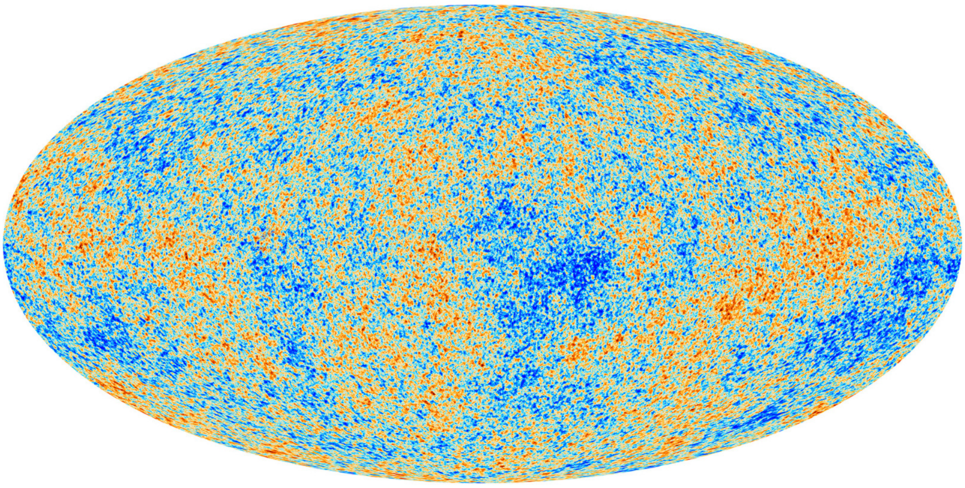

Figure 1.2: CMB temperature map, as measured by the Planck satellite. Different colours correspond to tiny differences in temperature. [Credit: www.esa.int]

where $R_{\mu\nu}$ is the Ricci curvature tensor, R is the scalar curvature, $g_{\mu\nu}$ is the metric tensor, Λ is the cosmological constant, G is the Newton's gravitational constant, c is the speed of light in vacuum, and $T_{\mu\nu}$ is the stress-energy tensor. The space-time is described by the Robertson-Walker metric (Peacock, 1999):

$$ds^2 = (cdt)^2 - a(t)^2\Big[\frac{dr^2}{1-K^2} + r^2(d\theta^2 + sin^2\theta d\phi^2)\Big] \tag{1.2}$$

where r, θ, and ϕ are spherical comoving coordinates, t is the proper time, and K is the curvature parameter, that can have values -1, 0, 1, corresponding to an open (hyperbolic), a flat (euclidean), or a closed (spherical) space-time geometry. The solution of the EFE in the case of a Robertson-Walker metric for a fluid with pressure p and density ρ is the Friedmann equation:

$$\left(\frac{\dot{a}}{a}\right)^2 = \frac{8\pi G}{3}\rho - \frac{Kc^2}{a^2} + \frac{\Lambda c^2}{3} \tag{1.3}$$

where a is the scale factor of the Universe that relates physical and comoving coordinates. In particular, if R_0 is the distance at the reference time t_0, $R(t)$ is the proper distance at the time t, and z is the redshift at time t, then:

$$a(t) = \frac{R(t)}{R_0} = \frac{1}{1+z(t)} \tag{1.4}$$

The Hubble parameter, related to the scale factor, is defined as the rate of change in time of the proper distance between two points:

$$H(t) = \frac{\dot{a}(t)}{a(t)} \tag{1.5}$$

The Hubble parameter computed at $t = t_0$ is called the Hubble constant H_0.

A solution to the Friedman equation can be obtained by specifying an equation of state for the fluid and combining it with the cosmological principle and the first law of thermodynamics. This leads to expressions describing the time evolution of ρ, P and T. By expressing the total density of the Universe in terms of its contributors, i.e. matter ρ_m, radiation ρ_r, and cosmological constant ρ_Λ, Eq.1.3 becomes:

$$\left(\frac{\dot{a}}{a}\right)^2 = \frac{8\pi G}{3}\left[\rho_{m,0}\left(\frac{a_0}{a}\right)^3 + \rho_{r,0}\left(\frac{a_0}{a}\right)^4 + \rho_{\Lambda 0}\right] - \frac{Kc^2}{a^2} \tag{1.6}$$

where the subscript 0 refers to the quantities estimated at $t = t_0$. Eq. 1.6 expresses the time evolution of the expansion of the Universe as a function of its density at $t = 0$ and curvature. Thus, it is now possible to study the evolution of density perturbations in to galaxies observed today.

1.1.2 Density perturbations and their growth

In the ΛCDM framework, structure formation results from gravitational instabilities which grow from density fluctuations in a quasi-homogeneous Universe. Density fluctuations are described as:

$$\delta\rho = \frac{\rho}{\bar{\rho}} \tag{1.7}$$

where $\bar{\rho}$ is the average density and ρ is the local density value. The origin of density perturbations is believed to reside in quantum fluctuations that generate Gaussian density perturbations with a scale invariant power spectrum. The time evolution of density perturbations is the key to understanding how instabilities grow and results in the observed galaxy population. In general, the evolution of $\delta\rho$ can be divided into two regimes. The phase that begins with $\delta\rho << 1$ and proceeds till $\delta\rho \sim 1$ is the so-called **linear regime**, when non-linear terms in the set of equations describing the time evolution can be neglected. When $\delta\rho \sim 1$, the approximation of linear-regime is no longer valid and the growth of fluctuation enters the **non-linear regime**. In the past years, thanks to observations made with Cosmic Background Explorer (COBE), the Wilkinson Microwave Anisotropy Probe (WMAP) and the Planck satellites, the existence of primordial fluctuations of the order of 10^{-5} in the CMB temperature map, shown in Fig. 1.2, has been confirmed.

These temperature fluctuations are believed to trace perturbations in the density of matter in the early Universe. Thus, at early stages, the growth of density perturbations can be studied in linear regime, using a set of equations that describe the evolution of a fluid in a gravitational field: the continuity equation (conservation of mass), the Euler equation (conservation of momentum), and the Poisson equation (to describe the potential). Solving such equations reveals the existence of a characteristic scale length λ_J and an associated mass M_J, called the Jeans length and the Jeans mass, respectively. Only perturbations on scales larger than λ_J and mass larger than M_J can collapse under gravity, in a typical time scale that is called *free-fall time*. Nevertheless, observations of primordial fluctuations of the order of 10^{-5}, together with the observation that at $z = 0$ $\delta >> 1$, reveal that, at some point in the history of the Universe, perturbations must have entered the non-linear regime.

To understand non-linear growth of perturbations, numerical methods are used, with some assumptions regarding the initial symmetry. In the *spherical top hat approximation* overdensities are spherically symmetric and evolve in accordance to the Friedman equation. In this case, the growth of perturbations occurs in two phases: initially, it expands as the Universe expands till it reaches a critical density δ_c that marks the onset of collapse and subsequent virialization. For all realistic cosmogonies, the result of the spherical approximation is $\delta_c \approx 1.686$. The virialized system, that is the end product of the spherical collapse, is governed by collisionless dynamics, a good assumption for dark matter halos and galaxies.

Thus far, the evolution of a single perturbation has been discussed. However, the birth of structures in the Universe is the result of perturbations that exist at different scales and masses. Hence, it is useful to approach the problem of perturbation growth in a statistical sense. The appropriate tool is a power spectrum $P(k)$, characterised by its variance, probability distribution and correlation functions. Inflation models for an isotropic and homogeneous Universe predict $P(k) \propto k^n$ (Guth, 1981; Guth & Pi, 1982), where n is called spectral index. In this formulation, k is the wave vector corresponding to the plane wave that represents a perturbation. The variance, σ^2, represents the amplitude of perturbations, but not their spatial extent. The probability distribution is generally assumed to be Gaussian (as motivated by inflation Guth & Pi, 1982; Brandenberger, 1985). The $n = 1$ power spectrum, called Harrison-Zeldovich approximation or scale-invariant spectrum (Harrison, 1970; Zeldovich, 1972), has always been considered the most natural choice for initial fluctuations. The spectral index can be estimated from the CMB map. The latest estimate of the spectral index is $n = 0.968 \pm 0.006$ (Planck Collaboration et al., 2015), with no evidence for significant changes as a function of the scale k at which n is estimated.

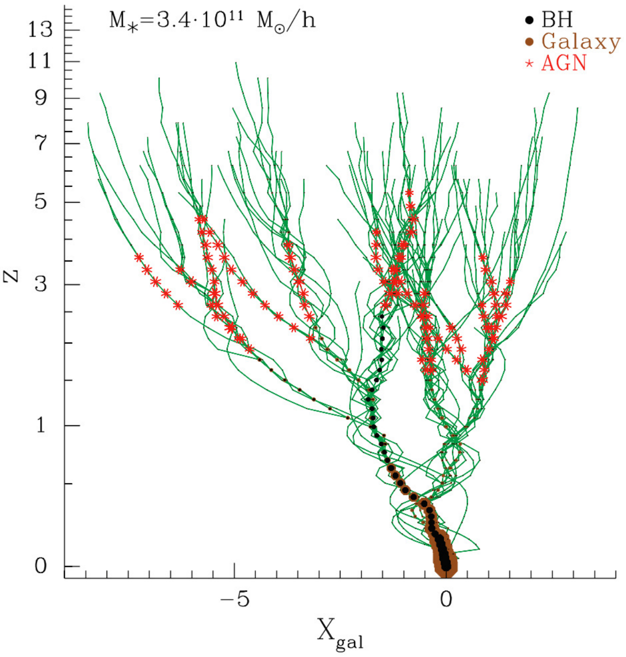

Figure 1.3: A typical galaxy merger tree that represents the hierarchical fashion of structure formation, where smaller units merge together to form more massive ones. From Marulli et al. (2009).

The knowledge of the shape of the initial fluctuation spectrum, together with the growth of perturbations over cosmic time and their amplitude at the last scattering surface are the necessary conditions to understand how the first collapsed structures appear in the Universe.

1.1.3 First collapsed structures

The first collapsed structures that are the result of the grow of initial fluctuations are dark matter halos (DMH). DM is, according to the ΛCDM model, the dominant matter component of the Universe, and it decouples from radiation at a redshift larger than the one at which the decoupling between baryonic matter and radiation occurs. Immediately after the decoupling of dark matter and radiation, the Jeans mass for the matter component is: $M_{J,CDM} \approx 10^6$ M$_\odot$. This result hints towards a hierarchical DMH growth process in order to explain the massive $10^{13} - 10^{15}$ M$_\odot$ DMHs of galaxies and clusters present in the Universe today. This hierarchical pathway (bottom-up scenario) is well described by the merger tree representation shown in Fig. 1.3, where less massive objects merge together to form more massive ones. The mass function of DMHs in the case of spherical collapse is the so-called Press & Schechter (1974):

$$n(M;t)dM = \sqrt{\frac{2}{\pi}}\frac{\rho_0}{M^2}\frac{\delta_c(t)}{\sigma(M)}|\frac{dln\sigma}{dlnM}| \times exp\left[-\frac{\delta_c^2(t)}{2\sigma^2(M)}\right] dM \qquad (1.8)$$

where ρ_0 is the average mass density of the DMH, δ_c(t) is the critical density at time t and $\sigma(M)$ is the dispersion in mass of the perturbation.

Eq. 1.8 predicts the number of collapsed DMH per unit mass per unit volume. Post collapse, a DMH reaches a state of virial equilibrium characterised by a virial temperature, defined as:

$$T_v \approx 2 \times 10^4 M_{h,8}^{2/3}(1+z)/10[K] \qquad (1.9)$$

where $M_{h,8}$ is the halo mass in unit of 10^8 $M_\odot$. The virial temperature of a DMH has important consequences on the efficiency of baryonic mass to collapse and form protogalaxies.

1.1.4 Galaxy formation

Luminous objects form by the infall of baryonic matter into dark matter halos. The study of growth of baryonic perturbations is complicated by the necessary addition of radiative processes (shock heating, pressure gradients, cooling) that are of extreme importance in understanding the existence of characteristic scales in the mass spectrum of galaxies (a property that cannot be explained by gravity alone; see Binney, 1977; White & Rees, 1978; Rees & Ostriker, 1977; Silk, 1977) . Briefly, during infall in dark matter haloes, the baryonic gas is shock-heated at the virial temperature of the halo through violent relaxation. Typical virial temperatures are $T_V > 10^4 K$, thus the gas in the halo gets ionised. Subsequently, the gas cools radiatively through emission of radiation that accompanies de-excitation. The virial temperature of DMH, T_v, sets the cooling efficiency of the baryonic gas and hence the level of fragmentation and final mass of the collapsed baryonic object. When $T_v > 10^7$ K, the baryonic gas is fully ionised and cools mainly through Bremsstrahlung emission from free electrons. For $10^4 K < T_v < 10^6$ K, several excitation and de-excitation processes, depending on the chemical composition of the gas, drive the cooling. At $T_v < 10^4$ K gas is mainly neutral and thus the cooling is suppressed. The cooling process is characterised by a cooling timescale, t_{cool}, that in the case of an ideal, monotonic gas is:

$$t_{cool} = \frac{3nk_B}{2n_H^2\Lambda(T)}, \qquad (1.10)$$

where Λ is the cooling function of the gas, n is the number density of gas particles. When $t_{cool} > t_H$ (where t_H is the age of the Universe) cooling is not important and gas is thus in hydrostatic equilibrium (when not perturbed). When $t_{ff} < t_{cool} < t_H$ (where t_{ff} is the free-fall time, describing the timescale at which a gas cloud collapses in absence of pressure) the gas that underwent contraction following cooling has sufficient time to restore hydrostatic equilibrium. Only when $t_{cool} < t_{ff}$ the gas experiences catastrophic cooling. When gas accumulates in regions where self-gravity dominates over the gravity of the host halo, fragmentation into smaller clumps takes place during catastrophic cooling, giving birth to stars and protogalaxies (e.g. Hensler & Burkert, 1989; Meier & Sunyaev, 1979; Peebles, 1984). In particular, as DMH do not have a uniform density distribution, the cooling radius was introduced, defined as the radius at which $t_{cool} = t_{ff}$. Catastrophic cooling happens when $r_{cool} >> r_{vir}$ (where r_{vir} is the virial radius of the SMH), in a regime of so-called *cold mode accretion.* When $r_{cool} << r_{vir}$ cooling happens only in the inner part of the halo, and hot gas will be found in the outer radii; as the new accreted gas will be shock-heated at T_V, this regime is called *hot mode accretion.* The requirement on the ratio between t_{cool}, t_H and t_{ff} naturally sets an upper limit to the masses of galaxies that can form (White & Rees, 1978). More massive galaxies form during mergers of less massive units. Such merging events are a natural consequence of the bottom up structure formation scenario.

The first protogalaxies appear in the Universe at $z \approx 20 - 30$ (Tegmark et al., 1997). The subsequent evolution of the galaxy is impacted by the growth of the host halo, and processes related to the life cycle of stars (energy feedback, winds, supernovae explosions). Energetic outputs from supermassive black holes hosted at the centre of galaxies are also believed to play a key role in galaxy evolution. In addition, galaxy mergers can significantly boost the star formation activity and are responsible for morphological changes in the structure of galaxies. In the next sections, the general properties of galaxies will be discussed, together with the current picture of galaxy evolution.

1.2 Properties of galaxies

This section presents an overview of galaxies' properties, focusing particularly on observational results. This brief summary is a result of decades of work that has progressively improved thanks to significant advancements in the available instrumentation (from naked eye observations, to photographic plates, to CCDs). These advancements lead to an increase in the number of observed galaxies and in the quality of the data.

1.2.1 Morphological classification of galaxies

Once the existence of galaxies beside the Milky Way became an accepted idea, one of the first properties to be studied by astronomers was the shape of the galaxies, or their morphology. In fact, galaxies appear in a variety of shapes, but can be broadly divided into four main morphological families: spirals, ellipticals, lenticulars, and irregulars.

Ellipticals
Elliptical galaxies are systems supported by velocity dispersion instead of rotation. They can be spherical, oblate, prolate, and triaxial, depending on the ratio between the three axes. Their surface brightness profile is smooth, and the shape of the isophotes can be used to further classify ellipticals into disky or boxy. Stellar populations in elliptical galaxies are generally old, and the vast majority of ellipticals show no-ongoing star formation activity. Two main scenarios for the formation of ellipticals have been discussed in literature: the monolithic collapse and mergers. In the monolithic scenario, ellipticals form violently on short timescales from the collapse and virialization of an uncollapsed system. In this scenario, a single burst of star formation occurs simultaneously with the collapse of the gas (Partridge & Peebles, 1967; Larson, 1975). The second scenario (Toomre, 1977) assumes that star formation occurs only in discs, and that it is the merger of disk galaxies that creates an elliptical. Kauffmann et al. (2003) showed that the observed properties of ellipticals are well reproduced by the merger scenario-the currently adopted paradigm for the formation of ellipticals.

Spirals
Spiral galaxies can be generalised as highly flattened discs supported by rotation. They form via the dissipational collapse of a gas cloud in a dark matter halo. The central component, i.e. the bulge, can be absent or more-or-less pronounced, barred or unbarred. Also, the number of arms and how tightly wound they are can vary, dividing spirals in *grand design* (2 arms), *multiple-arm* ($>$ 2 arms), or *flocculent* (no defined arms). The surface brightness profile of the disc, that contains

gas, stars, and dust, can be well approximated with a single exponential. However, the disk can be divided into two components: the *thick* and the *thin* disc, with different scale heights and stellar populations (Seth et al., 2005). The bulge, when present in the central part of a spiral galaxy, is in general populated by older stellar populations with respect to the ones in the disc, and has significantly lower dust and gas fractions. Bulges are mainly observed in two forms. *Classical bulges* are generally spherically symmetric, pressure-supported systems, that resemble giant ellipticals on smaller scales (de Vaucouleurs, 1958; Andredakis & Sanders, 1994; Kormendy, 2013). They are thought to form in mergers of galaxies with different propertied as compared to the ones that form ellipticals (Kormendy & Fisher, 2008; Hopkins et al., 2010). *Pseudobulges*, on the other hand, show disc-like features: they are rotationally supported systems with close to exponential surface brightness profiles, populated by young stellar populations. They form as a result of secular evolution of galactic discs, when non-axisymmetric structures (i.e. bars) re-distribute energy and momentum, thereby re-arranging the disk structure (e.g. Kormendy, 1993; Croton et al., 2006; Kormendy & Fisher, 2008; Athanassoula, 2008; Combes, 2009; Weinzirl et al., 2009; Governato et al., 2009; Scannapieco et al., 2010; De Lucia et al., 2011; Guo et al., 2011).

Lenticular and Irregular galaxies

Lenticular galaxies are similar to spiral galaxies with a large bulge component, with the exception that their discs have no visible spiral arms and are populated by older stars. They are thought to be faded spirals, i.e. spirals that used up all their available gas (Elmegreen et al., 2002; Blanton & Moustakas, 2009; Rizzo et al., 2017). Other results in literature suggest that they could also originate from mergers (Rudick et al., 2010; Mihos et al., 2013; Querejeta et al., 2015). Finally, galaxies that have no particular shape are called Irregulars, and are thought to constitute $\sim 20\%$ of the entire population of galaxies. They are mostly small structures, rich in gas, dust and young stellar populations. The Large and Small Magellanic Clouds, visible in the southern hemisphere with the naked eye, are examples of irregular galaxies.

Classifications

The most famous galaxy classification scheme is the one made by Hubble (1936): the Hubble Sequence of Galaxies, or *tuning fork diagram*, shown in Fig. 1.4. The Hubble Sequence classifies galaxies in the four broad classes mentioned above: elliptical, spiral, lenticular, and irregular galaxies. Ellipticals are sub-classified according to their ellipticity. Spirals are classified according to the size of the bulge component, using a letter from a (dominant central bulge) to m (bulge-less disc). Spirals can also be classified as barred, when a bar is visible in the inner part of the disc. Lenticular galaxies have intermediate morphologies between spirals and ellipticals, and are hence located where the two branches of the fork originate. Irregular galaxies are all those structures that cannot be classified in the tuning fork scheme. Hubble suggested that his diagram should be considered

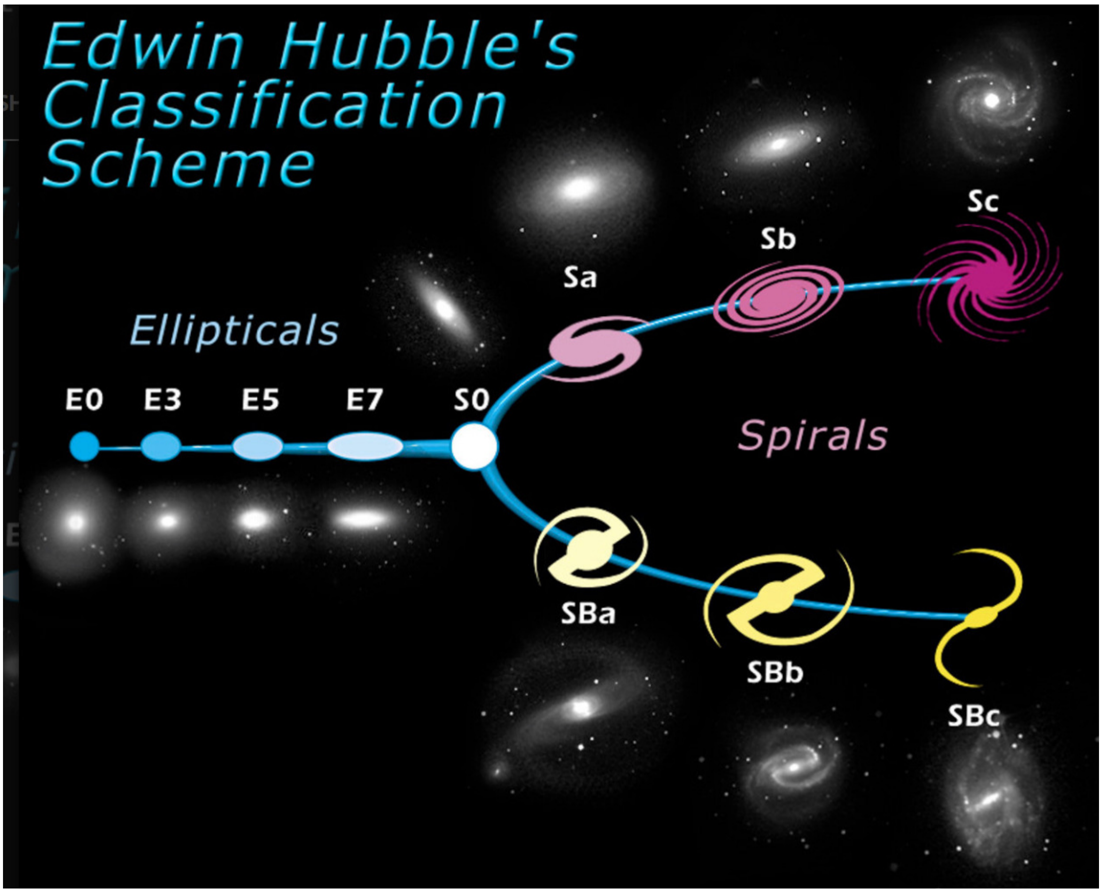

Figure 1.4: A representation of the Hubble tuning fork classification scheme, that divides galaxies in ellipticals, normal spirals, and barred spirals. [From www.spacetelescope.org]

not only as a classification, but as an evolutionary path followed by galaxies. For this reason, he renamed ellipticals as early type galaxies (ETGs), and spirals (both barred and unbarred) as late type spirals (LTGs).

Since its first appearance, the Hubble morphological scheme was subjected to criticism for its inability to include in it all observed galaxies. As a consequence, several revisions were made, and new classification schemes appeared. At the end of 1950 Morgan introduced a classification scheme based on both the appearance (shape and compactness), and the spectral type of stars populating the galaxy. The pillar of the classification proposed by Morgan is the crucial observation that spectral properties of galaxies correlate strongly with their Hubble morphological type (Seares, 1916b,a; Humason, 1932). In 1960s, van den Berg used observations from the Palomar Sky Survey to reveal that the appearance of spiral arms correlates strongly with the luminosity of galaxies (i.e. spiral arms are more likely to be observed in bright, luminous galaxies that in weaker ones). Thus, he proposed a modified Hubble Sequence consisting of a sub-classification of spirals based on their luminosity. Around the same period, the tuning fork diagram was revised by de Vaucouleurs, who added intermediate classes of spirals and included a number between -6 and 10 to indicate the morphological class of a galaxy (de Vaucouleurs, 1962, 1974). In 1948 he also introduces an empirical description of the surface brightness profile of elliptical galaxies and bulges of spirals, that is able to fit the data over a wide range of luminosities:

$$\Sigma(r) = \Sigma_e \; e^{-7.669\left[(r/r_e)^{1/4}-1\right]} \tag{1.11}$$

where r_e is the radius enclosing half of the total brightness and Σ_e is the brightness within r_e. In 1968 the generalised Sérsic profile was introduced (Sersic, 1968): an empirical law able to fit the surface brightness profile of different types of galaxies, from ellipticals to pure spirals. The Sérsic profile can be written as:

$$\Sigma(r) = \Sigma_e \; e^{-b_n\left[(r/r_e)^{1/n}-1\right]} \tag{1.12}$$

where n is the Sérsic index and b_n is a quantity that depends on n. For $n = 4$, the Sérsic profile is the de Vaucouleurs one, that best fits elliptical galaxies and spherical bulges of spirals. For $n = 1$ the Sérsic profile assumes the form of an exponential law, that best describes the disk of spiral galaxies. The Sérsic generalised profile set the stage for finding a single parameter able to distinguish galaxies based on their morphological classes. With this approach, several studies were carried out with the final aim of graduating from visual morphological classifications to quantitative morphology. The compactness of a galaxy, that in the Morgan classification was done by eye, was mathematically described for the first time by Fraser (1972) who introduced the concentration indices C_{21} (C_{32}) defined as the ratio of the radii containing 50 and 25 (75 and 50) percent of the total galaxy luminosity. In 1977 de Vaucouleurs introduced the widely adopted C_{31} index. Over the decades, several studies (Doi et al., 1993; Abraham et al., 1994; Shimasaku et al., 2001; Deng, 2013) conducted with larger galaxy samples reached the same conclusion: the concentration index is the best parameter to classify galaxies and the one that shows the best correlation with visual classification. Trujillo et al. (2001) showed that the Sérsic index n and the concentration parameter are monotonically related, hence making n a widely adopted parameter to distinguish morphologies. With this aim, in the past 20 years codes like GALFIT (Peng et al., 2002), GIM2D (Simard, 1998), and BUDDA (de Souza et al., 2004) have been developed, that are able to fit a model (i.e. Sérsic) to an observed light profile and thus classify galaxies according to their Sérsic index value, or other morphological indicators. Other studies focused on non-parametric morphology with the main aim of finding irregular structures (e.g. mergers) in big samples, giving birth to new morphological parameters like asymmetry, Gini-M20 correlation (Abraham et al., 2003; Lotz et al., 2004), and multiplicity (e.g. Law et al., 2007). Recently, two new pathways to galaxy classification have emerged.

The first is a citizen science project called Galaxy Zoo (Lintott et al., 2008) that visually classifies large samples of galaxies by giving non-astronomers access to database of astronomical observations via the internet. The second involves machine learning and deep learning: morphologies are estimated using Convolutional Neural Network and training the algorithm to mimic human perception (Huertas-Company et al., 2015). This method of classification has proven to be extremely efficient with a very small fraction of misclassifications with respect to visual inspection.

Despite the numerous advancements in morphological classification, all the schemes currently employed can be traced back to Hubble's work. The role of galaxy morphology in galaxy evolution studies was further emphasised when correlations between the observed properties of galaxies and their shape were discovered, as will be described in the next section.

1.2.2 A global bimodality

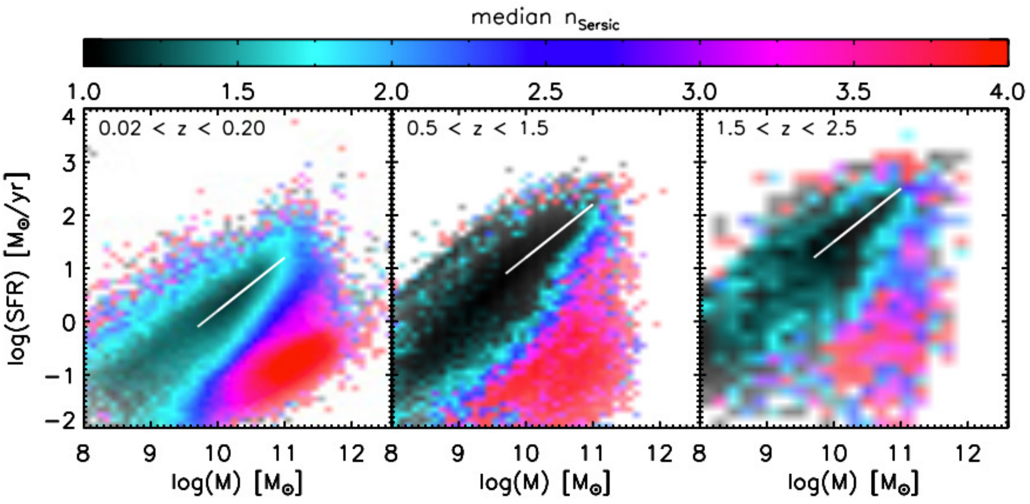

Figure 1.5: Surface brightness profile shape, as described by the Sérsic index, in the $\mathrm{LogM}_\star$ - LogSFR plane, in three different redshift bins. At all epochs, SFGs are well characterised by exponential discs, while quiescent galaxies at all epochs are better described by de Vaucouleurs profiles. [From Wuyts et al. (2011a)]

As seen in the previous section, one way to classify galaxies is on the basis of their morphology. Decades of research has now made clear that ellipticals and spirals do not differ solely because of their appearance but have a plethora of distinguishing properties, as summarised below.

Kennicutt (1992) was the first to observe, from a small sample of 55 galaxies, a correlation between the Hubble type and the strength of nebular emission lines

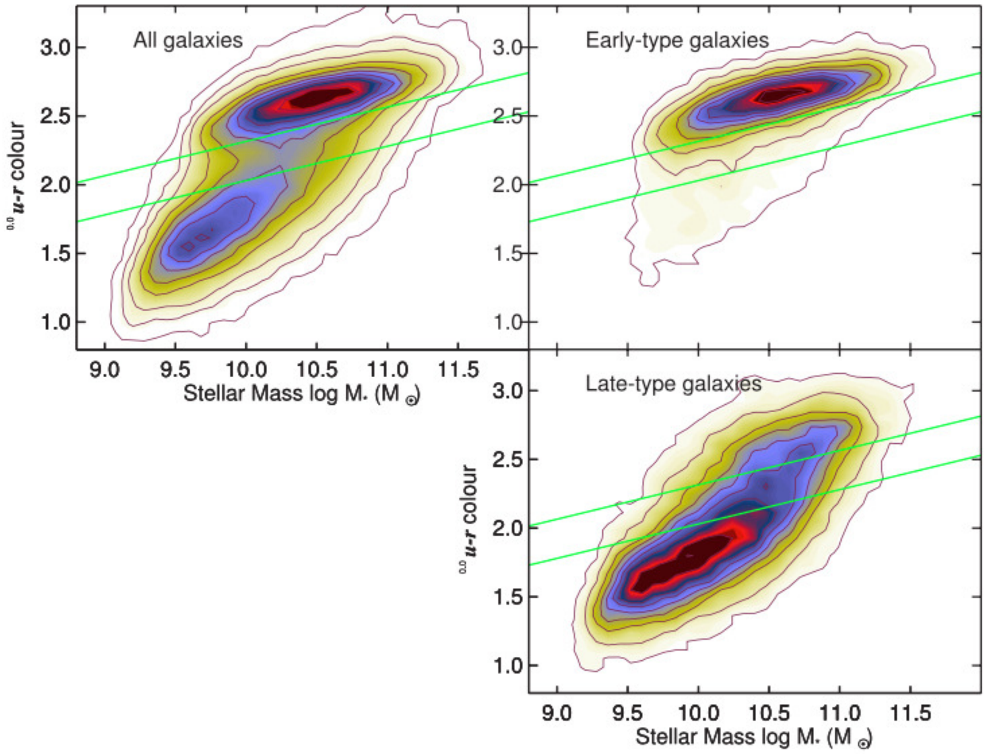

Figure 1.6: The $(u-r)$ colour-mass diagram shown for all galaxies (top left panel) and for the two subsamples of ETGs (top right) and LTGs (bottom right). The contours for the number density of galaxies are shown. [From Schawinski et al. (2014)]

generally associated to star formation activity as well as the shape of the stellar continuum. Recently, studies have shown that discs of spiral galaxies are actively star forming, while ellipticals are are mostly dead (no ongoing star formation) systems (Kauffmann et al., 2003; Schiminovich et al., 2007; Bell, 2008; Scarlata et al., 2007; Poggianti et al., 2008; Franx et al., 2008; Maier et al., 2009; Williams et al., 2010; Wuyts et al., 2011a; Cheung et al., 2012). Galaxies that have ongoing star formation are thus called star forming galaxies (SFGs), while galaxies with no ongoing star formation are referred to as passive galaxies.

The instantaneous star formation activity in a galaxy is computed as the quantity of stellar mass (M$_\star$, given in terms of solar masses, M$_\odot$) produced in a year by a galaxy: the star formation rate, SFR. Fig. 1.5 from Wuyts et al. (2011a) represents the LogM$_\star$ - LogSFR plane, color-coded by the Sérsic index of galaxies, and clearly shows that the two populations of SFGs and passive galaxies are characterised by different values of n: $n \sim 1$ for the former, and $n \sim 4$ for the latter. This result indicates that the spiral/elliptical bimodality of the Hubble diagram translates into a more global bimodality, expressible in terms of the galaxy star formation activity.

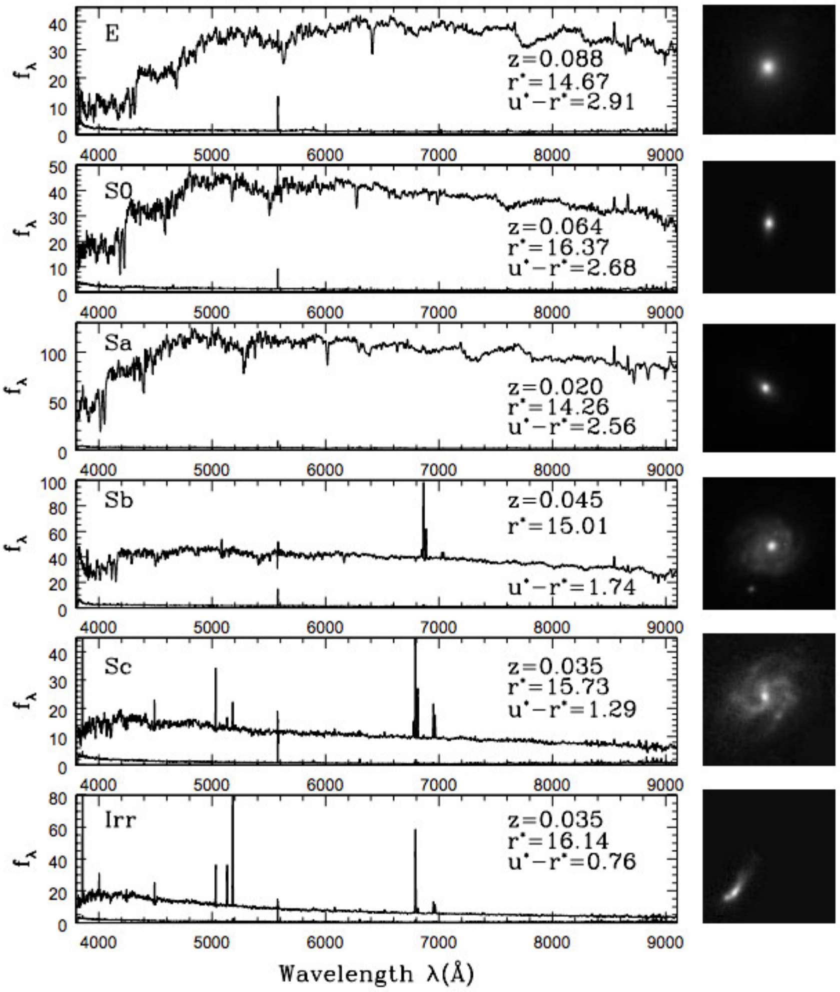

Figure 1.7: Spectra of six different galaxies corresponding to different morphological classes, from ellipticals (top) to late spirals and irregulars (bottom). [From Strateva et al. (2001)]

As a consequence of different star formation activities, the typical stellar populations found in star-forming (SF) and passive galaxies do not have the same characteristics. Morgan & Mayall (1957) were the first to notice, from a small sample of 47 galaxies spectra, that galactic spectra dominated by A and F stars (hotter and more massive stars, associate to recent event of star formation) are in general classified as *Sc* or *Irr*. On the other hand, a spectrum dominated by G stars (stars with intermediate surface temperatures) is typical of galaxies often classified as *Sb*. Finally, *Sa, S0* and *Ell* have spectra dominated by K stars (cold stars, associated to past events of star formation). These results have been recently corroborated by studies carried out using larger samples and deeper data (Proctor & Sansom, 2002; Thomas & Davies, 2006; Kuntschner et al., 2010; Falcón-Barroso et al., 2011; Robaina et al., 2012). Fig. 1.7 shows the spectra of six galaxies belonging to a wide range of morphological classes. The strength of emission lines, as well as the shape of the continuum, change drastically depending on the classification of galaxies: *Irr*, *Sc* and *Sb* have strong emissions and weaker continuum, while spectra of *Sa*, *S0*, and *Ell* have a stronger continuum, weaker or absent emission lines, and relevant absorption features. As the shape of the stellar continuum of a galaxy spectrum directly translates in the integrated colour of the galaxy, the bimodality in morphology and star formation activity is followed by a bimodality in galaxy colours. Spiral, star forming galaxies are generally characterised by blue colours, as they are mainly populated by young, hot stars, while elliptical, passive galaxies are generally red, as they are mainly populated by old, cold stars (Humason, 1936; Holmberg, 1958; de Vaucouleurs, 1961; Roberts & Haynes, 1994; Strateva et al., 2001). This classification holds true if the contribution of dust to the reddening of a galaxy is taken into account, as dust generally absorbs UV light emitted by young stars and re-emits it at longer wavelengths. It is also important to underline that galaxies with intermediate green colours, less numerous than blue and red galaxies, are generally considered as the evolutionary link between the two populations and are called *green valley* galaxies. Fig. 1.6 from Schawinski et al. (2014) demonstrates that the bulk of ETGs are found at red optical colours, while the bulk of LTGs lie at bluer optical colours. Nevertheless, small fractions of blue ellipticals and red spirals also exist as outliers. Spiral and ellipticals do not differ in their composition only because of the typical stellar populations. Observations suggest that cold gas, that fuels star formation, is present in large quantities in discs of spirals, but absent (or present in trace amounts) in ellipticals (Knapp et al., 1985; Schweizer, 1987; Knapp, 1987; Lees et al., 1991). The dust content is also different: generally copious in spirals and missing for a large fraction of ellipticals (Sadler & Gerhard, 1985; Bertola, 1987; Nieto, 1988; Draine, 2003; Draine et al., 2007; Dale et al., 2007; Santini et al., 2010).

The bimodal distribution of LTGs and ETGs, that till now was examined in terms of star formation activity, colour, and gas/dust content bimodality, is also found to hold true when analysing the typical masses of the two families of galaxies. In fact, LTGs and ETGs populate different regions of the stellar mass function, i.e. the number of galaxies of a given mass per unit mass, per unit volume at a given redshift. While spirals are generally found to dominate the low mass tail of the distribution, ellipticals populate the high mass end (e.g. Pannella et al., 2006; Pozzetti et al., 2009; Ilbert et al., 2009). As mass and light in galaxies go hand in hand, it was also found that galaxies with the largest luminosities are preferentially ETGs (Collaboration & Blanton, 2000; Ramos et al., 2011). Fig. 1.8 shows luminosity functions (LF) of galaxies at different redshifts, split in ellipticals (E) and spirals (S). At all redshifts, the high-luminosity end of the global LF is dominated by ellipticals, while spirals dominate at lower luminosities.

Finally, another property that characterises spirals and ellipticals is the typical

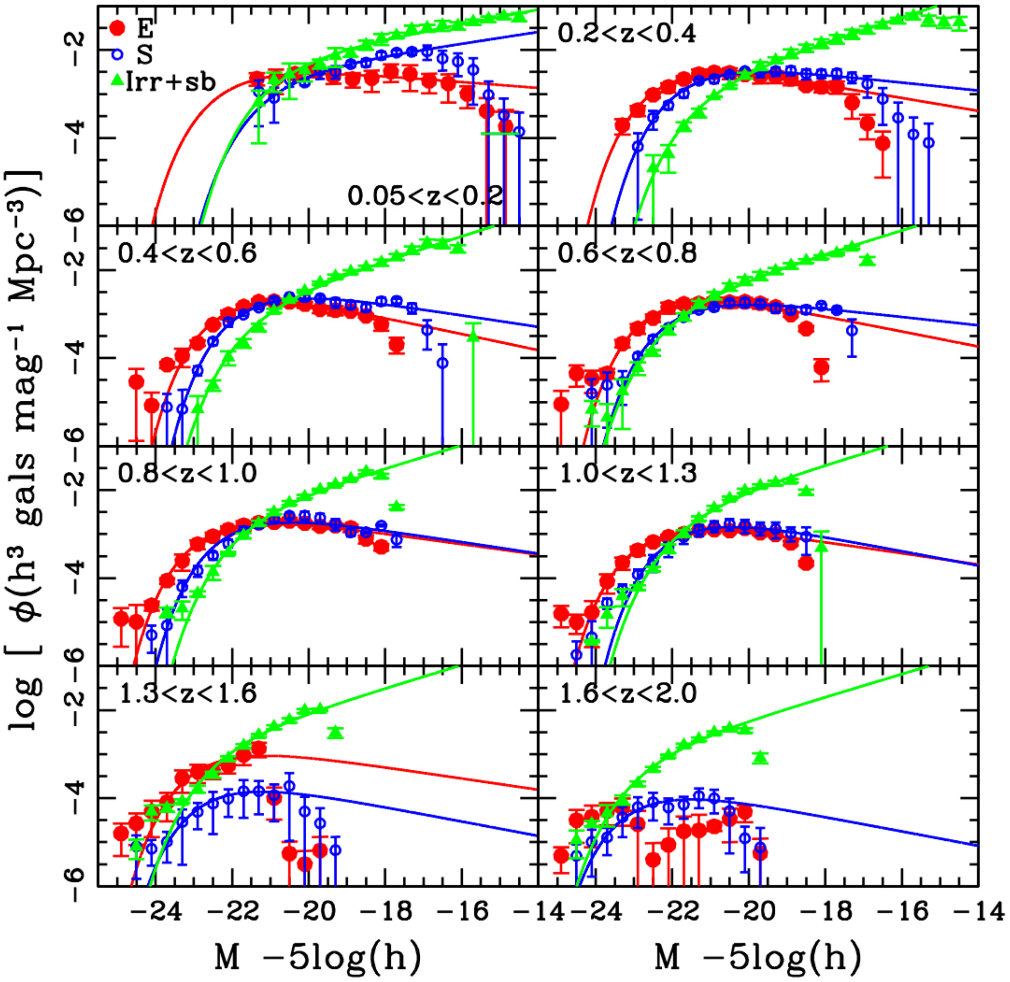

Figure 1.8: Luminosity functions (LFs) in the *i*-band and Schechter fits, divided in E-type galaxies (red), S-type galaxies (blue) and Irregulars (green). The LFs are shown in eight different redshift bins. [From Ramos et al. (2011)]

environment in which they live: low density environments (i.e. field, loose groups) mainly host LTGs, while dense regions of the Universe mainly host ellipticals (i.e. massive groups and clusters of galaxies). This distinction has been known since galaxies became accepted as extragalactic objects (e.g. Hubble & Humason, 1931; Smith, 1935; Zwicky, 1942; Morgan, 1961; Sandage, 1961; Abell, 1965; Oemler, 1974). Dressler (1980) showed that within rich clusters as well, there is a correlation between the local galaxy density and the galaxy type: namely an increase of ellipticals and *S0s* and a decrease of spirals with increasing density (as showed in the left panel of Fig. 1.9). Recent studies, carried out with different telescopes and samples, confirmed the existence of a morphology-density relation that is universal and covers a wide range in density (e.g. Postman & Geller, 1984; Vogt et al., 2004; Balogh et al., 2004; Blanton et al., 2005; Boselli & Gavazzi, 2006; van der

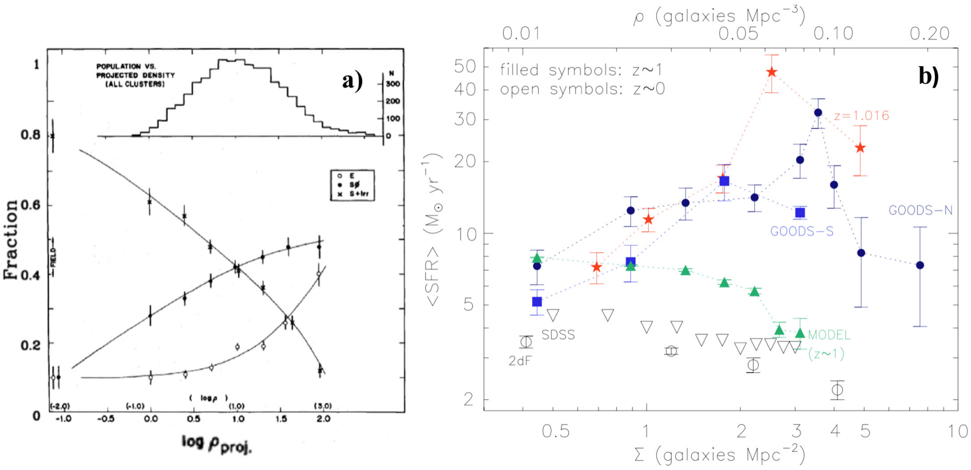

Figure 1.9: Morphology-density relation shown with three different perspective. *Left panel*: the increase in the fraction of ellipticals and S0 galaxies and the decrease in the fraction of spirals and irregulars towards larger projected densities [from Dressler (1980)]. *Right panel*: Environmental dependence of SFR at $z \sim 1$ (filled symbols) and 0 (open symbols) in different fields (GOODS-N, GOODS-S) and in the Millennium simulation (green) [from Elbaz et al. (2007)].

Wel, 2008; Bamford et al., 2009; Skibba et al., 2009; Hirschmann et al., 2014). Since the morphology of galaxies correlates with other integrated properties as seen above, the morphology-density relation has been explored in depth in literature as a function of various properties. The luminosity-density relation reveals that more luminous galaxies are found preferentially in more massive halos (Xia et al., 2006; Zandivarez et al., 2006; Park et al., 2007; Hansen et al., 2009; Yang et al., 2009; Tempel et al., 2011). The colour-density relation shows that bluer galaxies mostly populate field and low density environments (e.g. Lewis et al., 2002; Hogg et al., 2003; Gómez et al., 2003; Hogg et al., 2004; Balogh et al., 2004; Blanton et al., 2005; Baldry et al., 2006; Skibba & Sheth, 2009). According to the SFR-density relation the quiescent fraction of galaxies increases with increasing dark matter halo mass at low redshift (Kauffmann et al., 2003; Bamford et al., 2009; van der Wel et al., 2010; Lin et al., 2015; Gobat et al., 2015), but there is also evidence that hints towards a reversal of the relation at larger redshift (Elbaz et al., 2007). The right panel of Fig. 1.9 shows the SFR as a function of galaxies surface and volume density. The relation is a decreasing function for $z \sim 0$, but reverses at $z \sim 1$. Finally, the kinematic morphology-density relation suggests that the fraction of kinematically selected spirals decreases in high density environments (Cappellari et al., 2011b).

As seen above, a main distinction has emerged between LTGs and ETGs that concerns their ongoing star formation activity. In the past decade, a consistent picture has built up thanks to observation as well as simulations, where the star formation history (SFR as a function of time for a given galaxy) of LTGs and

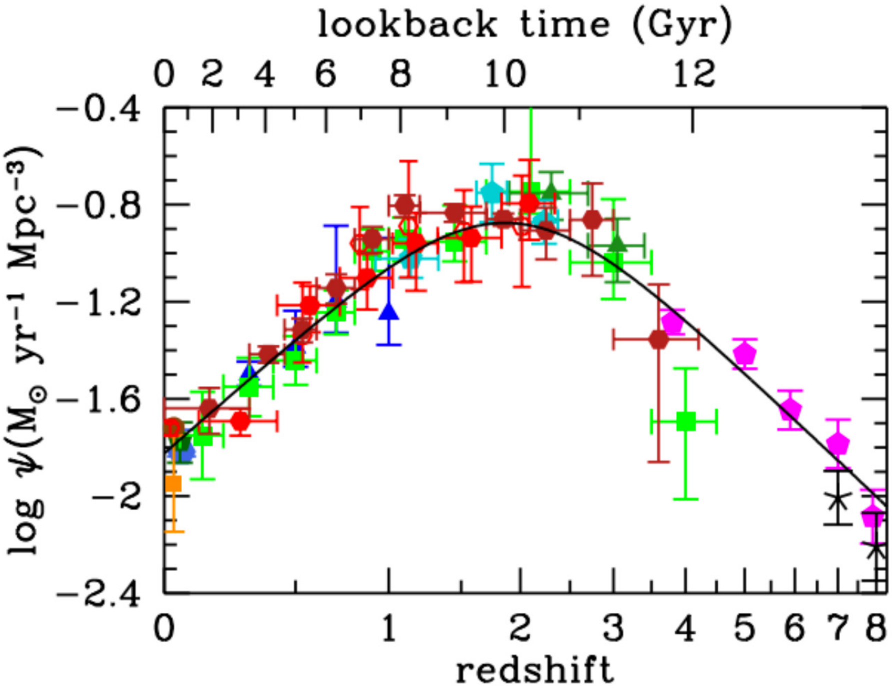

Figure 1.10: The evolution of the SFRD over cosmic time, computed using FUV + IR rest frame measurements as SFR indicators. The black solid curve is the best-fit relation. [From Madau & Dickinson (2014)]

ETGs differs significantly. From a sample of local galaxies, Heavens et al. (2004) discovered that the redshift at which the star formation activity of galaxies peaks is a monotonically increasing function of the final stellar mass of the structure. As more massive galaxies at $z \sim 0$ are predominantly ETGs, this suggests that stellar populations of massive ETGs were formed earlier in the history of the Universe than the ones in spiral galaxies. This apparent anti-hierarchical scenario, in which more massive systems form earlier than less massive ones, is the so-called *downsizing* scenario (Cowie et al., 1996). Downsizing can be reconciled to the hierarchical structure formation model considering that the stellar population in massive ellipticals might have been produced at early times in smaller galaxies (e.g. De Lucia et al., 2006; Nolan et al., 2007; Fontanot, 2010; Eliche-Moral et al., 2010; De Rossi et al., 2013; Kang et al., 2016). In the next section, the star formation activity of the Universe over cosmic time will be analysed, as such evolution holds the key to understand the build up of the Hubble sequence.

1.2.3 Star formation activity evolution

Understanding the evolution of star formation activity through cosmic time is the key to deciphering the observed differences in LTGs and ETGs mentioned above. The derivation of the history of star formation in galaxies requires the ability to estimate mass from light. Astronomers generally estimate the SFR and $M_\star$ of a galaxy from the light that it emits at different wavelengths. Various methods can be used to estimate the SFR depending on the wavelength range used to observe the galaxy. The ultraviolet (UV) traces the light of newly-formed stellar populations, while the infrared (IR) traces the light emitted by stars in the UV, absorbed and re-emitted by surrounding dust. Nebular lines (e.g. Hα, [OII]$_{3727A}$) trace gas excited and ionised due to the intense UV radiation emanating from young stars, located in areas called HII regions. In addition, radio emission also correlates with star formation activity due to the thermal emission from electrons in HII regions accelerated by SN explosions. Each method comes with its own strengths and uncertainties, and can be optimised for use in different redshift ranges (e.g. Wuyts et al., 2011b; Madau & Dickinson, 2014).

In the past two decades the large amount of multi-wavelength imaging and spectroscopic data available has significantly revolutionised our understanding of galaxies, as it is now possible to study the evolution of the star formation rate density (SFRD) through cosmic time from $z = 0$ all the way up to $z \sim 8 - 10$, i.e. almost for the entire history of our Universe (Madau & Dickinson, 2014). Owing to the wide compilation of studies based on various multi-wavelength data that focus on the SFRD at different redshifts, our understanding of the evolution of the star formation activity in galaxies has vastly improved (e.g. Lilly et al., 1996; Madau et al., 1996; Schiminovich et al., 2005; Le Floch & team, 2005). Fig. 1.10 shows the compilation of SFRD measurements taken from Madau & Dickinson (2014). A *rise and fall* behaviour of the SFRD with time is visible: the SFRD steadily increases from $z \sim 8$ to $z \sim 3$, it peaks between $z = 2$ and 1.5 and then decreases almost exponentially by an order of magnitude to the $z = 0$ value. The behaviour of the SFRD shows that the Universe was a more active place ~ 10 Gyrs ago, with galaxies forming stars at a rate approximately 9 times larger than the typical $z = 0$ value. It is also possible to estimate that $\sim 50\%$ of the total stellar mass density was generated in the peak period, while $\sim 25\%$ formed at $z > 2$, and the remaining $\sim 25\%$ over the last half of the Universe's lifetime. In the past decades, new insight into the process of star formation came from the discovery of a tight correlation between the SFR and the stellar mass of a galaxy; the next section explores such a correlation and its impact on the SFRD of the Universe.

1.2.4 The Main Sequence of SFGs

Studies indicate that most star forming galaxies, at least at $z < 4$, form stars in a relatively *ordered* fashion as they follow a tight correlation between the SFR and the stellar mass, or the so-called *Main Sequence of star forming galaxies* (MS) (e.g. Brinchmann et al., 2004; Noeske et al., 2007; Daddi et al., 2007; Elbaz et al., 2007; Salim et al., 2007; Whitaker et al., 2012; Speagle et al., 2014; Pannella et al., 2015). Estimates of the slope of the relation vary widely in literature, and assume a value between 0.2 and 1.2 (Speagle et al., 2014), mainly because of four reasons: 1) the selection criteria applied to identify SFGs, that can be based on a single colour cut, or on two-colours selections (BzK or UVJ), or on cuts on a value of specific SFR (sSFR); 2) the SFR indicator used (e.g. $H\alpha$, IR luminosity, D4000 break); 3) the fitting method used to identify the location of the MS at a fixed stellar mass (mean, median, mode); and 4) the range of stellar mass of the sample, as recent results suggest a flattening of the MS relation at the high mass end (Whitaker et al., 2014; Schreiber et al., 2015; Erfanianfar et al., 2016). In some extreme cases, when selecting galaxies with a cut in SFR, the MS in not recovered (Erb et al., 2006; Reddy et al., 2006; Lee et al., 2013). Given the need for a detailed understanding of the evolution of the MS for galaxy growth, Renzini & Peng (2015) suggested an “objective” definition of the MS as the ridge line of the star-forming peak (i.e. the mode of the distribution) in the 3D SFR-Mass-Number diagram, independent of the pre-selection of SF galaxies, as shown in Fig. 1.11. Nevertheless, despite the disagreement on the value of the MS slope in literature, there is a general consensus that the slope does not show evolution with redshift. On the other hand, the normalisation changes drastically with redshift, in accordance to the evolution of the SFRD, indicating that galaxies were forming more stars in the past than they are today. The characteristic specific star formation rate of the MS population decreases by a factor ~ 20 from $z = 2$ to $z = 0$ (Schreiber et al., 2015). According to hydrodynamical simulations, semi-analytical models and analytical models able to reproduce the MS of SFGs, the decrease in the normalisation towards lower redshifts is a consequence of the declining gas accretion onto galaxies (Bouché et al., 2010; Dutton et al., 2010; Davé et al., 2011; Dekel et al., 2013; Lilly et al., 2013; Torrey et al., 2014; Mitchell et al., 2014; Sparre et al., 2015; Forbes et al., 2014). Such a decline reflects the cosmological evolution of the accretion rate of gas into dark matter halos (Neistein et al., 2006; Birnboim et al., 2007; Genel et al., 2010; Tacchella et al., 2013).

An interesting feature of the MS is its low scatter, that remains more or less constant over a wide range of stellar masses and over cosmic time, at least up to $z = 2.5$ (e.g. Rodighiero et al., 2011; Whitaker et al., 2012; Schreiber et al., 2015). Evidence suggests that the scatter seems to increase only at the high mass end, suggesting the existence of a wider variety of channels for the growth of massive

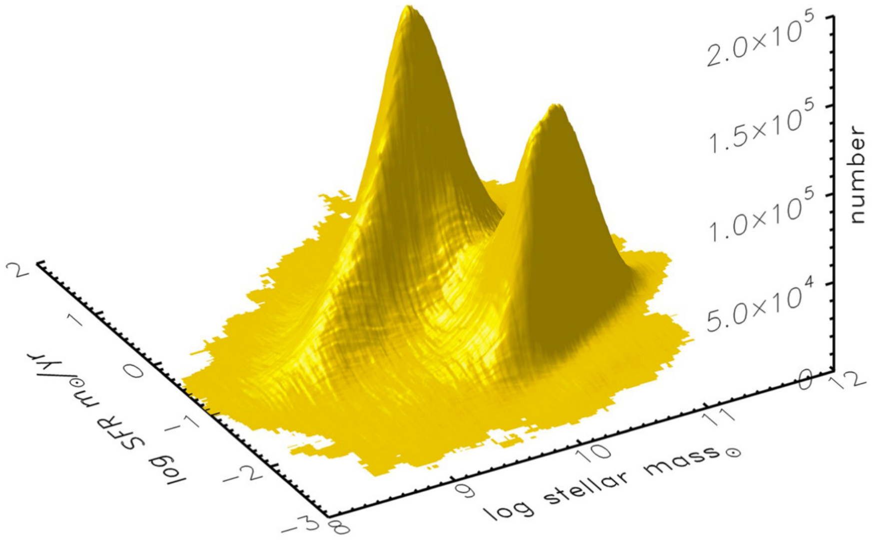

Figure 1.11: Three-dimensional SFR-M$_\star$ relation for local galaxies in the SDSS database and $0.02 < z < 0.085$. On the z axis the number of galaxies in each SFR-M$_\star$ bin is shown. The sharp ridge line of the SF peak is the objective MS definition given in Renzini & Peng (2015). [From Renzini & Peng (2015)]

galaxies (Guo et al., 2013; Ilbert et al., 2015). While the slope of the MS is related to the variation of the SFR at different stellar masses, the dispersion is related to the level of stochasticity in the star formation history (SFH) of galaxies, i.e. on their gas accretion history as well as the SF efficiency (Dutton et al., 2010; Leitner, 2012; Behroozi et al., 2013b; Sparre et al., 2015). Salmi et al. (2012) concluded that errors in the estimates of SFR and stellar mass are not responsible for the scatter in the MS, and thus, the scatter is *real* and reflects diversity in the SFR of galaxies over time. The small scatter of the MS suggests that in the largest fraction of SFGs, star formation activity is driven by secular processes and stochastic events such as merger-driven starbursts (i.e. galaxies that, at each stellar mass, have the largest SFRs) play a relatively minor role. Estimates of the time spent by a galaxy in phases of enhanced star formation are found to be inconsistent with the very short time scale of major mergers, thus implying that the scatter of the MS is not caused by mergers (Cox et al., 2008; Lotz et al., 2010).

Observations of the gradients of gas fraction and depletion times are seen across the MS and thus provide clues on the nature of its scatter: galaxies with the largest sSFRs have larger gas fraction and shortest depletion times (Magdis et al., 2012; Sargent et al., 2014; Wang et al., 2014; Genzel et al., 2015; Silverman et al., 2015; Lee & Team, 2015; Scoville et al., 2015). Dutton et al. (2010) concluded that the scatter could be related to variations in the DMH concentration that can in turn result in variations in the mass accretion history of galaxies belonging to the same halo. Recent studies focused on understanding the typical timescale of SFR variation embedded in the MS scatter (Abramson et al., 2015; Muñoz & Peeples, 2015), a topic highly connected to how SFGs accumulate mass during their lifetime. Tacchella et al. (2015b), using the VELA cosmological simulation (Muñoz & Peeples, 2015), showed that the mechanism that confines galaxies in a small 0.3 dex range above and below the MS is related to gas regulation, in particular to the balance between the inflow rate of cold gas, the SFR activity and the outflow rate. According to Tacchella et al. (2015b), a MS galaxy moves towards upper envelop of the MS when minor mergers or counter rotating streams trigger gas infall in the central region (Noguchi, 1998; Gammie, 2001; Dekel & Birnboim, 2006; Bournaud et al., 2007; Burkert et al., 2010; Cacciato et al., 2012; Dekel & Burkert, 2013). This is the so called compaction phase, that results in a blue-nugget galaxy. Central gas depletion (due to high SFR and stellar feedback) with short characteristic time scales moves the galaxy from the upper to the lower envelop of the MS, where galaxies typically have long depletion time scales and low gas fractions. Using cosmological zoom-in simulations, Zolotov et al. (2015) showed that gas compaction and central depletion are frequent events in high-z galaxies, and are actually the most important events in the lifecycle of galaxies, thus enabling the compaction-depletion scenario to become a straightforward explanation for the MS scatter. Observationally, Wuyts et al. (2011a) analysed the dependence of the position of the galaxies on galaxy structure (size and Sérsic index n), with respect to the MS ridge in the redshift range 0-2. They found that the Sérsic index tends to be roughly constant, $n \sim 1$, within 3σ from the MS, i.e. there is no significant gradient of n across the MS. Furthermore they showed that, galaxies located above 3σ from the MS (starburst galaxies, SB) seem to be more concentrated and spherical than MS counterparts. Guo et al. (2015) used a sample of local galaxies to conclude that, for massive galaxies, bulges and bars are responsible of the increase in the MS scatter.

More recently, a new approach to the study of the nature of the MS relation and its scatter came from spatially resolved observations of galaxies, enabling the community to study galaxies as objects comprising of individual components. Several investigations have unraveled a relation between the star formation surface density and the stellar masses at the ~ 1 kpc sale, the so-called *spatially resolved* MS of SFGs (Wuyts et al., 2013; Magdis et al., 2016; Cano-Díaz et al., 2016; Maragkoudakis et al., 2017). Ellison et al. (2017) found that galaxies above the MS are characterised by a great enhancement of SFR surface density in the central regions, while galaxies below the MS show a depression in their SFR profiles in the inner part, in agreement with the earlier predictions of Tacchella et al. (2015b). Belfiore et al. (2017) found that galaxies below the MS have heavily suppressed SFR in the inner part and less suppressed SFR in the outer disc. Such spatially resolved observations of galaxies, made possible by a new observational technique called integrated field spectroscopy (IFS), has greatly improved our understanding of the star formation activity of galaxies and will continue to do so in the next years. Examples of IFS survey of galaxies are Atlas3D (Cappellari et al., 2011a), CALIFA(Sánchez et al., 2012), MaNGA (Law & Team, 2014) and SAMI (Croom et al., 2012).

Despite the great advancement in understanding the different properties of LTGs and ETGs, as well as the evolution of star formation over cosmic time, the primary mechanism (internal or external) responsible for quenching star formation in galaxies and transforming them into quiescent systems still eludes us.

1.2.5 From star forming to passive: the quenching mechanism

In galaxy evolution, the term quenching defines the process (or ensemble of processes) able to inhibit star formation activity, and thus leads to the formation of red and dead galaxies. Quenching of star formation is a fundamental process as significant discrepancies are in place between the observed luminosity function (LF) of galaxies and the LF predicted by CDM-based numerical simulations of galaxies. In fact, CDM-based numerical simulations of galaxies, where it is assumed that the stellar mass of galaxies follows the halo mass, predict a larger number of galaxies both at the low and at the high mass (or luminosity) end, while good agreement is found between simulations and observations for the typical mass (or luminosity) of galaxies. In other words, the efficiency with which baryons are converted into stars in halos of different masses remains a key problem of CDM-based models of structure formation. Several works (e.g. Conroy & Wechsler, 2009; Guo et al., 2009; Behroozi et al., 2013a; Kravtsov et al., 2014) have shown that this efficiency peaks for halos with $M_{halo} \approx 10^{12} M_{\odot}$, but decreases for both lower and higher mass halos due to feedback processes that must be responsible of impacting the cold gas reservoir of galaxies. Fig. 1.12 shows a very common depiction of this problem. The difference between the observed LF (in blue) and the simulated LF (in red) of galaxies has its minimum around $\sim 3 \cdot 10^{10} L_{\odot}$. At both increasing and decreasing luminosities, this difference increases, implying the omission of some baryonic processes in CDM simulations responsible for lower star star formation activity and hence lower number of galaxies observed at a given luminosity. As the key ingredient of star formation activity is the availability of cold gas from which new stars form, most of the proposed quenching mechanisms in literature focus on how to halt cold gas accretion into galaxies, or on how to remove the accreted cold gas. Several processes have been proposed, and have been split in two categories: 1) internal, when the process is

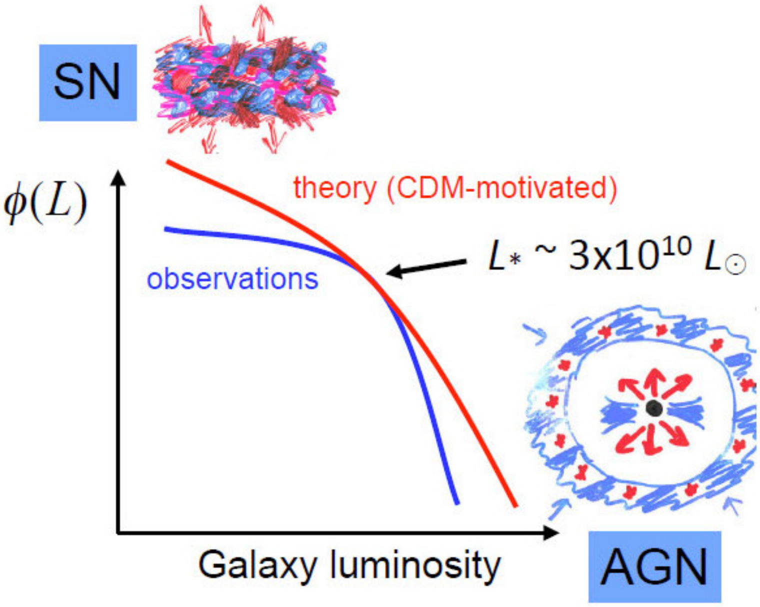

Figure 1.12: The discrepancies between the luminosity function of observed (red) and simulated (blue) galaxies enhances the need for a mechanism able to stop star formation, both at low and high luminosities. [From ned.ipac.caltech.edu]

dependent on the properties of the galaxy itself and not on the environment in which the galaxy is hosted, and 2) external, when the process is related to the characteristics of the environment the galaxy sits in (i.e. dark matter halo mass, satellite vs. central, local density).

In low mass dark matter haloes (i.e. for lower mass galaxies) the role of quenching is played by SN feedback (internal mechanism), that releases enormous amounts of energy and momentum into the surroundings. While ionising radiation creates giant HII regions, SN-driven winds also act to expand the cavities and generate super-bubbles, where no star formation can occur (Dekel & Silk, 1986; Efstathiou, 2000; Murray et al., 2005). Internal processes in more massive galaxies are mainly associated to the co-evolution of the galaxy with its central super massive black hole (SMBH). In fact, observational evidence was found supporting the idea that SMBH masses correlate tightly with the properties of the host galaxy, in particular with the spheroidal component (e.g. Kormendy & Richstone, 1995; Magorrian et al., 1998; Ferrarese & Merritt, 2000; Gebhardt et al., 2000; McLure & Dunlop, 2002; Tremaine et al., 2002; Marconi & Hunt, 2003; Häring & Rix, 2004; Gültekin et al., 2009; McConnell & Ma, 2013; Kormendy & Ho, 2013; DeGraf et al., 2015; Graham et al., 2015; Graham, 2016). The discovery of the aforementioned correlations opened a new channel of inquiry focusing on the ability of SMBHs to impact cold gas reservoirs of star forming galaxies. The phase during which this occurs is known as Active Galactic Nuclei (AGN) feedback, that can be summarised as the interaction between the gas present in a galaxy and the radiation emitted from the SMBH during an accretion phase. In particular, two different forms of feedback can be identified. When the winds from the AGN are able to push the gas in its surroundings and expel it from the galaxy (at least from the disc), the feedback is referred to as radiative, or quasar-mode (e.g. Silk & Rees, 1998; Fabian, 1999, 2002; King & Pounds, 2003; Hopkins et al., 2006b,a; Dunn et al., 2010; Feruglio et al., 2010; Fabian, 2012; Cicone et al., 2014). The kinetic, or radio-mode feedback occurs when a SMBH is able to produce radio jets and keeps the gas hot (e.g. Pedlar et al., 1990; Tabor & Binney, 1993; Peterson & Fabian, 2006; Croton et al., 2006; Bower et al., 2006; De Lucia et al., 2006; McNamara & Nulsen, 2007; Bower et al., 2008; Cattaneo et al., 2009; Fabian, 2012; Vogelsberger et al., 2013). Another internal scenario is the so-called *morphological quenching*. In this scenario, proposed by Martig et al. (2009), the presence of a massive bulge in the inner part of a spiral galaxy stabilises the disc, which could still host cold gas, against fragmentation and collapse. This scenario implies that bulges are a necessary condition to have lack of star formation in galaxies, and that large amounts of cold gas should be present in dead ellipticals. The existence of passive bulge-less galaxies (nevertheless a very small fraction of the total passive population) then has to be explained by other quenching mechanisms.

As seen above, a galaxy's cold gas supply can also be affected by external processes that the galaxy experiences when it enters a more massive DMH (or more dense environment). Tidal interactions develop when a galaxy experiences the gravitational field of a neighbour. The strength of the tidal force depends on the masses of the two galaxies and their separation, and can thus result in significant outflows of cold gas from the disk towards central regions causing enhanced star formation and consequently, gas exhaustion. The tidal interaction present due to the DMH's gravitational field also results in gas inflows from outer to inner regions, bar-developments, and gas exhaustion following a starburst phase (Byrd & Valtonen, 1990; Merritt, 1984; Villalobos et al., 2012). In general, the effects of tidal forces due to a galaxy's high speed interactions and to the DMH potential well are called galactic harassment (Moore et al., 1998). Ram pressure stripping, instead, is defined as the pressure exerted on a galaxy moving through the hot and dense gas that permeates a massive DMH, with $T \sim 10^7 - 10^8$K and $\rho \sim 10^{-4} - 10^{-3}$atoms/cm^{-3} (Gunn & Gott, 1972). Ram pressure has been observed to drag neutral gas, as well as molecular gas and dust, but does not affect the old stellar component (Roediger & Hensler, 2005; Gavazzi et al., 2013; Boselli et al., 2014; Cortese et al., 2012; Fossati et al., 2013; Poggianti et al., 2016). Nulsen (1982) proposed viscous stripping as a possible way to extract cold gas from the edges of a disk of a galaxy, but because of the similarities with ram pressure stripping signatures, it is difficult to observationally isolate this process. Cowie & Songaila (1977) noticed that thermal evaporation could also occur at the interface between hot ICM and cold ISM, resulting in heating and evaporation of the latter. Finally, as hot gas in a galaxy can potentially cool and become fuel for star formation, the removal of hot gas can also affect the cold gas replenishment as this occurs in dense environments (Larson et al., 1980; Bahé et al., 2013). It has also been shown, using cosmological simulations, that the temperature of the gas accreted by galaxies through filaments from the cosmic web is a function of the halo mass. In particular, DMH with $\mathrm{M}_h > 10^{12} M_\odot$ are found to accrete hot gas, in contrast to lower mass haloes that accrete cold gas (Birnboim & Dekel, 2003; Kereš et al., 2005; Dekel & Birnboim, 2006; Kereš, 2009; Birnboim & Dekel, 2011). When accretion of cold gas halts, a galaxy is *strangulated* and becomes progressively passive by using up its cold gas reservoirs and declining star formation rate, or more abruptly as a consequence of a major merger which would also involve a more significant increase in stellar mass (Cen, 2014; Peng et al., 2015; Smethurst et al., 2015). It has also been proposed that quenching could be a combination of all these processes. For example, using their cosmological zoom-in simulations, Zolotov et al. (2015) show that quenching of high redshift SFGs is preceded by a compaction phase that creates the so-called blue nuggets: SFGs morphologically similar to quiescent ones. This compaction phase is caused by strong inflows to the centre due to minor mergers and/or counter-rotating gas and violent disk instabilities. The availability of dense cold gas in the centre results in high SF and consequently stellar/SN and/or AGN feedback causing quenching. Tacchella et al. (2015b) propose that episodes of compaction, quenching and replenishment are responsible for a galaxy to be located in a ±0.3 dex region around the MS. The final quenching happens when the replenishment time is longer than the depletion time (i.e. in massive haloes, or at low redshifts), leading to a passive galaxy.

Despite the plethora of studies investigating the nature of quenching, this topic is not yet fully understood and hence, an important aspect of galaxy evolution still eludes us.

1.3 Open questions

The overview of galaxy properties and galaxy evolution given above clearly shows how, despite many advances in the understanding of a galaxy life cycle, topics like the evolution of the star formation activity through cosmic time, as well as the connection between processes able to quench star formation in galaxies and processes responsible for the morphological transformation of galaxies, are still raising many open questions. Since the discovery of the MS, a large fraction of galaxy evolution studies focused on understanding how galaxy properties evolve along and across the relation. This was done mainly for three reasons: 1) to understand the drivers of the scatter of the relation; 2) to shed light on the quenching mechanism by exploring the different properties of galaxies on the MS and in the passive region; 3) to understand the mechanism able to boost star formation well above the MS, in the region of starburst galaxies. This thesis aims at answering the following questions: *what is the role of the individual galactic components, bulges and discs, in shaping the scatter of the MS? What is the spatial distribution of the star formation activity of starburst, normal star forming and passive galaxies?* In recent years, several morphological decomposition of galaxies became available for large samples of galaxies, both in the local Universe and at higher redshift (Lintott et al. 2008, Gadotti et al. 2009, Simard et al. 2012, van Der Wel et al. 2012, Huertas-Company et al. 2015). In this thesis, structural decompositions of galaxies will be studied to understand their variations both along and across the relation and over a wide redshift range, with the final aim of drawing a coherent picture of the drivers of the MS scatter, the mass growth of galaxies along the MS, and of the processes responsible for starburst phases and quenching. Chapter 2 of the thesis will focus on local Universe, while in Chapter 4 a sample of $z \sim 1$ galaxies will be analysed. Nevertheless, as the MS is used as a tool to understand the evolution of the star formation activity in galaxies, potential biases in the MS estimate (slope and dispersion) need to be accounted for, to avoid obtaining results affected by selection biases. Selection effects might play an important role especially when samples of green valley galaxies are created and used to study the quenching timescales (e.g. Schawinski et al., 2014; Smethurst et al., 2015; Coenda et al., 2017; Belfiore et al., 2017). Chapter 3 of this thesis will explore the following question: *Does the inclination of a galactic disk bias the measurements of the SFR for local galaxies? What is the impact on the Main Sequence of SFGs?.* SFR estimates depend on corrections for the dust content of galaxies, usually estimated from fitting the spectral energy distribution (SED) of galaxies, or from emission line ratios known to be good tracers of dust. When the disk of a spiral galaxy is close to edge-on, light attenuation from dust is at its maximum, as light as to travel larger distances within the disc. Chapter 3 of this thesis explores the problem of galaxy inclination when determining its SFR, with consequences on both the MS slope estimate and on selection effects on the sample of green valley galaxies.

2 The morphology - star formation activity link at low redshift

The content of this chapter has been published in Morselli et al. (2017), with only some modifications being made to the manuscript when adopting it for this thesis. The original manuscript (Astronomy & Astrophysics, Volume 597, id.A97) was written together with coauthors Paola Popesso[1], Ghazaleh Erfanianfar[1,2], and Alice Concas[1].

[1]Excellence Cluster Universe, Boltzmannstr. 2, Garching bei München, 85748, Germany
[2]Max-Planck-Institut für extraterrestrische Physik, Gießenbachstrasse 1, Garching bei München, 85748, Germany

2.1 Introduction

The aim of this chapter is to study the relation between galaxies structural parameters and location with respect to the MS in the local Universe. The choice of performing this study starting on a local galaxy sample is dictated by the fact that the Sloan Digital Sky Survey (SDSS; Strauss et al., 2002) provides the required statistics to dissect the MS brick by brick to study the nature of its scatter as a function of the galaxy morphology with high accuracy. In addition, the availability of accurate morphological classification and bulge/disk decomposition of SDSS galaxies allows us to study the role and interconnection of the individual galaxy components. Throughout this chapter, the following cosmology is assumed: $H_0 = 70.0\ km\ s^{-1} Mpc^{-1}$, Ω_m=0.3 and Ω_Λ=0.7.

2.2 Dataset

In this chapter we make use of the catalogues derived from the SDSS-DR7 database (Abazajian et al., 2009) and in particular the following quantities: star formation rates, stellar masses, stellar velocity dispersion, and properties derived from bulge/disk decomposition of galaxies. We now briefly summarise how these were derived and provide references to the original papers for details.

2.2.1 SFRs, stellar masses, and velocity dispersion

SFRs and $M_\star$ are taken from the MPA/JHU DR7 catalogues (Kauffmann et al., 2003; Brinchmann et al., 2004; Salim et al., 2007). Stellar masses have been estimated from a fit to the photometry, using a large grid of models from Bruzual & Charlot (2003) and spanning a wide range of star formation histories. We use the total, aperture corrected stellar mass computed from the total *ModelMag* photometry that is less sensitive to emission line contamination. SFRs come from emission line modelling using the grid of $\sim$ 2x10^5 models of Charlot & Longhetti (2001). Dust corrections are mainly based on the H_α/H_β ratio. To calculate the likelihood of each model, Brinchmann et al. (2004) use a Bayesian approach. Since the likelihood distribution of a given parameter gets broader for decreasing signal-to-noise ratios (S/N), the SFR comes from the H_α line just for galaxies with S/N > 2. For AGNs and composite galaxies, as classified in the BPT diagram, and for galaxies with no H_α emission, the SFR comes from the D4000 break, that is known to correlate with sSFR (sSFR = SFR/$M_\star$). An aperture correction to the SFR based on the fit of the light outside the aperture to stochastic models is applied to account for the small 3" diameter of the SDSS fiber (Salim et al. 2007). The aperture velocity dispersion, σ_{ap}, and mean S/N per pixel are taken from the MPA/JHU *gal-info* catalogue, while values of the H_α and H_β fluxes and their S/N ratios are form the MPA/JHU *gal-line* catalogue.

2.2.2 The bulge/disk decomposition catalogue

Galaxy structural parameters are taken from the bulge/disk decomposition of the Simard et al. (2011) catalogue (S11 hereafter). In S11, the GIM2D code (Simard et al., 2002) has been applied to the g and r filter images of 1,123,718 SDSS DR7 galaxies to obtain a two-dimensional bulge-disk decomposition convolved with the point-spread function. The simultaneous fit of the g and r images makes the decomposition robust against spurious effects. S11 provide structural parameters for three different fitting models: 1) a pure Sérsic, 2) an exponential disk plus De Vaucouleurs bulge, and 3) an exponential disk plus free Sérsic bulge model. In this work, we use the catalogue obtained from the exponential disk plus De Vaucouleurs bulge model as the F statistics reveal that SDSS images are not good enough to efficiently compute the Sérsic index of the bulge and its structural parameters (see S11 for details). The S11 catalogue obtained from an exponential disk plus De Vaucouleurs bulge includes an estimate of the bulge-total ratio (B/T) done both on the r-band (B/T[r]) and on the g-band (B/T[g]) images. The comparison between B/T[r] and B/T[g] shows a very good agreement, as shown in Fig. 2.1: the slope of the correlation is very close to 1 (0.96±0.05), the intercept is 0.05±0.03 and the Spearman correlation ranking is 0.98.

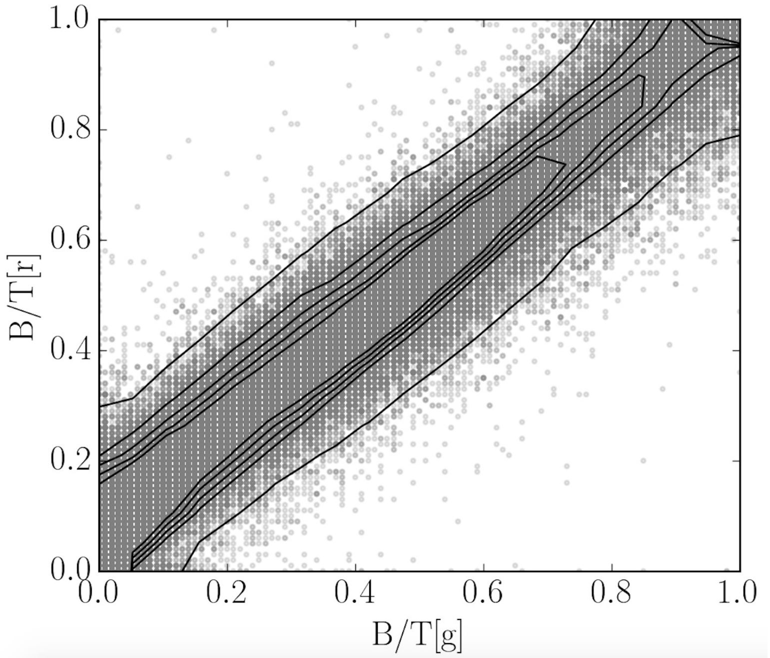

Figure 2.1: Comparison between the B/T computed from the g-band image and the B/T computed from the r-band image. Both estimates come from the S11 catalogue, obtained in the case of an exponential disk plus De Vaucouleurs bulge model.

In this work, we use the B/T computed from the r-band image and the magnitudes of the bulge and disk components, that are given as rest-frame, extinction, and K corrected. Extinction values are taken from the SDSS pipeline, while K correction was computed using version 4.2 of *k-correct* (Blanton & Roweis, 2007). The total, K and extinction corrected r and g-band magnitudes of the galaxies in S11 agree very well with the SDSS Petrosian magnitudes (extinction and K corrected). We use the criterion $P_{PS} \leq 0.32$ (as suggested by S11) to select robust subsamples of genuine bulge plus disk systems, where P_{PS} is the probability that a two-component model is not statistically needed to fit the galaxy image. In this work, we will also use other outputs of the S11 morphological decomposition in the case of an exponential disk plus De Vaucouleurs bulge model, like the effective radius of the bulge, $r_{e,bulge}$, the disk scale height, $r_{h,disk}$, and the disk inclination.

2.2.3 Galaxy host halo mass

We use the group catalogue of Yang et al. (2007, Y07 hereafter) and Yang et al. (2012), an optically selected galaxy group and cluster sample for a complete spectroscopic subsample ($0.01 < z < 0.2$) of DR7 SDSS galaxies. The halo-based group finder of Y07 works as an iterative algorithm and, unlike the traditional friend-of-friend (FoF) method, it is able to identify groups, pairs and isolated halos. Summarising, the algorithm first finds the potential group centres using FoF and considers all the remaining galaxies as isolated. Then, it computes the characteristic luminosity ($L_{19.5}$) of each group and its halo mass assuming a functional form for $M_{halo}/L_{19.5}$, constant in the first iteration, $L_{19.5}$-dependent for the remaining iterations. This method of computing halo mass, with respect to gravitational lensing or X-ray emission based techniques, is able to span the entire richness range, thus a larger range in halo masses (Yang et al., 2005). Finally, using halo properties, the algorithm updates the group members and iterates the procedure. The reader can refer to Y07 for the details regarding the method. In particular, we use the Sample A group catalogue built without considering fiber-collision corrections. This catalogue provides two estimates of the group halo mass (M_{halo}): one based on $\mathrm{L}_{19.5}$, the other based on the characteristic stellar mass. In our analysis we use the estimate of M_{halo} from the characteristic stellar mass $M_\star$, since the M_{halo}-$M_\star$ relation is slightly tighter than the M_{halo}-$L_{19.5}$ relation (Y07). The catalogue provides halo masses only for groups whose characteristic $M_\star$ is above $10^{10.2} M_\odot$. Thus, the algorithm does not assign halo masses below $10^{11.5}$ $M_\odot$ where one must extrapolate the calibration. However, estimating the characteristic $M_\star$ of very low mass halos with just one or two galaxies is very uncertain. Thus, we assign an upper limit halo mass of $10^{11.5}$ $M_\odot$ to halos with masses below this threshold.

2.2.4 The galaxy sample

We construct the master catalogue from the MPA-JHU SFR and $\mathrm{M}_\star$ catalogue, after removing duplicates and objects with no SFR or $\mathrm{M}_\star$ estimates, and cross-correlate it with the S11 catalogue. Less than 2% of galaxies do not have a SFR or a stellar mass estimate because of low quality photometric or spectroscopic data. In the cross-correlation between the master and the S11 catalogues, only 8% of galaxies are lost owing to minor differences in the selection criteria applied in S11. The cross correlation with the catalogue of Y07 leads to the exclusion of 5% of the sample, partially overlapping with the 8% of S11. This is due to the fact that Y07 limit the analysis to SDSS regions with a minimum of 70% spectroscopic completeness, thus, losing a low percentage of galaxies in regions of lower completeness. To limit our analysis to a local volume galaxy sample with relatively high spectroscopic completeness, we select galaxies that satisfy the following criteria: $0.02 < z < 0.1$, $\mathrm{LogM}_\star \geq 9.0\ \mathrm{M}_\odot$, no AGN as identified in the MPA-JHU catalogue, and a good estimate of z and SFR. Galaxies that are classified as AGN ($\sim 3\%$) in the BPT diagram in the MPA-JHU catalogue are removed from the sample as the AGN component could provide a significant contribution to the host galaxy colours. Thus, the inclusion of the AGN population, though not very significant in numbers, could bias our analysis of the galaxy bulge and disk colours.

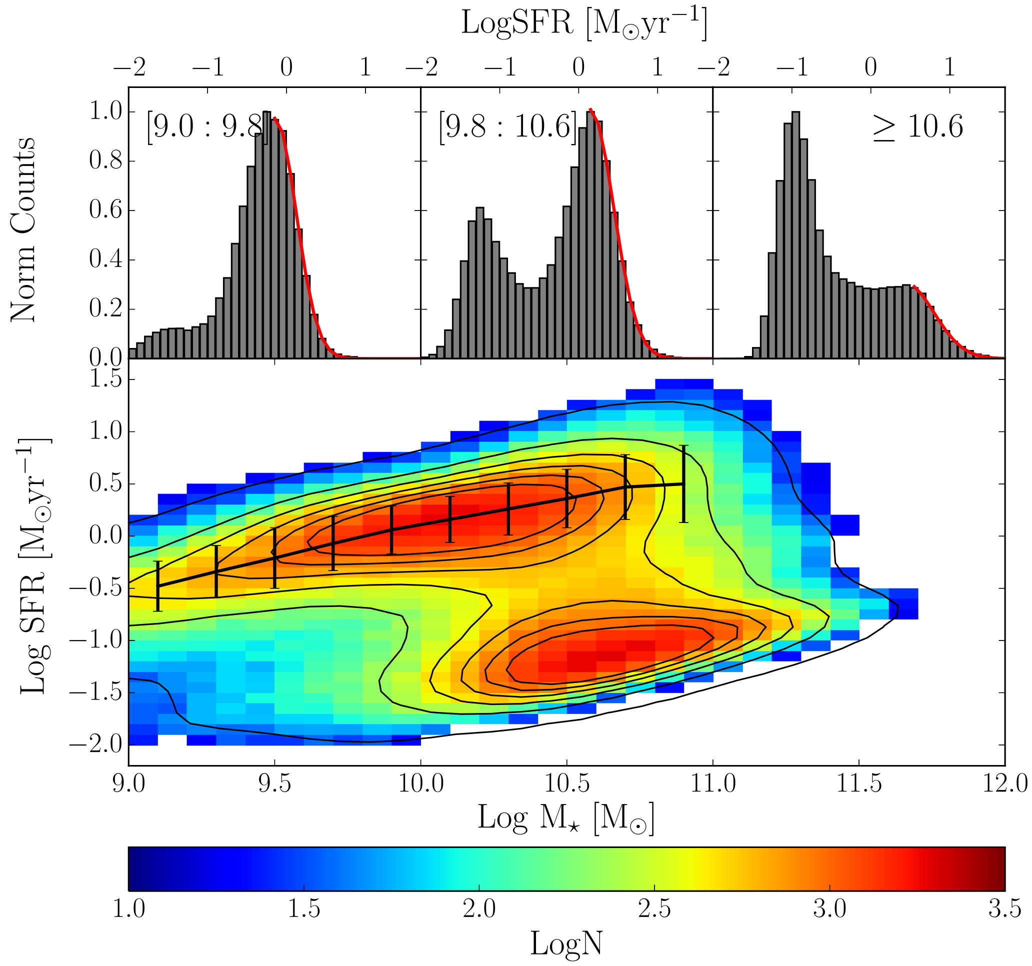

Figure 2.2: Distribution of galaxies in S_{ALL} sample in the LogSFR - Log$M_\star$ plane. *Top panels*: SFR distribution of galaxies in three different stellar mass bins. The red solid line is the result of the gaussian fit to the right-side of the SF peak. *Bottom panel*: LogSFR - Log$M_\star$ plane colour-coded as a function of the number of galaxies in each bin. The MS of SFGs is indicated by the thick solid line, while the error bars mark the 1σ scatter.

Our selection criteria lead to a final galaxy sample of $\sim$ 265,000 galaxies, S_{ALL}. In the bottom panel of Fig. 2.2 we show how galaxies in our S_{ALL} sample populate the LogSFR - Log$M_\star$ plane. In the upper panels we show the distribution of the SFR of galaxies in three bins of stellar mass to better visualise the typical bimodal distribution and its dependency on stellar mass. The thick solid line and error bars in the bottom panel of Fig. 2.2 indicate the position of the MS of SFGs and its 1σ scatter, respectively. Following the example of Renzini & Peng (2015), the MS and its scatter are computed as the mode and dispersion of the SFR distribution in several stellar mass bins. We divide the sample in stellar mass bins of 0.2 dex in the range $9.0 \leq \mathrm{Log}(M_\star/M_\odot) \leq 11.0$. In each bin, we fit

Table 2.1: Main sequence SFRs (first column) and dispersion values (second column) in bins of stellar mass, in Log($M/M_\odot$) (third column).

LogSFR$_{MS}$ [$M_\odot yr^{-1}$]	σ_{MS} [$M_\odot yr^{-1}$]	Log $M_\star$ [$M_\odot$]
-0.48	0.24	9.0:9.2
-0.34	0.25	9.2:9.4
-0.21	0.29	9.4:9.6
-0.07	0.26	9.6:9.8
0.06	0.23	9.8:10.0
0.16	0.22	10.0:10.2
0.26	0.25	10.2:10.4
0.36	0.28	10.4:10.6
0.47	0.31	10.6:10.8
0.50	0.37	10.8:11.0

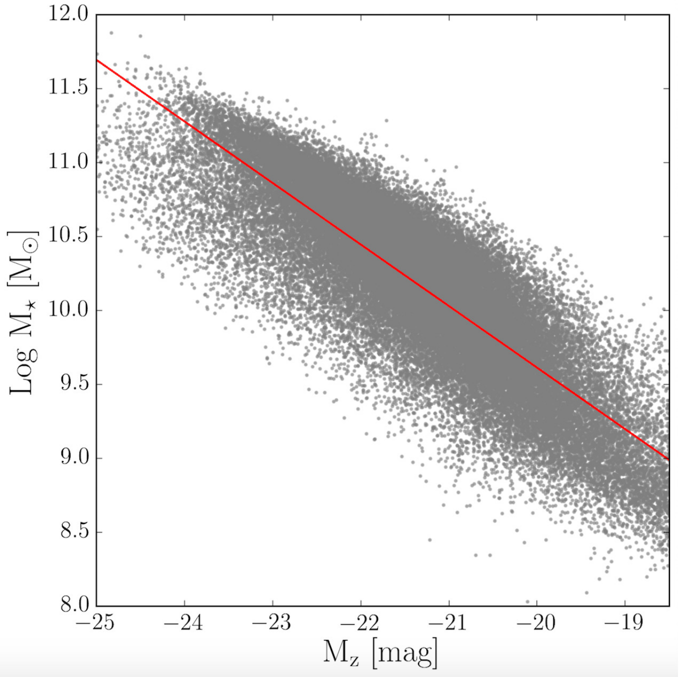

Figure 2.3: Correlation between the absolute z-band magnitude, M_z, and the stellar mass, Log$M_\star$ for the spectroscopic MPA-JHU catalogue at $0.02 < z < 0.1$. M_z has been computed from the SDSS Petrosian magnitude, corrected for extinction.

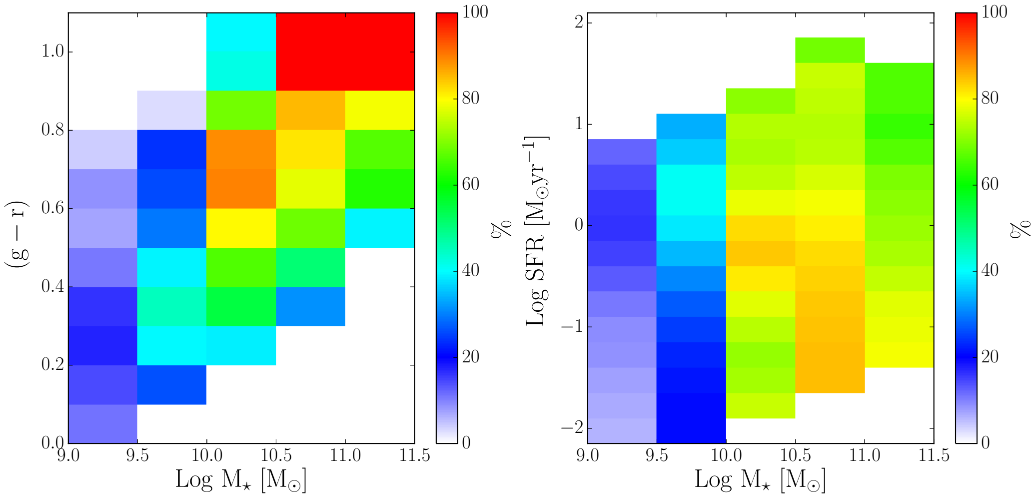

Figure 2.4: Completeness in the $(g-r)$-LogM$_\star$ plane (left panel) and LogSFR - LogM$_\star$ plane (right panel) of the spectroscopic S_{ALL} sample with respect to the parent photometric S_{phot} sample.

with a Gaussian to the right side of SFR distribution (see, as an example, the red fits in the upper panels of Fig. 2.2), to avoid shifts in the peak value caused by the green valley population. We did not compute the MS values for masses M$_\star$ > 10^{11}M$_\odot$ since in this range the distribution is significantly non–Gaussian (Erfanianfar et al., 2016; Whitaker et al., 2012) and cannot be easily disentangled from the tail of the quiescent distribution. The mean (μ) and sigma (σ) values of the Gaussian fit are used as MS and scatter in the midpoint of each stellar mass bin and are summarised in Table 1.

To check for biases introduced by our selection criteria, we study the completeness of our spectroscopic S_{ALL} sample in the LogSFR - LogM$_\star$ plane, by comparing it with the parent photometric sample drawn from the SDSS DR7 in the same region, redshift, and stellar mass range (S_{phot}). The stellar masses for S_{phot} galaxies without spectroscopic data are derived from the z band absolute magnitude, M$_z$, using the best-fit LogM$_\star$ - M$_z$ relation shown in Fig. 2.3 obtained for S_{ALL} (Log(M$_\star$/M$_\odot$)=(-0.42±0.1)M$_z$+1.3(±0.2)). On the other hand, obtaining a measure of the SFR without spectroscopic data is not trivial. We verified that the five SDSS broadbands are insufficient to retrieve a reliable measure of the SFR through the SED fitting technique. Also, the addition of the GALEX UV bands does not help in obtaining a reliable dust correction. Indeed, the scatter between the SFR derived in this manner and the SFR derived from the dust-corrected $H\alpha$ emission of the MPA-JHU catalogue exceeds 0.5 dex. To overcome this issue we use the rest-frame (g-r) galaxy colour as a proxy for star formation activity.

The left panel of Fig. 2.4 shows the (g-r) - LogM$_\star$ plane colour-coded as a function of the completeness level of S_{ALL} with respect to S_{phot}. The completeness in each bin is estimated as the percentage of S_{phot} galaxies that are also in the S_{ALL} sample in the same bin. Completeness is below 50% for $10^{9.0}$M$_\odot$ < M$_\star$ < $10^{10.0}$M$_\odot$. In this stellar mass range it is larger for blue, SFGs than for passive, redder galaxies because of the presence of strong emission lines. For M$_\star$ > $10^{10.0}$M$_\odot$, the completeness is larger for redder galaxies, most likely owing to the strong stellar continuum. To obtain the completeness in the LogSFR - LogM$_\star$ plane we proceed as follows. For every galaxy we get the completeness value by its (g-r) colour and stellar mass (left panel). We then compute the completeness in a given bin of the LogSFR - LogM$_\star$ as the average completeness over all galaxies in that bin. The result is shown in the right panel of Fig. 2.4. Completeness varies between 5% and ~ 20% for galaxies with M$_\star$ < $10^{9.5}$M$_\odot$, where it is larger for blue, SFGs owing to the presence of strong emission lines. For stellar masses in $10^{9.5-10.0}M_\odot$, the completeness of the spectroscopic catalogue reaches 40% on the MS and in its upper envelope, while it decreases to 20% for passive galaxies. For galaxies with M$_\star$ > 10^{10}M$_\odot$, completeness is always higher than 60%, reaches values of ~ 80% on the MS, and is even larger in the passive region with M$_\star$ ~ $10^{10.5-11.0}$M$_\odot$, where galaxies are characterised by a strong continuum.

2.3 Estimate of the central BH mass

In Sec. 1.2.5, while introducing the quenching mechanism, we have seen that in the past years many models were formulated that pointed to a primary role of central SMBHs to stop star formation in galaxies. Currently, only ~ 90 reliable dynamical estimates of central BH masses in galaxies are available, thus making it difficult to draw conclusions, in a statistical sense, on the role of central SMBHs in transforming galaxies from star-forming to passive. Nevertheless, tight correlations have been discovered between the dynamically-measured BH masses and the properties of their host galaxies, particularly concerning the spheroidal component (Gebhardt et al., 2000; Ferrarese & Merritt, 2000; Tremaine et al., 2002; Häring & Rix, 2004; Gültekin et al., 2009; Kormendy & Ho, 2013; McConnell & Ma, 2013; Terrazas et al., 2017). These relationships are a useful tool to study in a statistical way the role of the central BH (in particular of its mass) in large samples of galaxies. In this work, we use the black hole mass (M$_{BH}$) - σ relation of McConnell & Ma (2013) to derive the mass of the central BH for the galaxies in our S_{ALL} sample:

$$\mathrm{Log}M_{BH} = 8.32 + 5.64\mathrm{Log}\left(\frac{\sigma_e}{200}\right) \tag{2.1}$$

where σ_e is the velocity dispersion integrated within $r_{e,bulge}$. This correlation was chosen over the others available in literature as it has been obtained for a mixed morphological sample of galaxies, without excluding pseudobulges. The SDSS velocity dispersions σ_{ap} are computed inside the SDSS fiber aperture of radius $r_{fib} = 1.5$”, and thus have to be extrapolated at $r_{e,bulge}$. Thus, we apply the aperture correction described in Jorgensen et al. (1995) to σ_{ap}:

$$\sigma_e = \sigma_{ap} \cdot \left(\frac{r_{fib}}{r_{e,bulge}}\right)^{0.04} \tag{2.2}$$

where $r_{e,bulge}$ is taken from S11. In the redshift range considered here, the average aperture correction is $\sim$ 14%. Given the spectral resolution of the SDSS spectrograph and typical S/N values, velocity dispersion estimates smaller than ~70 km/sec are not reliable. Thus, to all galaxies with $\sigma_{ap} < 70$ km/sec, we assign a fixed upper limit of $\sigma_{ap} = 70$ km/sec with an error of ±70 km/sec (that will be used in this work to compute weighted averages). We also exclude few galaxies with $\sigma_{ap} > 420$ km/sec, as the SDSS template spectra are convolved to a maximum sigma of 420 km/s. It is important to keep in mind that the value of σ_{ap} (and thus of σ_e) can be contaminated by disk rotation, especially in galaxies that have a significant disk component. When studying the quiescent fraction of the entire population of low redshift galaxies, contamination by rotation does not seem to play a major role (Bluck et al. 2014), as the quiescent fraction as a function of LogM$_{BH}$ is independent on the correlation used (LogM$_{BH}$ - σ or LogM$_{BH}$ - LogM$_{bulge}$) to estimate the BH mass. Nevertheless, some caution is needed when analysing LTGs alone, for which the quiescent fraction at fixed LogM$_{BH}$ is larger for M$_{bulge}$-derived estimates of LogM$_{BH}$, as a consequence of the contamination of disk rotation in σ (Bluck et al. 2014). Fig. 2.5 shows the distribution of LogM$_{BH}$ for all galaxies in the S_{ALL} sample. The peak of the distribution at LogM$_{BH}$ $\sim$ 5.5 M$_\odot$ is caused by our method of assigning an upper limit to all galaxies that have velocity dispersion σ_{ap} lower than the spectral resolution (green histogram in Fig. 2.5).

2.4 Bulge/disk decomposition reliability: comparison with other works

To check the reliability of the S11 B/T classification, we compare it with different morphological classifications, in particular, BUDDA (de Souza et al., 2004, Bulge/disk Decomposition Analysis) and *Galaxy Zoo* (Lintott et al., 2008). Both classifications take the presence of bars into account. Thus, this comparison is particularly interesting to understand how the presence of a bar can bias the S11 B/T estimate.

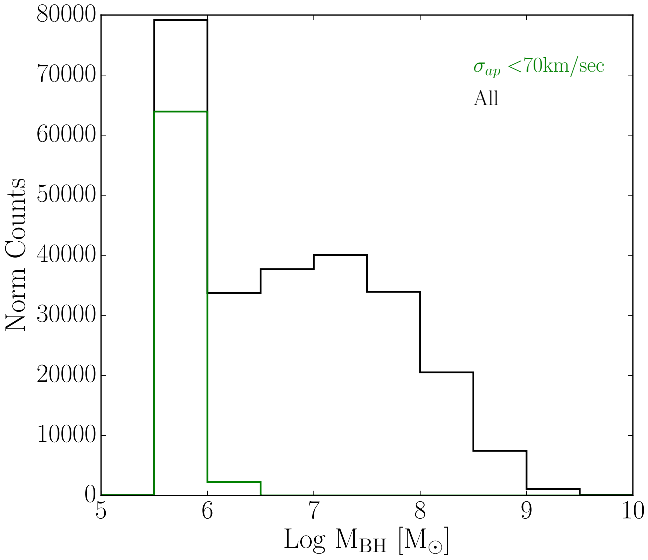

Figure 2.5: Distribution of LogM_{BH} for all galaxies in the S_{ALL} sample. LogM_{BH} has been estimated from the aperture-corrected velocity dispersion σ_e, using the relation of McConnell & Ma (2013).

BUDDA is a fortran code that performs multicomponent decomposition of galaxies. Bulges are fitted with Sérsic profiles and disks are fitted with exponentials. Unlike in GIM2D, in addition to bulge and disk, bars are also modelled with a Sérsic profile. We make use of the public catalogue of structural parameters presented in Gadotti (2009, G09 hereafter), where the BUDDA code has been applied to a sample of 946 spectroscopically confirmed, nearly face-on galaxies, in the range $0.02 \leq z \leq 0.07$ and $M_\star > 10^{10} M_\odot$. The final sample of G09 is clean and optimal for bulge/disk decomposition as the quality of each image has been inspected by eye and the redshift range is low. The S11 and G09 catalogues have 910 galaxies in common (correlation radius $r = 3$"). We compare the B/T ratios of S11 (B/T_{GIM2D}) with the G09 values (B/T_{BUDDA}). Both B/T values have been computed from the r-band images. Results are shown in Fig. 2.6. The red stars are the median values of the whole sample in bins of 0.1 in B/T and the errors are computed as the standard deviation in each bin. We find an overall agreement between the two methods at least below B/T $\sim$ 0.6. GIM2D tends to find slightly higher B/Ts with respect to BUDDA. The blue triangles indicate the subsample of galaxies that are classified as "barred" in BUDDA, while the black circles indicate the "unbarred" subsample. A very good agreement in B/T_{BUDDA} and B/T_{GIM2D} is found for unbarred galaxies, while for barred galaxies, GIM2D tends to estimate higher values of the B/T of almost double at B/T < 0.1 and 20-30% higher at larger B/Ts. Despite this, the overall effect is not dramatic as B/T_{GIM2D} for the whole sample (red stars) does not increase more than 25% because of the inclusion of barred galaxies. This is because of their relatively low

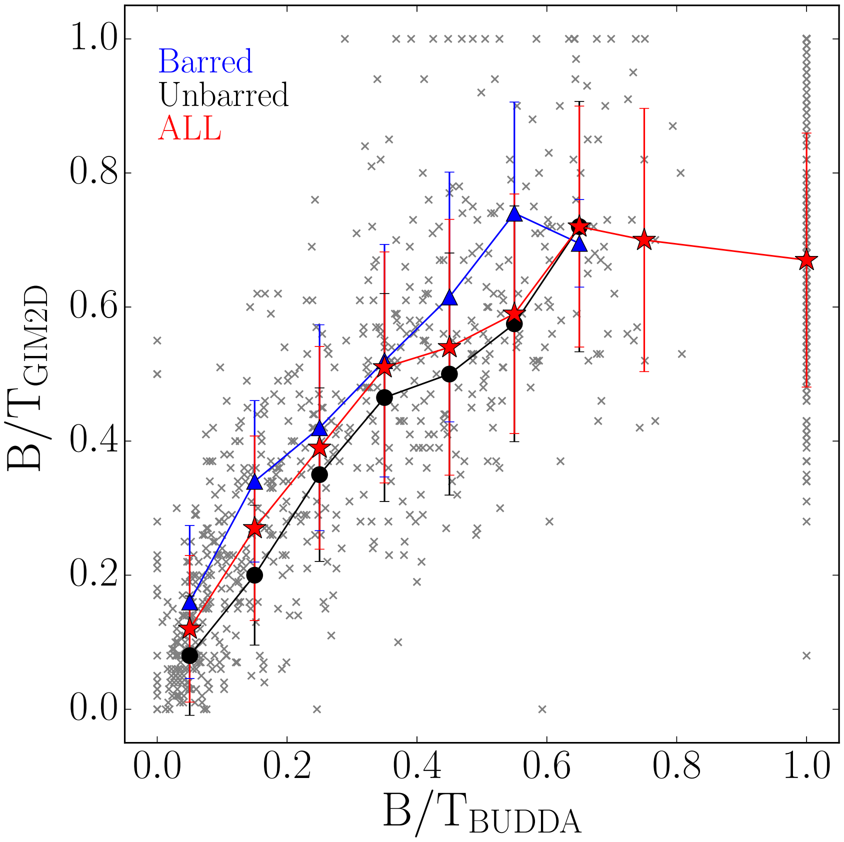

Figure 2.6: Comparison between B/T$_{BUDDA}$ and B/T$_{GIM2D}$. The red stars are the median value of the B/T$_{GIM2D}$ in bins of 0.1 B/T$_{BUDDA}$ for all galaxies that the two catalogues have in common, while the blue triangles and black circles are used for the subsamples of barred and unbarred galaxies, respectively. The error bars are given by the standard deviation in each bin.

percentage, ∼ 30%. Above the B/T ∼ 0.6 threshold, B/T$_{GIM2D}$ tends to flatten to an average value of ∼0.7. This is consistent with the tendency of GIM2D to find an overabundance of small disks in spheroidal galaxies, as pointed out in S11.

We compare GIM2D with the second release of Galaxy Zoo (Lintott et al., 2008), which is a project aimed at classifying "by-eye" the morphology of galaxies in the SDSS Main Galaxy Sample (Strauss et al., 2002). The catalogue provides morphological classification only for ∼ 50% of the parent photometric sample drawn from the SDSS. The remaining half of the galaxy sample is classified with uncertain morphology. In the second release (GZ2; Willett et al., 2013) ellipticals are classified as round, cigar-like, or in-between. Spirals are classified in four classes as a function of the bulge prominency: Sa if they have dominant bulge, Sb for obvious bulges, Sc if the bulge is just noticeable, and Sd if there is no bulge. In addition, spirals are also divided into barred and not-barred cat-

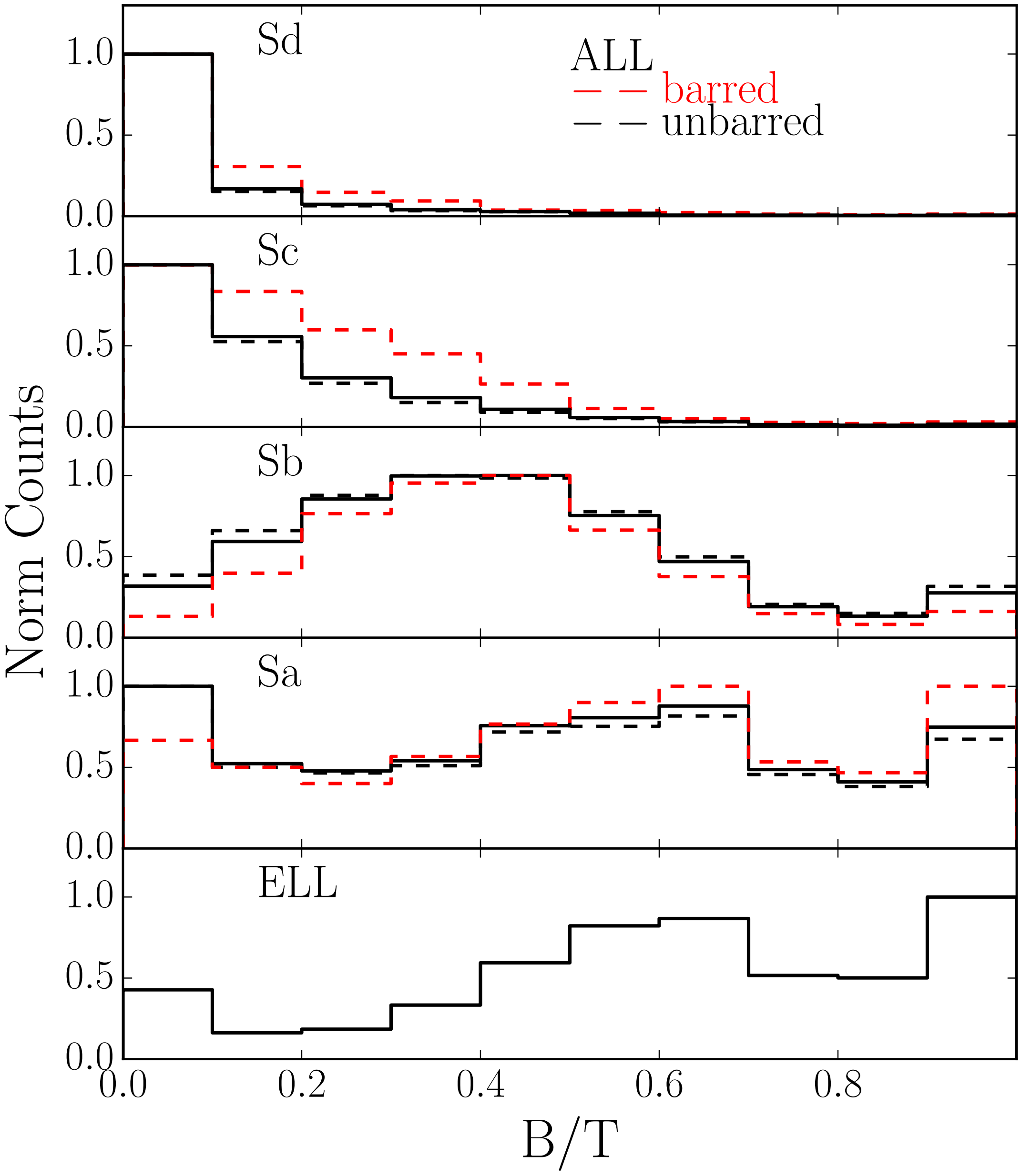

Figure 2.7: Distribution of the S11 B/T in the different morphological classes defined by Galaxy Zoo 2 (from top to to bottom: Sd, Sc, Sb, Sa, and ellipticals). The histograms have been normalised to the peak. The red dashed histograms describe barred spirals, while the black dashed histograms indicate unbarred spirals. The whole population of barred and unbarred galaxies is described by the black solid histograms.

egories. Since edge-on spirals have separate morphological classes in GZ2, we restrict this analysis to galaxies that, in S11, have a disk inclination angle that is smaller than 70° (where $i = 90°$ for an edge-on disk). In Fig. 2.7, we show the B/T distribution of each subcategory, which are identified using the *gz2class* final classification in GZ2[1]. The GZ2 ellipticals, which are considered as a whole regardless of the shape, are characterised by a B/T distribution peaking at B/T ~ 1 and with a second peak at B/T ~ 0.6. We also observe a third, much less significant peak at B/T of 0. Approximately 60% of GZ2 ellipticals with B/T < 0.8 have $P_{PS} \leq 0.32$, thus making the disk component statically significant. These galaxies could be *S0* galaxies that are visually misclassified as ellipticals (Willett et al., 2013; Huertas-Company et al., 2011). Not surprisingly, for GZ2 Sa galaxies, i.e. consistent with an intermediate morphology template (bulge-dominated spiral), the B/T distribution is wide with three peaks, at B/T of 0, ~ 0.5, and 1, respectively. 62% of the *Sa* have B/T between 0.2-0.8, but 22% and 16% of them are classified as pure disks or pure spheroidals according to the S11 P_{PS} statistics. However, we point out that *Sa* galaxies account only for less than $\sim 1\%$ of the GZ2 sample. For *Sb*, *Sc*, and *Sd* the B/T distributions reveal a very good agreement between GZ2 and GIM2D classification. Also, it is clear from Fig.2.7 that the presence of a bar (red dashed line histograms) results in an overestimate of the GIM2D B/T, in particular for *Sc* and *Sd* galaxies. The effect on the whole population is an increase in the mean B/T by a maximum of $\sim 25\%$, as already found in the comparison with BUDDA.

We point out that neither G09 or GZ2 catalogues are suitable for our analysis. While BUDDA does not provide the required statistics, in GZ2, the visual classification is available only for half of the parent galaxy subsample drawn from the SDSS, leading to a high level of incompleteness. Only S11 simultaneously provides the required statistics and completeness. The drawback of using S11 is the uncertainty of bulge/disk decomposition at relatively high values of B/T. Indeed, the comparison with BUDDA and GZ2 shows that S11 find an overabundance of double component systems among galaxies that are classified as pure spheroidal by BUDDA and by the visual classification. Cheung et al. (2013) suggest that among galaxies with B/T > 0.5 only those with $P_{PS} < 0.32$ have a reliable the bulge/disk decomposition. However, such a drastic cut would imply selecting only half of the S11 sample at B/T > 0.5, leading to significant selection effects in our analysis. To overcome this problem, we adopt the following approach. When measuring the mean B/T in the LogSFR - LogM$_\star$ plane, we use a weighted mean, where the weights are based on the errors provided by the S11 catalogue for B/T. Including this error in the weighted mean allows us to take into account the uncertainty due to low S/N and resolution issues. This approach also allows us to propagate the uncertainty of the morphological classification throughout our

---

[1] Alternatively, a similar comparison can be carried out using the vote fractions instead of the *gz2class* parameter, but this leads to a decrease in the number of sources for the comparison, especially in the case of intermediate-morphology galaxies.

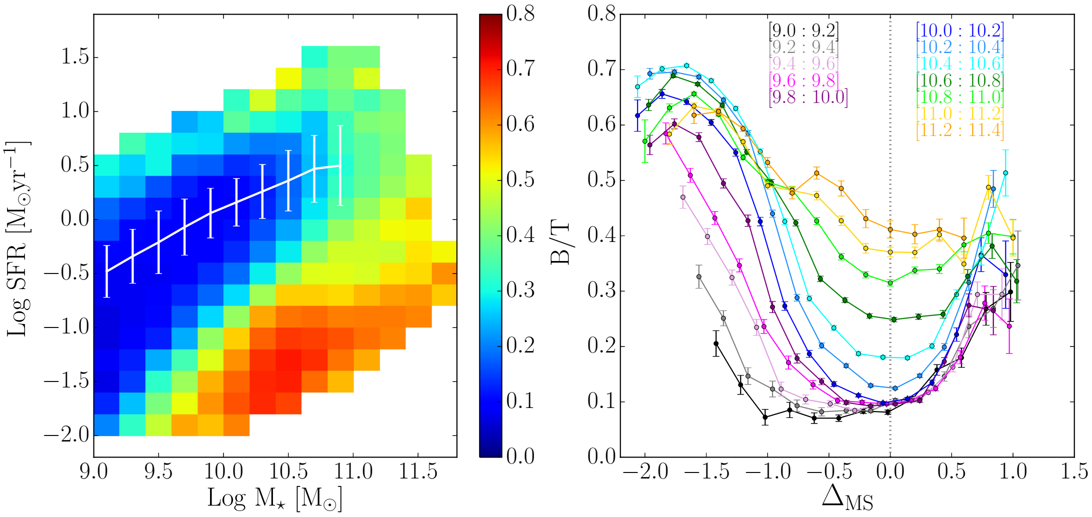

Figure 2.8: *Left panel*: LogSFR - LogM$_\star$ plane colour-coded according to the weighted average B/T in the bin. The white line represents the location of the MS of SFGs, and the error bars indicate its dispersion. *Right panel*: B/T ratio as a function of Δ_{MS} (distance from the MS) in different stellar mass bins. The dotted vertical line indicate the position of the MS. Error bars are obtained via bootstrapping.

analysis. As an alternative approach, and to verify the robustness of our results, we create a reference sample (S_{ref}) in which we keep the B/T as given by S11 for all galaxies with $P_{PS} \leq 0.32$. Instead, galaxies that have $P_{PS} > 0.32$ are consider as pure disks (B/T = 0) when B/T≤0.5 or as pure spheroidals (B/T = 1) when B/T > 0.5. When analysing the colours of the individual components in the LogSFR - LogM$_\star$ plane, we use a sample with robust double component classification by imposing the cut at $P_{PS} < 0.32$.

2.5 Results

In the following sections, we study the galaxy B/T, central BH mass, concentration parameter and bulge/disk colours in the LogSFR - LogM$_\star$ plane. The purpose of this analysis is to better understand the drivers of the MS scatter, and the main differences in galaxy properties between SF and passive galaxies.

2.5.1 The B/T across the LogSFR - LogM$_\star$ plane

In Fig. 2.8 we show the distribution of the B/T values of S_{ALL} in the LogSFR - LogM$_\star$ plane (left panel). Each bin is colour-coded according to the weighted average of the B/Ts in that bin. The width of each bin is 0.2 in both LogM$_\star$ and

LogSFR to account for the average errors on the measurements. The white solid line is the MS and the error bars show the dispersion around it (Table 1).

Fig. 2.8 confirms the result already obtained by Wuyts et al. (2011): the MS is populated mainly by disk-dominated galaxies and the quiescent region by bulge-dominated systems. Intermediate B/T values are found in the green valley and the upper envelope of the MS. We also confirm previous results that the mean B/T on the MS increases as a function of the stellar mass, going from 0.16 at $10.2 < \mathrm{Log}(M_\star/M_\odot) < 10.4$, to 0.21 at $10.4 < \mathrm{Log}(M_\star/M_\odot) < 10.6$, 0.26 at $10.6 < \mathrm{Log}(M_\star/M_\odot) < 10.8$, and 0.32 at $10.8 < \mathrm{Log}(M_\star/M_\odot) < 11.0$. This implies that above $\mathrm{LogM}_\star = 10.2 M_\odot$ the MS is populated by double component galaxies, which is consistent with previous findings (Lang et al. 2014, Bluck et al. 2014, Erfanianfar et al. 2016). When approaching the quiescence region at $\gtrsim 1$ dex below the MS, the B/T further increases to reach an average value between 0.6 - 0.7 for galaxies with $\mathrm{LogM}_\star > 9.6 M_\odot$. For less massive galaxies, the average B/T in the passive region is in the range 0.3 - 0.5. However, this is the region most affected by completeness issues as shown in Fig. 2.4. Thus, it is very likely that a strong selection effect in favour of emission line galaxies is biasing the mean value of the B/T in the weighted mean.

A deeper insight is obtained from a careful analysis of the relation between the residuals around the MS, $\Delta_{MS} = \mathrm{LogSFR}_{MS} - \mathrm{LogSFR}_{gal}$ (where SFR_{MS} is the SFR on the MS and SFR_{gal} is the galaxy SFR), and the mean B/T in different stellar mass bins as shown in the right panel of Fig. 2.8. Contrary to Wuyts et al. (2011), who find a roughly constant value of the Sérsic index $n \sim 1$ around the MS, we observe that the B/T - Δ_{MS} relation exhibits a parabola-like shape within 3σ from the MS with the MS coinciding with the lowest B/Ts at any stellar mass. In contrast to previous results (Wuyts et al. 2011, Cheung et al. 2012), we find that star-forming blue galaxies with a bulge-dominated morphology are not outliers in the diagram but are just populating the upper envelope tail of the MS.

To further investigate how galaxies with different morphologies populate the plane, we study the distribution in the entire stellar mass range of the B/T for galaxies above the MS ($> 2\sigma$), within the MS ($\pm 2\sigma$), in the lower envelope of the MS (2-3 σ below) and in the passive region (3σ below). As shown in fig. 2.9, the MS (black line) is dominated by pure disk galaxies, in which $\sim 60\%$ of the population have $B/T < 0.2$. The large error associated with MS galaxies with $B/T \leq 0.2$ reflects the increase of the B/T along the MS. In the upper envelope of the MS (blue stars), disk galaxies make up only $\sim 30\%$ of the entire galaxy sample, favouring a population of intermediate B/Ts. Similarly, $\sim 35\%$ of galaxies are pure disks in the lower envelope of the MS. Galaxies in the lower and upper envelopes of the MS share the same distribution of galaxy B/T. Among passive galaxies (red triangles), $\sim 70\%$ have $B/T \leq 0.8$. As discussed earlier,

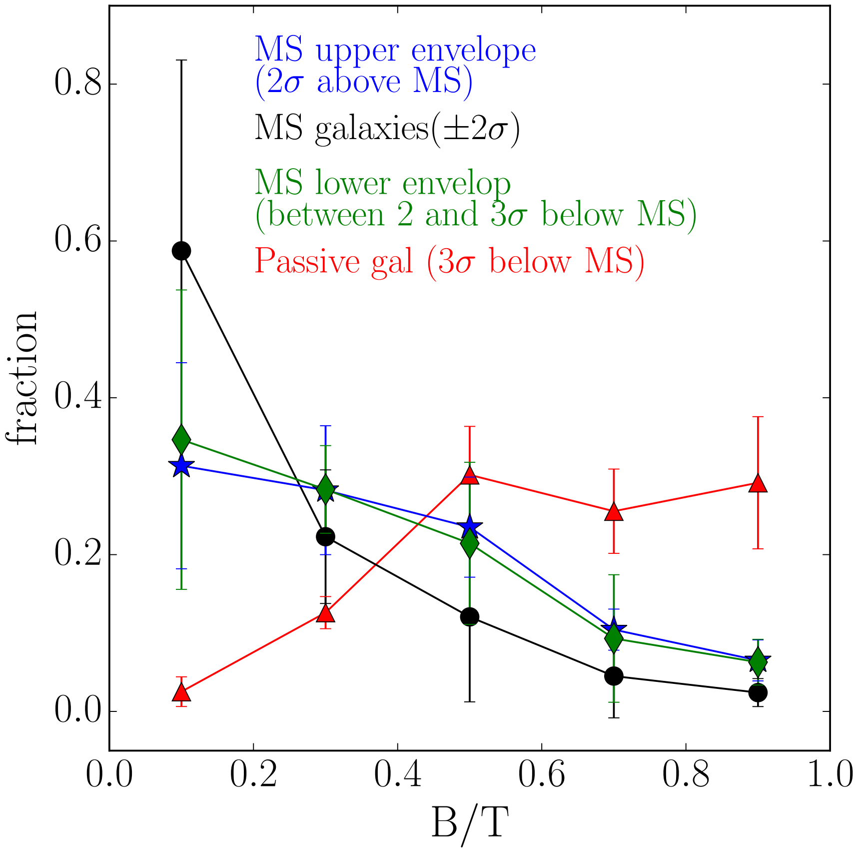

Figure 2.9: Fraction of galaxies as a function of the B/T within the MS (black circles), in the upper envelope of the MS (blue stars), in the green valley, and in the passive region (red triangles). The fraction is estimated as the mean in several bin of stellar mass from 10^{10} to 10^{11} $M_\odot$. The error bars show the dispersion around the mean. The MS upper envelope and the lower envelope (green valley) share the same distribution of galaxies as a function of the B/T: ∼ 40% of the population has B/T > 0.4 vs. 15% of the galaxies in the MS.

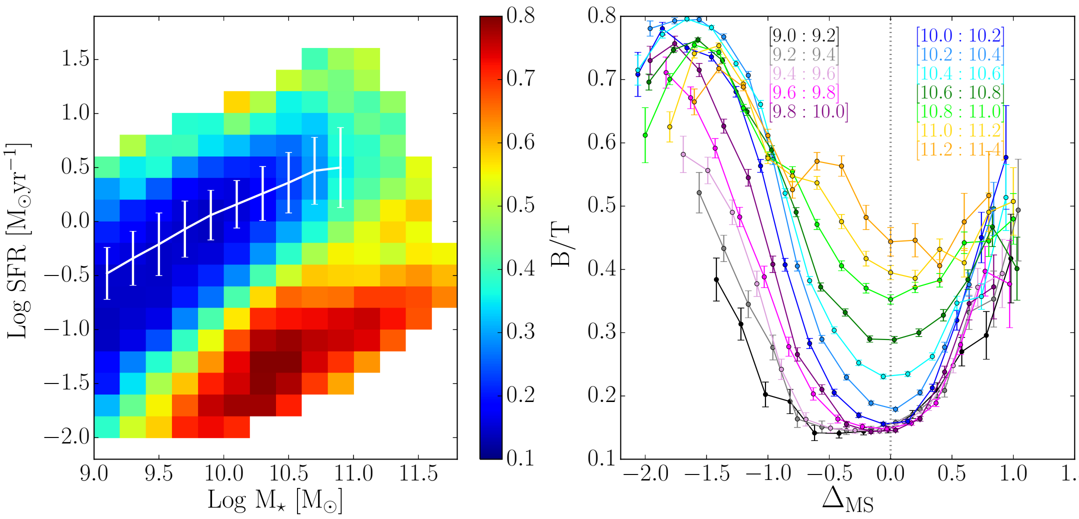

Figure 2.10: Same as Fig. 2.8, but for S$_{ref}$ sample of galaxies. *Left panel*: LogSFR - LogM$_\star$ plane colour-coded according to the weighted average B/T in the bin. The white line represents the location of the MS of SFGs, and the error bars show its dispersion. *Right panel*: B/T ratio as a function of Δ_{MS} (distance from the MS) in different stellar mass bins.

this fraction is contaminated by true spheroidal galaxies for which GIM2D finds a spurious disk. Nevertheless, there is a significant population of passive galaxies with a secure bulge plus disk morphology, as $\sim 45\%$ of all passive galaxies have B/T ≤ 0.8 and $P_{PS} < 0.32$. Also, the fraction of passive galaxies with B/T < 0.2 is negligible, indicating that passive pure disks, if at all present, are outliers of the galaxy population.

To prove the reliability of our results against the bulge-disk decomposition of S11, we performed the following additional tests:

- We repeated the analysis of the mean B/T in the LogSFR - LogM$_\star$ plane for the S_{ref} sample. We recall that the S_{ref} sample is built from the S_{ALL} sample by keeping the B/T as given by S11 for all galaxies with $P_{PS} \leq 0.32$, while the remaining galaxies are considered pure disks if they have B/T $\leq$ 0.5 or pure spheroidals if they have B/T > 0.5. The trends of the B/T in the LogSFR - LogM$_\star$ plane are remarkably consistent with those of Fig. 2.10 for the S_{ALL} sample. We still observe the minimum of the B/T distribution for galaxies that, at each stellar mass bin, are located on the MS. As expected, the increase of the B/T in the passive region is more significant for S_{ref} than for the S_{ALL}, as only $\sim 50\%$ of galaxies with B/T > 0.5 have $P_{PS} \leq$ 0.32.

- We repeated the analysis by limiting the S_{ALL} sample to galaxies with high S/N photometric data and secure S11 classification, by selecting galaxies

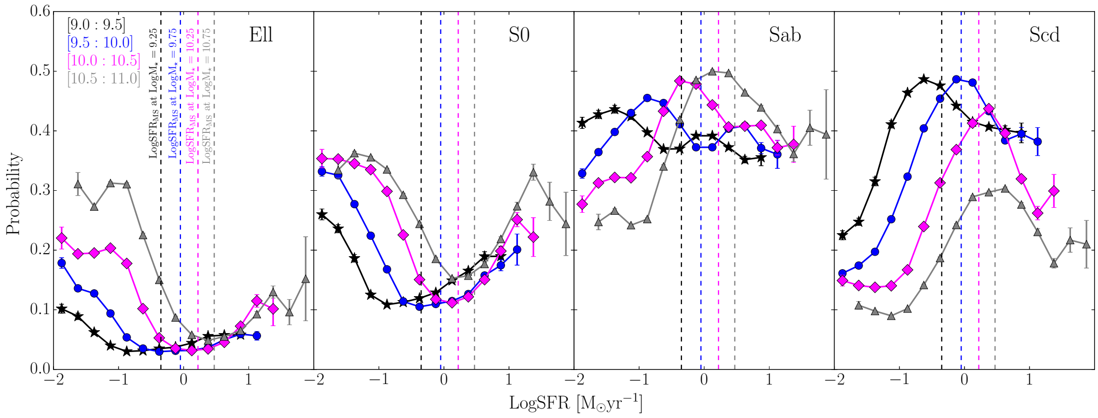

Figure 2.11: Probability of galaxies in the S$_{all}$ sample to be classified as *Ell*, *S*0, *Sab*, and *Scd* (from left to right, respectively) as a function of LogSFR. In each panel, subsamples of galaxies with different stellar masses are shown in different colours: 9.0<Log(M$_\star$/M$_\odot$) <9.5 in black, 9.5<Log(M$_\star$/M$_\odot$) <10.0 in blue, 10.0<Log(M$_\star$/M$_\odot$) <10.5 in magenta, and 10.5<Log(M$_\star$/M$_\odot$) <11.0 in grey, respectively. The dashed lines mark the MS value of LogSFR at the median stellar mass value of the bin.

with a disk scale length larger than 2" to avoid resolution issues (as in Cheung et al. 2013). Also this test confirms the results presented in Fig. 2.8.

- We investigated whether the parabola-shape distribution of the average B/T values around the MS can be recovered by other morphological classifications. In particular, we exploit the automated, vector-based morphological classification of SDSS galaxies presented in Huertas-Company et al. (2011). We decided to use this classification as it does not assign a class to each galaxy, but a probability to each galaxy of being classified in four morphological classes (*Ell*, *S0*, *Sab*, *Scd*). Thus this classification is best indicated to express a continuous transition between different morphological types. From left to right, Fig. 2.11 shows the probability, as a function of the position with respect to the MS, of SDSS galaxies to be classified as *Ell*, *S0*, *Sab*, and *Scd*, respectively. To better underline mass-dependent trends of the classification, in each panel we divided galaxies in four mass bins: 9.0 $<$ Log(M$_\star$/M$_\odot$) $<$ 9.5 in black, 9.5 $<$ Log(M$_\star$/M$_\odot$) $<$ 10.0 in blue, 10.0 $<$ Log(M$_\star$/M$_\odot$) $<$ 10.5 in magenta, and 10.5 $<$ Log(M$_\star$/M$_\odot$) $<$ 11.0 in grey, respectively. The dashed lines mark the MS value of the SFR at the median value of each stellar mass bin. Interestingly, we notice that the probability of a galaxy to be classified as a bulge-dominated galaxy (*S0*) shows the same parabola-like distribution that characterises the B/T at a fixed stellar mass as a function of the SFR. The probability has its minimum on the MS where, on the contrary, a galaxy has the maximum probability to be classified as a disk dominated system. Also the probability of a galaxy of

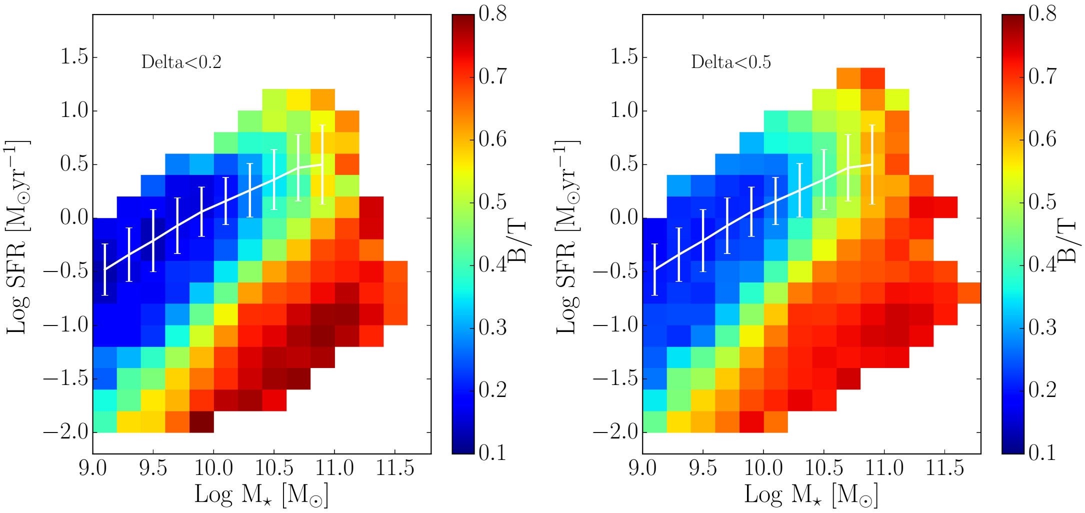

Figure 2.12: *Left panel*: LogSFR - LogM$_\star$ plane colour-coded according to the weighted average mass-derived B/T in the bin. The B/T has been computed from the total, bulge, and disk mass estimates given in Mendel et al. (2013). Only galaxies for which the difference between the total mass and sum of the bulge and disk masses (in units of the standard error) is smaller than 0.2 are shown. The white line represents the location of the MS of SFGs, and the error bars (computed via bootstrapping) indicate its dispersion. *Right panel*: same as left panel, but for galaxies for which the difference between the total mass and sum of the bulge and disk masses (in units of the standard error) is smaller than 0.5.

being classified as *Ell* increases towards the upper envelop of the MS, but less significantly than in the *S0* case.

- We investigated whether the morphological trends are confirmed when using the B/T computed from the bulge and total stellar mass (and not from r and g-band photometry, as done so-far). Bulge, disk and total stellar masses for SDSS galaxies based on the morphological decomposition of S11 have been computed by Mendel et al. (2013) via fitting to broadband spectral energy distributions (SEDs). The formal uncertainties on the total bulge, disk, and total stellar mass are of the order of $\sim$ 0.15 dex, but the authors warn that SED modelling assumptions results in an additional $\sim$ 60% systematic uncertainty. In Fig. 2.12 we show the distribution of the B/T computed from the Mendel et al. (2013) bulge, disk and total stellar mass estimates. As the uncertainties involved are large, we decided to restrict our analysis to two cases: the *left panel* of Fig.2.12 shows only galaxies for which the difference between the total mass and sum of the bulge and disk masses (in units of the standard error) is smaller than 0.2, while on the *right panel* galaxies for which the difference is smaller than 0.5 are shown. Despite the larger uncertainties introduced by the SED fitting assumptions, the morphological trends in the LogSFR - LogM$_\star$ plane observed using the photometry-derived B/T are confirmed when using the mass-derived B/T. Due to the smaller statistics, introduced by the criteria on the difference between the total mass and sum of the bulge and disk masses, the upper envelop of the MS is less populated than in the case of the S_{ALL} sample. Nevertheless, it is clear that the MS falls at the minimum of the B/T distribution at each stellar mass bin, especially at Log($M_{\star}/M_{\odot}$) >10. Galaxies in the upper and lower envelopes of the relation are populated by more bulge-dominated galaxies with respect to MS counterparts at fixed total stellar mass.

2.5.2 The effect of bars

In Sect.2.4 we conclude that S11 and G09 show good agreement for B/T < 0.6 and that the presence of a bar leads to an overestimation of the S11 B/T of 10 - 25%. However, the gradient observed from the peak of the MS towards the upper and lower envelopes of the relation leads to an increase of the mean B/T by a factor ∼ 3-5, depending on the stellar mass bin. Thus, the increase of the mean B/T across the MS is much larger than the overestimation of the B/T due to the bars. Nevertheless, the bars could be preferentially located in certain regions of the LogSFR - Log$M_{\star}$ plane, thus affecting the average B/T value of that region.

To check this, we perform the same analysis as in Fig. 2.8 on the G09 sample (see left panel of Fig. 2.13). We observe a ∼ 25% milder increase of the mean B/T along the MS with respect to the result of Fig 2.8 (mean B/T value of 0.13, 0.19, and 0.23 at stellar masses of $10^{10-10.4}M_{\odot}$, $10^{10.4-10.8}M_{\odot}$, and $10^{10.8-11.2}M_{\odot}$, respectively), which is consistent with the overall effect of overestimation of the S11 B/T from the inclusion of barred galaxies. Because of the relatively small size of the G09 sample, the upper and lower envelopes of the MS are poorly populated. Thus, we limit the analysis of the mean B/T as a function of the distance from the MS to two stellar mass bins, above and below the median mass of the sample ($10^{10.25}M_{\odot}$). We perform the analysis for the whole G09 sample and for the "unbarred" G09 sample (deprived of barred galaxies). The right panel of Fig. 2.13 shows the mean B/T as a function of Δ_{MS} for the two G09 samples in comparison with the mean relation obtained in the same stellar mass bins in S11. The error bars are estimated via bootstrapping technique. We find a perfect match of all relations in the MS region. This indicates that bars do not play a crucial role in the gradient of B/T across the MS. Only in the quiescence region, as expected, the S11 relation shows lower mean B/T with respect to G09 because of the underestimation of S11 B/T for spheroidal galaxies (Fig. 2.6). In addition the barred galaxy sample of G09 shows that the B/T - Δ_{MS} for barred galaxies exhibits the same parabola-like shape. Thus, barred galaxies follow the same trend. This suggests that the presence of a bar on average plays a second order

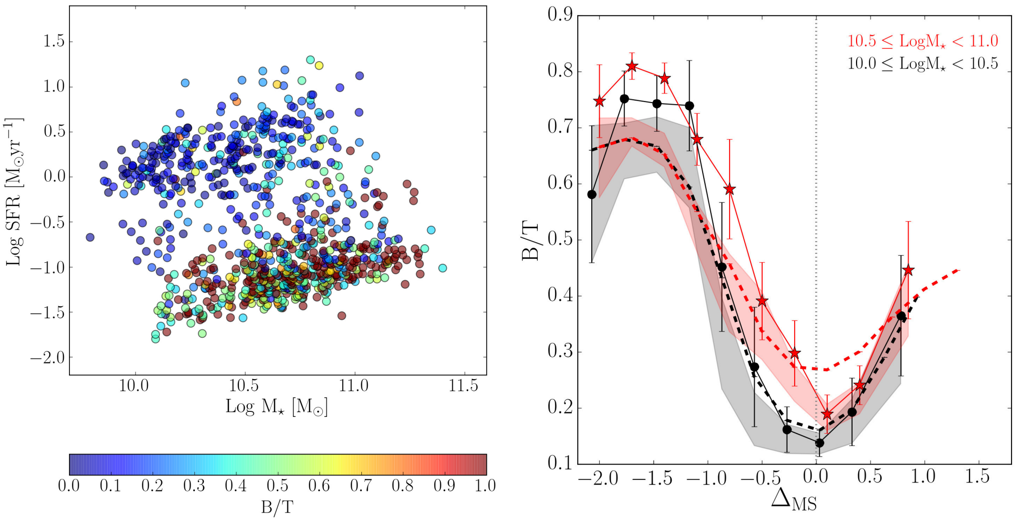

Figure 2.13: *Left panel*: LogSFR - LogM$_\star$ plane for galaxies in the bulge-disk decomposition catalogue of G09. Each marker is colour-coded accordingly to the B/T value of the galaxy. *Right panel*: B/T as a function of the distance from the MS, Δ_{MS}, for the G09 whole sample (shaded region), and for the G09 subsample of unbarred galaxies (solid lines). The sample was divided into two bins of stellar mass, $10.0 \leq$ Log(M$_\star$/M$_\odot$)<10.5 (in black) and $10.5 \leq$ Log(M$_\star$/M$_\odot$)<11.0 (in red). The B/T distributions computed for the S_{ALL} sample are also shown for comparison in dashed lines. The solid vertical lines indicates the location of the MS. error bars are obtained via bootstrapping.

effect with respect to the galaxy morphology.

2.5.3 σ_e, LogM$_{BH}$ and R_{90}/R_{50} in the LogSFR - LogM$_\star$ plane

To investigate the robustness of the morphological trends observed in the LogM$_\star$-LogSFR plane, and to study similarities (or differences) of the bulgy galaxy population in the upper and lower envelopes of the MS, we use the bulge velocity dispersion, σ_e, the black hole mass, M$_{BH}$, and the SDSS concentration parameter, R_{90}/R_{50}. The parameters σ_e and R_{90}/R_{50} are often used to discriminate between classical and pseudo-bulges (see e.g. G09). Classical bulges resemble spheroidal galaxies for their colours and scaling relations. Pseudo-bulges are, instead, outliers in the Kormendy relation (Kormendy, 1977, G09). They tend to be blue-ish, with low velocity dispersion, and with a Sérsic index close to ~ 2.

Fig. 2.14 shows the distribution of galaxies in the LogSFR - LogM$_\star$ plane colour-coded as a function of the weighted average of σ_e in each bin. In order to sample the bulge alone, we select galaxies with B/T ≥ 0.5 and galaxies with $P_{PS} \leq 0.32$ if $0.0 <$ B/T < 0.5. To all galaxies with $P_{PS} > 0.32$ and 0.0<B/T<0.5, thus galaxies for which a bulge component is not statistically needed to fit their surface

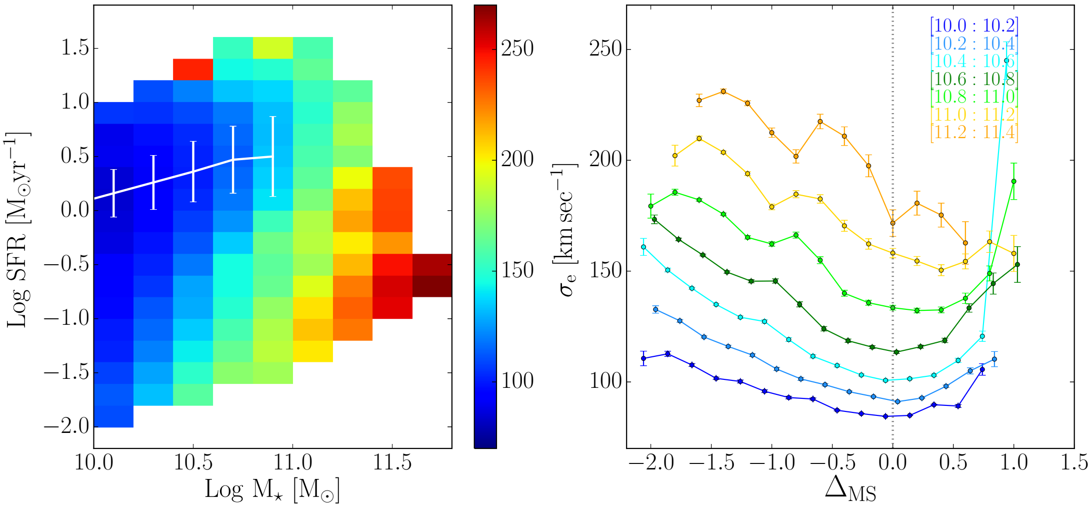

Figure 2.14: *Left panel*: Distribution of galaxies in the LogSFR - LogM$_\star$ plane, in which each bin (0.2M$_\odot$ in M$_\star$ and 0.2 M$_\odot yr^{-1}$ in SFR) is colour-coded according to the weighted average value of the velocity dispersion σ_e in the bin. The white line represents the location of the MS of SFGs. *Right panel*: σ_e as a function of the distance from the MS, Δ_{MS}, in six different bins of stellar mass, each 0.2M$_\odot$ wide. The different bins of stellar mass are indicated with different colours, as defined in the legend of the image, while the grey dotted vertical line represents the location of the MS. The error bars are obtained via bootstrapping.

brightness profiles, we assign a fixed upper limit of $\sigma_{ap} = 70$ km/sec with an error of ±70 km/sec. As galaxies with $\sigma_{ap} < 70$ km/sec are mostly low mass galaxies we focus this analysis on galaxies with Log(M$_\star$/M$_\odot$)≥ 10. The behaviour of σ_e across and along the MS is qualitatively similar to the B/T ratio. At a fixed stellar mass, σ_e has its minimum on the MS, increases towards the upper and lower envelopes of the MS, and reaches its maximum in the quiescence region. Also, the velocity dispersion of MS galaxies increases for increasing stellar mass along the MS, resembling the B/T behaviour. We point out that the exclusion of pure-disk galaxies, which populate the core of the MS, naturally leads to a flatter parabola-like shape for the σ_e distribution as a function of the distance from the MS, Δ_{MS}. No significant differences are observed when dividing the sample in galaxies with disk inclination $i < 45^\circ$[2] and galaxies with $i > 45^\circ$, thus our results are not contaminated by disk rotation.

Following the procedure outlined in Sec. 2.3 we compute M$_{BH}$ for all galaxies with a safe bulge component (galaxies with B/T $\geq$ 0.5 and sources with $P_{PS} \leq$ 0.32 if 0.0 < B/T < 0.5). For all galaxies with 0.0 < B/T < 0.5 and $P_{PS} > 0.32$ we assign a fixed upper limit of $\sigma_{ap} = 70$ km/sec with an error of ±70 km/sec and then proceed with the computation of M$_{BH}$. Fig. 2.15 shows the distribution of galaxies in the LogSFR - LogM$_\star$ plane colour-coded as a function of the weighted

---

[2] The disk inclination angle is 0° for face-on galaxies and 90° for edge-on galaxies.

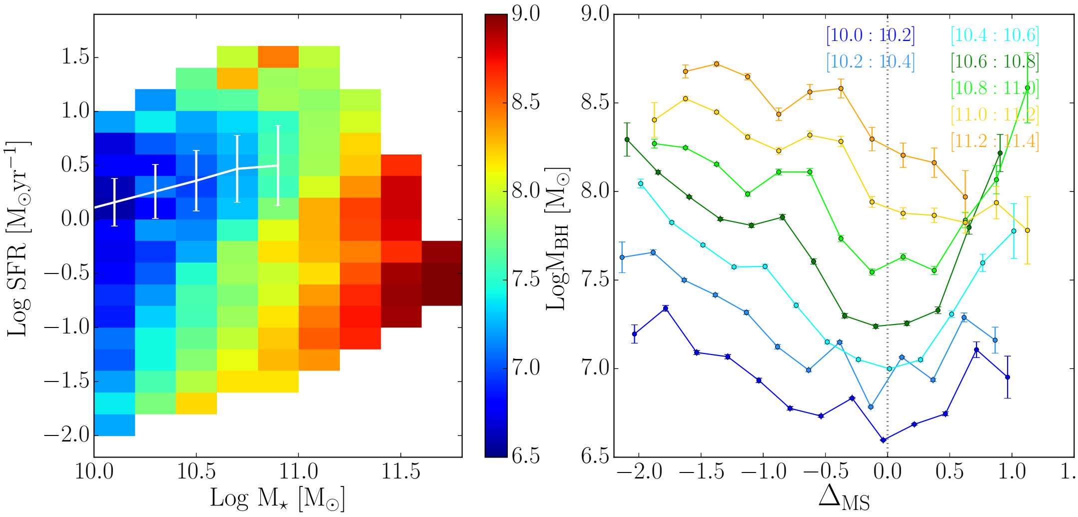

Figure 2.15: *Left panel*: LogSFR - LogM$_\star$ plane colour-coded as a function of the weighted average of M$_{BH}$ in each bin. The white line represents the location of the MS of SFGs, and the error bars its dispersion. *Right panel*: average M$_{BH}$ as a function of the distance from the MS (Δ_{MS}) in different stellar mass bins.

average of M$_{BH}$ in each bin. We find, once again, that the MS coincides with the minimum black hole masses at each stellar mass bin, at least in the stellar mass range in which the MS can be safely determined (M$_\star$ < 10^{11} M$_\odot$) and in which we can trust the estimates of M$_{BH}$. This finding represents a strong proof of the reliability of our results on the morphological distribution of galaxies around the MS. In fact, while the B/T used in the analysis presented in Sec. 2.4.1 is derived from photometry, the black hole masses come from the velocity dispersion, estimated from galaxy spectra. The fact that galaxies located in the upper and lower envelopes of the MS are hosting central BHs with similar masses (on average) also points towards the fact that those bulges might be structurally similar.

The same trend in Fig. 2.14 and Fig. 2.15 is also observed for the concentration parameter, which is one of the most reliable discriminant (G09) between bulges and pseudo-bulges at given B/T. Fig. 2.16 shows that the concentration index reaches the minimum on the MS, and it increases both towards larger and smaller SFRs. In the lower and upper envelopes of the MS the mean value of $R_{90}/R_{50} \approx 2.5$ is consistent with the mean for classical bulges with low values of D4000, as estimated in the same mass range by G09 (see Fig. 20 of G09). Low values of the D4000 index would indicate a relatively young age of the stellar population. Values of $R_{90}/R_{50} \approx 2$, which are consistent with pseudo-bulges, are found only in the core of the MS. In the quiescence region, the mean $R_{90}/R_{50} \approx 3$ is consistent with classical bulges with high values of D4000, i.e older stellar populations. Thus, we conclude that lower and upper envelopes of the MS share the same

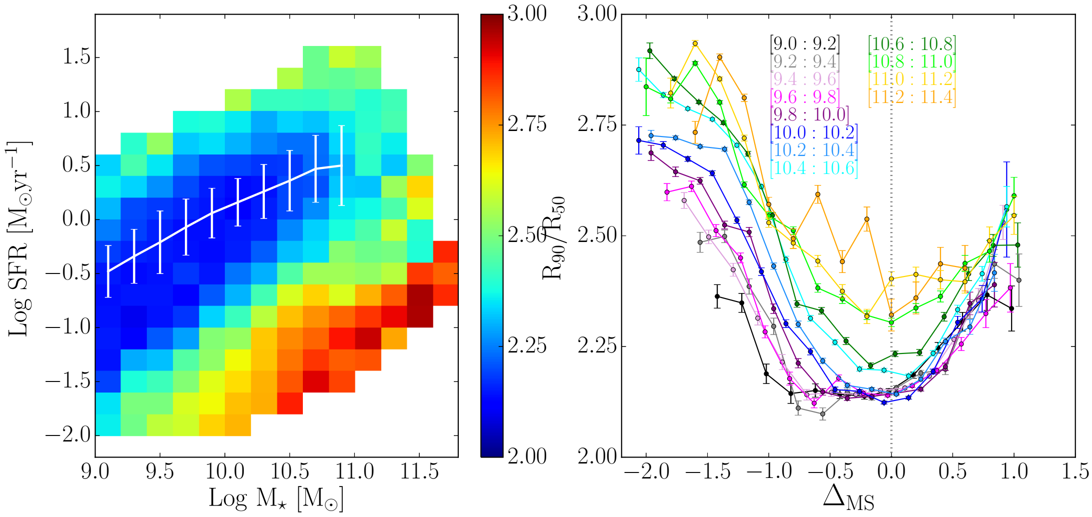

Figure 2.16: *Left panel*: LogSFR - LogM$_\star$ plane colour-coded as a function of the weighted average of the R_{90}/R_{50} ratio. The white line represent the location of the MS of SFGs, and the error bars its dispersion. *Right panel*: R_{90}/R_{50} ratio as a function of the distance from the MS (Δ_{MS}) in different stellar mass bins.

B/T, bulge velocity dispersion, and concentration parameter distributions. Both are populated by intermediate morphology galaxies with classical bulges. The similarity of these distributions could suggest that the scatter around the MS is characterised by different evolutionary stages of the same galaxy population, while the MS itself is mainly populated by pure disk galaxies.

2.5.4 Bulge and disk colours in the LogSFR - LogM$_\star$ plane

The SDSS spectroscopic dataset does not provide any spatial information. Thus to understand whether there is a connection between the SF activity of the individual galaxy components (bulge and disk) and the star formation of the galaxy as a whole, we use the colour of bulges and disks as a proxy of their SFR, while the total SFR of the galaxy is taken from Brinchmann et al. (2004). For this purpose we limit this analysis to the S_{ALL} sample with secure double morphological component, applying the cut at $P_{PS} \leq 0.32$.

In Fig. 2.17 we show the (g-r) colour of the galaxy (upper left panels), disk (upper central panels), and bulge (upper right panels) in the LogSFR - LogM$_\star$ plane. The upper panels are colour-coded as a function of the galaxy or galaxy component colour. The colour in each bin is obtained with a weighted mean. The bottom panels show the dependence of the mean colour of the whole galaxy (left panel), disk (central panel) and bulge (right panel) on the distance from the MS.

The galaxy and disk colours follow similar trends where at any stellar mass bin,

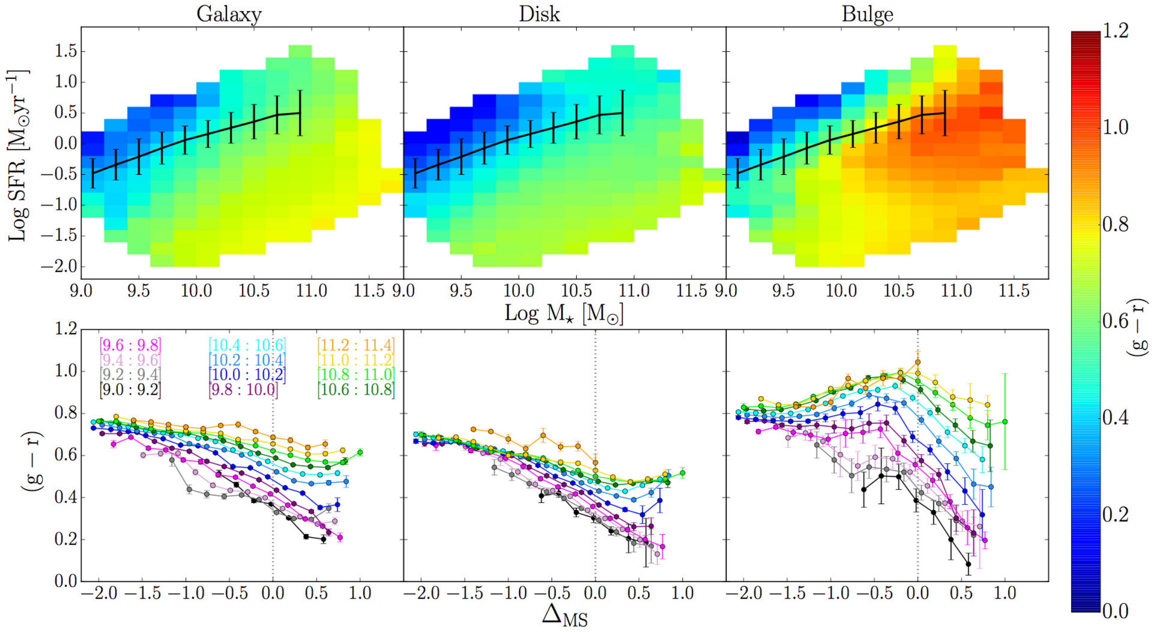

Figure 2.17: Galaxy (left panels), disk (central panels), and bulge (right panels) colours in the LogSFR - LogM$_\star$ plane. In the upper panels, the distribution of galaxies in the LogSFR - LogM$_\star$ plane is colour-coded according to the weighted average (g-r) colour in each bin. The bins are 0.2M$_\odot$ in Log$M_\star$ and 0.2M$_\odot yr^{-1}$ in LogSFR. In the bottom panels, the (g-r) colour is shown as a function of the distance from the MS, Δ_{MS}, in different bins of stellar mass, represented by different colours (same as Fig. 2.8). The error bars in the lower panels are obtained via a bootstrapping.

they anti-correlate with the distance from the MS, getting progressively bluer from the quiescence region to the upper envelope of the MS. The anti-correlation is steeper for the whole galaxy colour than for the disk component. In both cases, the relation flattens progressively towards highest stellar mass bin. The bulge colour shows a different behaviour instead. Up to M$_\star \sim 10^{10}$M$_\odot$, the bulge colour also anti-correlates with the distance from the MS, getting bluer from the passive region to the upper envelope of the MS. In this stellar mass range bulges above the MS are as blue as their disks. However, above M$_\star \sim 10^{10}$M$_\odot$, the relation reverses with the bulge colour getting redder from the passive region up to the MS. After reaching its reddest value, the bulge turns slightly bluer towards the upper envelope of the MS. However, the bulge colour is always redder than the disk even in the upper envelope of the MS. For M$_\star > 10^{11}$M$_\odot$, bulges are always characterised by red colours independent of their position on the LogSFR - LogM$_\star$ plane.

In order to check the bias from dust obscuration, we analyse the average Balmer decrement computed for galaxies with S/N > 8 in both Hα and Hβ (Fig. 2.18). Dust obscuration is not significant for galaxies with stellar masses below 10^{10}M$_\odot$. Hence the trends in colours reflect a trend in SF activity. Very massive (M$_\star \gtrsim$

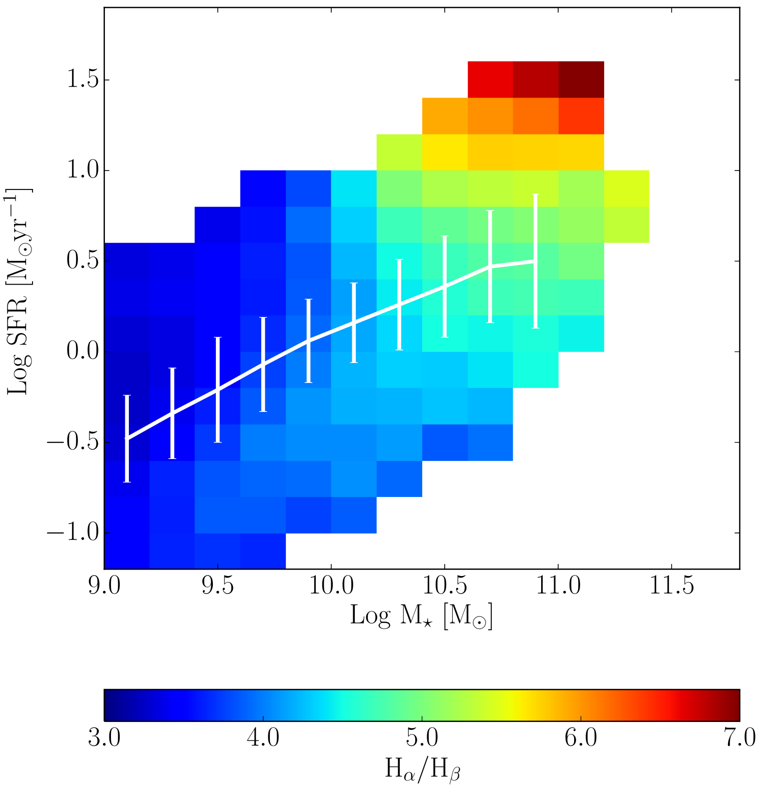

Figure 2.18: Balmer decrement in the LogSFR - Log$M_\star$ plane for galaxies in our sample that have a median S/N ratio per pixel > 8. The white solid line and error bars represent the MS of SFGs and its dispersion.

$10^{10.5}M_\odot$) SFGs in the upper MS envelope exhibit the highest values of Balmer decrement, pointing to a very high level of dust obscuration. This, in turn, would suggest that the flattening of the colour gradients across the MS at increasing stellar mass in all panels of Fig. 2.17 could be due to an increasing level of dust obscuration towards the upper envelope of the MS. We also point out that above $M_\star \sim 10^{10.5}$ $M_\odot$, the very red colour of bulges in the green valley and on the MS cannot be explained by a large level of dust obscuration due to the low average Balmer decrement. We conclude that the bulges in massive MS and green valley galaxies are intrinsically redder than their counterparts in the passive region. This implies that such bulges might be older or more metal rich with respect to bulges in the passive region. In any case, this suggests different evolutionary paths for bulges on the MS, and in the passive region.

The observed trends of the bulge and disk colours at fixed stellar mass with the distance from the MS are also preserved when considering all galaxies in S_{ALL} with $0.2 \leq B/T \leq 0.8$.

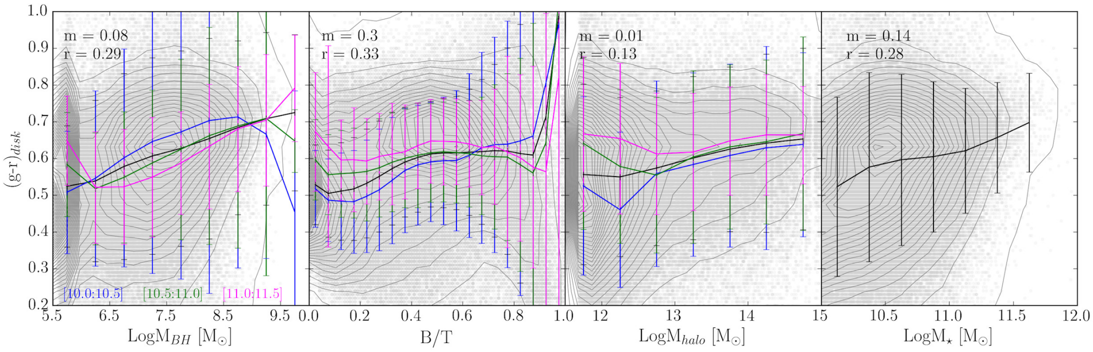

Figure 2.19: From left to right, (g-r) disk colour as a function of LogM$_{BH}$, B/T, LogM$_{halo}$ and LogM$_\star$, respectively. The solid lines connect the average values of $(g-r)_{disk}$ computed in bins of LogM$_{BH}$ (0.5 dex), B/T (0.05), LogM$_{halo}$ (0.5 dex) and LogM$_\star$ (0.25 dex). The colours indicate different stellar mass ranges: $10.0 \leq \mathrm{Log}(M_\star/M_\odot) < 10.5$ in blue, $10.5 \leq \mathrm{Log}(M_\star/M_\odot) < 11.0$ in green, $11.0 \leq \mathrm{Log}(M_\star/M_\odot) < 11.5$ in magenta, and the full range in black, respectively. Errorbars have been computed using the bootstrapping method. In the upper-left corner of each panel, the angular coefficient m and the correlation coefficient r are shown, computed for the entire stellar mass range.

2.5.5 The reddening of the disk

In the previous Sections we analysed the distribution of galaxy morphology across the LogSFR - LogM$_\star$ plane and underlined the importance of considering galaxies as systems composed of components that evolve independently. The analysis of the $(g$-$r)$ colour of disks and bulges revealed that the colour of the individual components plays a critical role in placing galaxies around the MS relation. In addition, we have seen that galaxies moving from the MS towards its lower envelop and towards the passive region have significantly redder disks with respect to MS galaxies. Here we study the disk as an individual galaxy component to understand what causes the colour gradient observed in the right panel of Fig. 2.17. We study the disk color as a function of four properties of the galaxy: the BH mass, the B/T, the mass of the parent dark matter halo, and the stellar mass. The main purpose of this exercise is to understand which actor amongst the central SMBH, galaxy morphology, dark matter halo mass, or galaxy stellar mass plays the most critical role in driving the reddening of the disk and of the whole galaxy. Fig. 2.19 shows the colour of the disk as a function of LogM$_{BH}$, B/T, LogM$_{halo}$ and LogM$_\star$. As the mechanism responsible of regulating the colour of the disk can be different for galaxies at different stellar masses, we show the average $(g-r)_{disk}$ values also computed in three stellar mass bins of 0.5 dex width: $10.0 \leq \mathrm{Log}(M_\star/M_\odot) < 10.5$ in blue, $10.5 \leq \mathrm{Log}(M_\star/M_\odot) < 11.0$ in green, $11.0 \leq \mathrm{Log}(M_\star/M_\odot) < 11.5$ in magenta. The errorbars have been estimated via the bootstrapping technique.

The first panel of Fig. 2.19 shows the $(g$-$r)_{disk}$ - LogM$_{BH}$ correlation. As expected, galaxies hosting more massive SMBHs have redder disks, and this holds at all stellar masses. Black hole masses in the range Log($M_{BH}/M_{\odot}$) < 6.0 are in the vast majority upper limits estimated by assigning to σ_{ap} the value of 70km/sec (Sec. 2.3). The bulk of the population of galaxies hosting SMBHs with Log($M_{BH}/M_{\odot}$) < 6.0 is found at blue disk colours. Interestingly, we found that at a fixed BH mass, galaxies with lower stellar masses have slightly redder colours ($\sim 0.1 mag$) with respect to more massive galaxies. This difference is not significant due to the large scatter of the relation, but suggests that together with the BH mass itself, the ratio between the bulge mass and the total stellar mass (B/T) plays a role in driving the reddening of the disk.

The second panel of Fig. 2.19 shows the correlation between the B/T and the $(g\text{-}r)_{disk}$ colour. This correlation is the one with the largest Spearman coefficient, and thus the one with the smaller scatter. We observe a strong dependence of the disk colour on the B/T, especially for B/T < 0.6, where also different behaviours are observed for galaxies with different stellar masses. In fact, galaxies with Log($M_{\star}/M_{\odot}$) > 11.0 have red disks independently on the B/T. For lower mass galaxies instead, the disk is predominantly blue in disk-dominated systems, and becomes redder with increasing B/Ts. Massive systems (i.e. Log($M_{\star}/M_{\odot}$) $= 11.0$) with low B/Ts (i.e. 0.2) have large BH masses (Log($M_{BH}/M_{\odot}$) $=7.7$, computed from the M_{bulge} - M_{BH} relation of McConnell & Ma, 2013) that characterise red disks (see first panel of Fig. 2.19). Such trends seem to indicate that the B/T is deeply connected to the reddening of the disk, at least till a certain value of the BH mass is reached. In massive galaxies, where BHs are massive also if the structure is disk-dominated, disks are mainly red (and dead).

The third panel of Fig. 2.19 shows the correlation between LogM_{halo} and $(g\text{-}r)_{disk}$. As expected, this relation is the weakest one, as: 1) uncertainties in the determination of LogM_{halo} are very large (see Yang et al. 2007); 2) galaxies at different stellar masses can populate the same dark matter halo, being centrals or satellites; 3) galaxies within the same halo might have spent several Myr in the halo, or might have just recently "fallen into" the halo; 4) the constrain of $M_{halo} = 10^{11.5}$ $M_{\odot}$ imposed on the Yang et al. (2007) catalog confines most of the galaxies in a very narrow host halo mass range between $10^{11.5-12.5}$ $M_{\odot}$, leading to an artificially flatter distribution. The general trends observable from the third panel of Fig. 2.19 reveal that DMHs with Log($M_{halo}/M_{\odot}$) > 13.0 host the bulk of the population of red disks, despite a large scatter, while DMH of lower masses host both red and blue disks. The trends are independent on the stellar mass above Log($M_{halo}/M_{\odot}$) $= 13.0$, while for Log($M_{halo}/M_{\odot}$) < 13.0 less massive galaxies generally have bluer disks and more massive galaxies have redder ones, despite being hosted by a DMH of same mass.

Finally, the fourth panel of Fig. 2.19 shows the correlation between the disk colour and the stellar mass. This relation has a correlation coefficient comparable to the $(g\text{-}r)_{disk}$ - LogM_{BH} one and reveals that more massive galaxies have redder disks than less massive structures. Such a relation also comes naturally considering that the average B/T of the galaxy population is also a monotonically increasing function of the stellar mass. In general, we find very broad and poorly significant correlations between the disk colours and the quantities listed above as indicated by the Spearman coefficients. Nevertheless, the trends observed in Fig. 2.19 indicate that LogM_{halo} is the less efficient quantity to predict red disks amongst the ones studied here. Overall, we find that disks whose parent galaxy is massive, bulge dominated and embedded in massive host halos, tend to have on average redder colours with respect to those in low mass disk galaxies that are embedded in low mass halos.

2.5.6 Driving galaxies below the MS

To further analyse the mechanism responsible for the reddening of the disk, and thus for moving a galaxy from the MS towards its lower envelope and towards the passive region of the LogSFR - $\mathrm{LogM}_\star$ plane, we study the correlations between galaxy properties (LogM_{BH}, B/T, LogM_{halo}) and the distance from the MS, Δ_{MS}. The results are shown in Fig. 2.20. Here Δ_{MS} is positive for galaxies above the MS, and negative for galaxies below the relation.

The first panel of Fig. 2.20 shows the Δ_{MS} - LogM_{BH} correlation. As expected, we find that galaxies below the MS are hosting more massive BHs than MS counterparts. Despite large errorbars we observe that at fixed LogM_{BH} galaxies at lower stellar masses are in general located at larger distance below the MS than more massive structures. This trend confirms what concluded about the $(g\text{-}r)_{disk}$ - LogM_{BH} relation: the importance, together with the absolute value of the BH mass, of the ratio between the BH mass and the total mass of the galaxy in driving the reddening of the disk and in moving a galaxy in the lower envelope of the MS. In other words: while a galaxy of mass $\mathrm{Log(M_\star/M_\odot)} = 10.25$ hosting a BH of mass $\mathrm{Log(M_{BH}/M_\odot)} = 7.5$ is located ~ 1.3 dex below the MS (and corresponds to a B/T ~ 0.7), a galaxy of mass $\mathrm{Log(M_\star/M_\odot)} = 11.25$ hosting a BH of mass $\mathrm{Log(M_{BH}/M_\odot)} = 7.5$ is located ~ 0.5 dex below the MS (and corresponds to a B/T ~ 0.1).

The Δ_{MS} - B/T correlation is shown in the second panel of Fig. 2.20. The Spearman coefficient of this relation is just slightly smaller than the one of the Δ_{MS} - LogM_{BH} correlation, but in this case we do not observe differences in the three stellar mass bins. The bulk of the B/T < 0.3 population is found on the MS, with significant scatter both below and above the relation. Galaxies with $0.3 <$ B/T < 0.7 are mainly found in the passive region, but a significant fraction of the population is located on the relation and in the green valley. Finally, galaxies with B/T > 0.7 are located almost exclusively in the passive region.

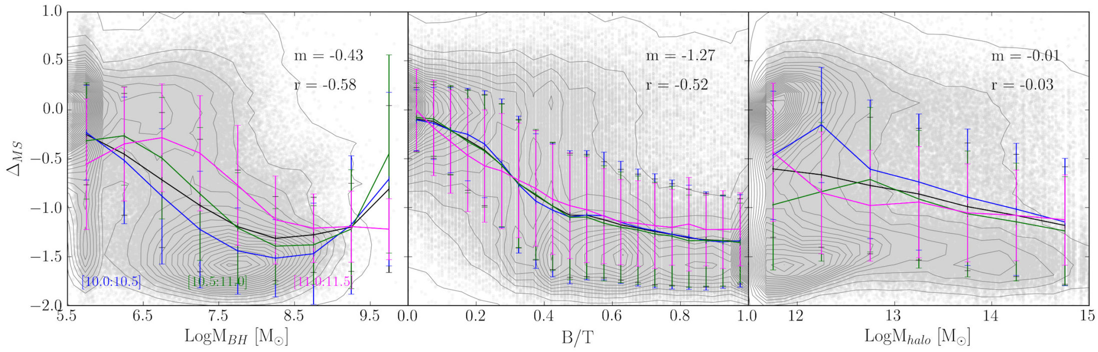

Figure 2.20: From left to right, distance from the MS as a function of LogM$_{BH}$, B/T and LogM$_{halo}$, respectively. The solid lines connect the average values of $(g-r)_{disk}$ computed in bins of LogM$_{BH}$ (0.5 dex), B/T (0.05) and LogM$_{halo}$ (0.5 dex). The colours indicate different stellar mass ranges: $10.0 \leq$ Log(M$_{\star}$/M$_{\odot}$)<10.5 in blue, $10.5 \leq$ Log(M$_{\star}$/M$_{\odot}$)<11.0 in green, $11.0 \leq$ Log(M$_{\star}$/M$_{\odot}$)<11.5 in magenta, and the full range in black, respectively. Errorbars have been computed using the bootstrapping method. In the lower-right corner of each panel, the angular coefficient m and the correlation coefficient r are shown, computed for the entire stellar mass range. In t this Figure, positive values of Δ_{MS} correspond to galaxies located below the relation.

The third panel of Fig. 2.20 shows the Δ_{MS} - LogM$_{halo}$ plane. No significant correlation is found between the two quantities. Halos with LogM$_{halo}$ < 13.0 M$_{\odot}$ host both MS galaxies and passive ones, while more massive halos mainly host passive galaxies. While this general behaviour reflects the morphology-density relation of Dressler (1980), no systematic trend is observed between the distance from the MS and the DM halo mass. This seems to indicate, as concluded in Sec. 2.5.5, that the DMH mass is the weakest quantity to predict the passivity of galaxies amongst the one analysed here and in the previous section.

2.6 Discussion and conclusions

We used the bulge-disk decomposition of Simard et al. (2011) to study the link between the structural parameters of galaxies and their location in the LogSFR - LogM$_{\star}$ plane. We use the colour of bulges and disks to understand how these individual components influence the evolution of the galaxy as a whole. Our sample is drawn from the spectroscopic sample of SDSS DR7, in the redshift range $0.02 < z < 0.1$ and M$_{\star} > 10^{9}$M$_{\odot}$, and the main findings are as follows:

- The MS of SFGs is populated by galaxies that, at every stellar mass, have the lowest B/Ts. At low stellar masses, M$_{\star} < 10^{10.2}$ M$_{\odot}$, MS galaxies are pure disks, while the prominence of the bulge component increases with increasing stellar mass for more massive galaxies.

- The upper and lower envelopes of the MS are populated by galaxies characterised by intermediate B/Ts. This is robust against different decompositions and independent of the modelling of the bar component.
- The MS of SFGs also corresponds to the minimum of the velocity dispersion and black hole mass distribution in a given stellar mass range. This indicate that larger values of the B/T in the upper envelop of the MS with respect to MS counterparts are reliable, and are not the result of a nuclear concentration of star formation within the disk.
- Bulges in the upper envelope of the MS are characterised by blue colours at low stellar masses, or red colours and large dust obscuration at high stellar masses. This is consistent with high SF activity in the central region of the galaxy.
- The study of the mean bulge velocity dispersion, black hole mass and galaxy concentration parameter indicates that galaxies populating the upper and lower envelopes of the MS are structurally similar. The values of the concentration parameter, in particular, suggest that these galaxies are characterised by classical bulges rather than pseudo-bulges.
- In the low mass regime, $M_\star < 10^{10} M_\odot$, disk and bulge colours show a similar behaviour at fixed stellar mass, becoming progressively redder from the upper envelope of the MS to the passive region. Nevertheless, the reddening of the bulge component is steeper than for disks. Disks and bulges become bluer for $M_\star > 10^{10} M_\odot$ when going form the MS towards its upper envelope, despite a less pronounced total variation of colours. The trend of the bulge colour reverses in the lower envelope of the MS, where bulges are redder than in the passive region.
- The population of passive galaxies is largely made of genuine bulge plus disk systems (at least 45%).
- The B/T and $\mathrm{Log}M_{BH}$ are the two quantities that have the strongest correlations with the colour of the disk and the distance from the MS. In very massive galaxies, disks are red independently on the B/T value, indicating that for these systems the BH might be responsible for the shut down of the star formation activity in the disk.

Our results point to a tight link between the distribution of galaxies around the MS and their structural parameters. Contrary to Wuyts et al. (2011) and Cheung et al. (2012), we find that blue bulgy SFGs are not outliers in the distribution of galaxies on the MS. They occupy the upper tail of the MS distribution, leading to a progressive increase in B/T above the MS. In particular, Wuyts et al. (2011) find that the galaxy Sérsic index remains ~ 1 in the region of the MS. We find, instead, that the MS location corresponds to the lowest value of the B/T at any mass. This could be due to the inability of a single Sérsic model (used in Wuyts et al. 2011) to capture small bulges in disk-dominated galaxies. In agreement with previous results, we find a large percentage of bulge-dominated systems in the high-mass SF region, where the MS scatter tends to increase (i.e. Lang et al., 2014; Whitaker et al., 2014; Erfanianfar et al., 2016). However, the B/T - Δ_{MS} relation at fixed stellar mass holds in the stellar mass range 10^{9-11}M$_\odot$, and seems to flatten where the MS itself tends to disappear. We also investigate how the presence of a bar influences the scatter around the MS. Overall we conclude that bars do not affect the scatter of the MS or the B/T - Δ_{MS} relation. In fact, this relation holds for both the unbarred and barred G09 subsamples. This suggests, partly in disagreement with the findings of Guo et al. (2015), that the predominance of the bulge in a galaxy is intrinsically related to the location of a galaxy around the MS, and this is true at any stellar mass independent of the presence of a bar. Nevertheless, we do not exclude the possibility that a large percentage of bars among very massive SFGs can contribute to an increase in the scatter of the MS, as suggested by Guo et al. (2015).

Our study shows that the location of galaxies in the LogSFR - LogM$_\star$ plane and, in particular, with respect to the MS of SFGs, is determined by the combined activity (or inactivity) of the individual galaxy components. This was previously suggested by Abramson et al. (2014), who have pointed out that the MS becomes roughly linear if one assumes that the SF activity takes place only in the disk rather than in the entire galaxy. However, our results suggest otherwise. The effect of normalising the SF activity to the disk mass leads to a completely flat and tight relation only for pure disk galaxies, which, as shown here, dominate the core of the MS distribution. Extending this normalisation to galaxies of intermediate morphology has the additional effect of increasing the scatter by ~ 0.1 dex in any mass bin. We suggest the following explanation:

$$SFR_{gal} = SFR_{disk} + SFR_{bulge} \tag{2.3}$$

thus,

$$\frac{SFR_{gal}}{M_{disk}} = sSFR_{disk} + \frac{SFR_{bulge}}{M_{disk}}, \tag{2.4}$$

where M$_{disk}$ is the disk mass and sSFR$_{disk}$ is the specific SFR of the disk. The last equation leads to the following effects:

- For pure disk galaxies, which dominate the core of the MS, the mass of the disk equals the mass of the galaxy and SFR$_{bulge}$ ~ 0, hence SFR$_{gal}$/M$_{disk}$ = sSFR$_{disk}$. Since the MS is nearly linear, sSFR$_{disk}$-M$_\star$ relation is flat with a very small scatter.

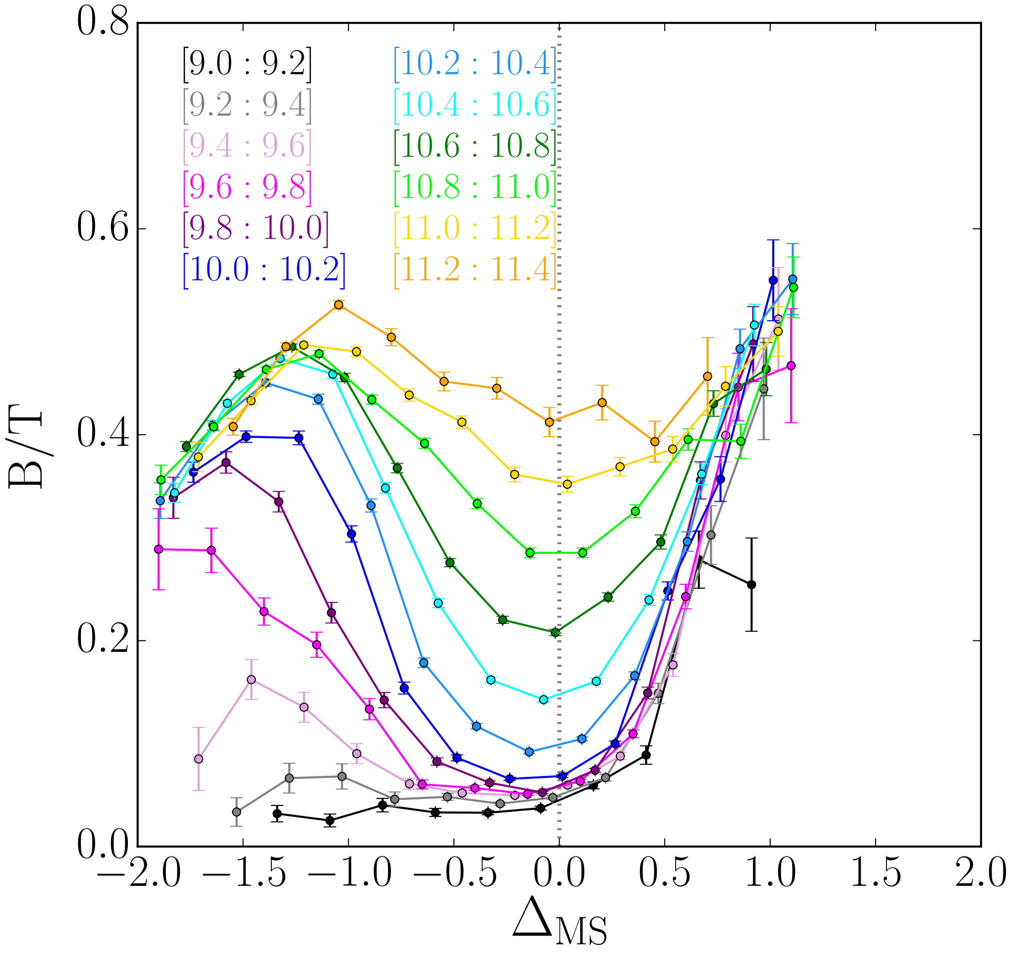

Figure 2.21: B/T ratio, as a function of the distance from the MS, represented by the vertical dotted line. Here Δ_{MS} was computed from the sSFR normalised to M_{disk}. Different bins of stellar mass are indicated with different colours.

- For intermediate B/T galaxies in the upper envelope of the MS, thus with a blue star-forming bulge, $SFR_{bulge} > 0$ and $M_{disk} < M_{star}$. This implies that $SFR_{gal}/M_{disk} = sSFR_{disk} + SFR_{bulge}/M_{disk}$. Therefore such galaxies are displaced well above the $sSFR_{disk}$-$M_{\star}$ relation by the contribution of SFR_{bulge}/M_{disk}. The larger the SFR of the bulge, the larger the displacement.

- For intermediate B/T galaxies in the lower envelope of the MS, thus with a red quiescent bulge, $SFR_{bulge} \sim 0$, hence $SFR_{gal}/M_{disk} = sSFR_{disk}$. They scatter around the $sSFR_{disk}-M_{\star}$ relation in the same way as around the MS.

In Fig. 2.21, we show the relation between B/T and distance from the MS computed as the difference between the $sSFR_{disk}$ of galaxies and $sSFR_{disk}$ of galaxies in the MS. This is carried out for galaxies that are pure disks or have a secure bulge plus disk structure. The B/T trends in Fig. 2.21 are similar to those in Fig. 2.8; there is a steep increase of the mean B/T in the upper envelope of the MS due to the displacement of bulgy SFGs above the $\mathrm{sSFR}_{disk}-\mathrm{M}_\star$ relation. We underline that the B/T in the passive region is lower than that observed in Fig. 5, as here pure spheroidal galaxies are excluded from the sample. We find that the overall effect of neglecting the SF activity of the bulge component is to increase the scatter of the sSFR-$\mathrm{M}_\star$ relation.

It has been proposed that minor mergers or violent disk instabilities could favour the flow of cold gas from the disk towards the galaxy centre and, thus, cause an overall compaction of the system. The high SF activity in the centre would lead to a compact, bulgy, star-forming object (Dekel & Burkert, 2013; Zolotov et al., 2015). Tacchella et al. (2015a) study the evolution of galaxies in this scenario using zoom-in simulations and they find that galaxies at high redshift undergo subsequent phases of compaction and depletion of the gas reservoir, which ultimately leads to quenching. The compaction phase causes high SF in the central region of galaxies, and hence could favour bulge growth. This phase is then followed by depletion from gas exhaustion. Such subsequent phases can move a galaxy across the MS: towards the upper envelope during compaction and towards the lower envelope during depletion. Complete quiescence can be reached once the bulge reaches a given mass threshold corresponding to no more inflows in massive halos or AGN feedback. Our findings on the B/T around the MS and bulge/disk colours can be related to such a scenario and are also consistent with the observed gradient of molecular and atomic gas fraction across the MS, as seen by Saintonge et al. (2016).

We found that, in particular above $\mathrm{M}_\star > 10^{11} M_\odot$, where the spectroscopic completeness is high, the passive region of the LogSFR - Log$\mathrm{M}_\star$ plane is populated either by red spheroidals or by galaxies composed of a red bulge and a red disk. For passive galaxies that have a disk, the progressive decline of the SFR from the lower envelope of the MS towards the quiescent region is mainly driven by the shut down of disk activity, while the bulge is already red and dead when a galaxy is on the MS. Pure red disks are a non significant tail of the passive population, suggesting that the growth of the bulge is somehow related to the decline of the SFR of a galaxy. This is confirmed also by our findings that the B/T is the quantity that correlates the most with the disk colour and the distance of galaxies from the MS, despite a large scatter. Previous works suggest that the reddening of the disk can be caused by the presence of the bulge itself, as predicted by the so-called *morphological quenching* (Martig et al. 2009). For instance, Lang et al. (2014) propose that bulge growth precedes quenching of the SF activity of the whole galaxy and of the disk. Using a similar galaxy sample drawn from the SDSS, Bluck et al. (2014) suggest a prominent role of the bulge component in shutting down the SF activity in galaxies, particularly because of the link between the mass of the bulge and the mass of the central black hole. On the other hand, several works also propose that pure ellipticals and red bulge+disk galaxies might have different evolutionary paths. Schawinski et al. (2014) suggest that for elliptical galaxies the quenching proceeds through mergers and starburst phase, followed by a rapid decline in SFR, for a total duration of 1-2 Gyr from the merging event. On the contrary, in bulge+disk galaxies the SFR would slowly decrease with time as the cold gas reservoir is used and not replenished from cosmological inflows. In this scenario, the quenching of red spirals would take up to few Gyr. This is in agreement with the results of Masters et al. (2010), that studying a sample of red spirals drawn from the Galaxy Zoo catalogue found that these galaxies are characterised by old stellar population and less recent star formation than blue spirals, and are likely to be galaxies in which the cold gas reservoir has been used and not replenished. Nevertheless, the growth of the bulge cannot be the only mechanism driving a galaxy in the passive region, as galaxies with comparable B/T values are found above and below the MS. In other words, while the presence of a bulge seems to be a necessary conditions for a disk to be red, it is not sufficient alone to explain the reddening of the disk and the quenching of its star formation activity. The large scatter observed in the analysed correlations between the disk colour (and distance from the MS) and BH mass - B/T - DMH mass reveals that none of the quantities alone has a prominent role in determining the passivity of a galaxy.

3 The effect of disc inclination on the main sequence of star-forming galaxies

The content of this chapter has been published in Morselli et al. (2016), with only minor modifications being made to the manuscript when adopting it for this thesis. The original manuscript (Monthly Notices of the Royal Astronomical Society, Volume 462, Issue 3, p.2355-2365) was written together with coauthors Alvio Renzini[1], Paola Popesso[2], and Ghazaleh Erfanianfar[2,3].

[1]INAF-Osservatorio Astronomico di Padova, Vicolo dell'Osservatorio 5, I-35122 Padova, Italy
[2]Excellence Cluster Universe, Boltzmannstr. 2, Garching bei Munchen, 85748, Germany
[3]Max-Planck-Institut für extraterrestrische Physik, Gießenbachstrasse 1, Garching bei Munchen, 85748, Germany

3.1 Introduction

In this paper we explore the effect of the disk inclination on the MS slope and dispersion. Indeed, reddening must be substantially higher for edge-on galaxies compared to face-on ones, and therefore more uncertain the extinction corrections to apply to the derived SFRs. We also study the contamination of inclined disks in the lower envelope of the MS, hence for the population of galaxies that are most likely characterised by green colours, and are found in the valley between the blue cloud and the red sequence in the colour-magnitude diagram (Schawinski et al., 2014; Leitner, 2012; Smethurst et al., 2015). Here we illustrate the main results of the experiment, having unveiled an inclination effect much stronger than one could have anticipated from the mere extinction correction.

3.2 Dataset

3.2.1 SFRs and stellar masses

Also in this paper we use the SDSS-DR7 database, specifically taking SFRs and stellar masses from the MPA-JHU catalogues[1]. SFRs have been taken from Brinchmann et al. (2004), where they are derived from the Hα luminosity, corrected for reddening. For galaxies with non-detectable Hα, AGNs or composite galaxies, an estimate of the SFR was derived from the strength of the 4000 Å break (D4000).

The diameter of the fibers of the SDSS spectrograph is $3''$, hence fibers sample only a fraction of each galaxy, especially at high masses and low redshift. Aperture corrections were then applied to produce the total SFRs listed in the MPA-JHU catalogues. As it will become clear in the following section, aperture corrections play an important role in determining the results of the present investigation and therefore we expand briefly on how they were derived for the MPA-JHU catalogue. The procedure basically follows Brinchmann et al. (2004) with one modification. The correction is based on the likelihood of the specific star formation rate for a given set of colours, P(SFR/L$_i$/ colour), constructing it on a grid of bins of 0.05 mag in $^{0.1}(g-r)$ and of 0.025 mag in $^{0.1}(r-i)$, where SFR/L_i is the value of the SFR to i-band luminosity ratio inside the fiber, and $^{0.1}(g-r)$ and $^{0.1}(r-i)$ are the colours, k-corrected to $z=0.1$. The colour of the galaxy outside the fiber was derived by subtracting the fiber luminosities from the total ones, then convolving this estimate of the colour with $P(SFR/L_i/colour)$ to get a value for SFR/L_i outside the fiber. Brinchmann et al. (2004) warned that the results depend on their main assumption that the distribution of SFR/L_i for given $^{0.1}(g-r)$ and $^{0.1}(r-i)$ colours is similar inside and outside the fiber. This assumption may fail for galaxies having a strong bulge component. The mentioned modification consisted in adjusting slightly the SFR having noted that the original procedure overestimates the SFR of galaxies with low levels of star formation (Salim et al., 2007). Stellar masses, $M_\star$, are taken from from the SED fits of Salim et al. (2007). In the following we make use of the MEDIAN values of SFR and $M_\star$, but we have checked that the results are still valid when considering the average (AVG) values.

3.2.2 Bulge-disk decomposition: B/T and disk inclination angle

We use the Simard et al. (2011, S11 hereafter) bulge-disk decomposition of galaxies in the SDSS DR7 photometric catalogue, done with the GIM2D code (Simard

---

[1] http://wwwmpa.mpa-garching.mpg.de/SDSS/DR7/

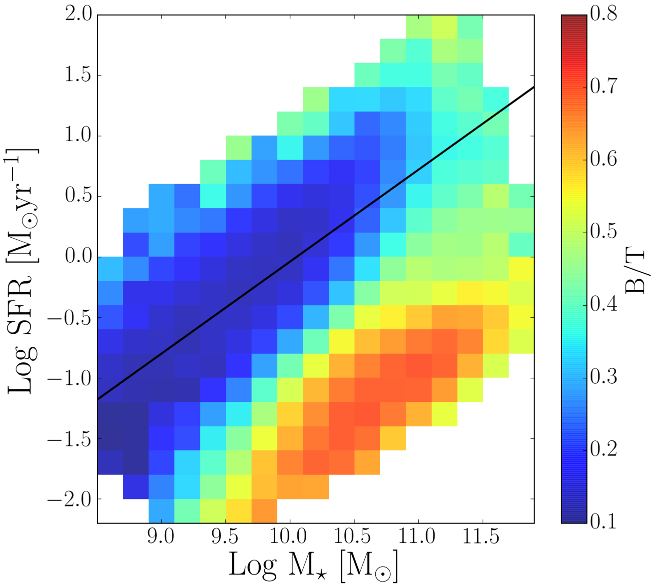

Figure 3.1: The SFR vs. stellar mass plane of galaxies with $0.02 < z < 0.2$, color-coded by the average B/T value in each bin. The bins are 0.2 dex wide in Log(SFR) and 0.2 dex wide in Log($M_\star$), and each bin host a minimum number of 20 galaxies. The B/T values are taken from the Simard et al. (2011) catalogue, and are computed from $r-$band images. The black solid line is the MS relation computed by Renzini & Peng (2015). The B/T has its minimum on the MS, and it increases in the upper envelope of the MS, and for green valley and passive galaxies. Restricting the analysis to B/T$\leq$ 0.5 allows us to avoid from the sample passive galaxies and focus on MS and green valley galaxies.

et al., 2002). In particular, we make use of the decomposition done with a bulge+disk model, where the bulge Sérsic index is fixed to $n = 4$ and the disk component has $n = 1$. This decomposition gives, together with other parameters, the B/T ratio in the r and g bands, and the disk inclination angle, that is $i = 0°$ for face-on galaxies and $i = 90°$ for edge-one ones. Other quantities like the B/T ratio within the SDSS fiber in the g and r bands are also given. In addition, in the S11 catalogue the probability that a double component disk+bulge model is not required to describe a galaxy is stored in the P_{PS} parameter. P_{PS} is a useful quantity to select trustable disk+bulge galaxies. Morselli et al. (2017, M17 hereafter) carried out a comparison of the morphological classification of S11 with others, specifically Galaxy Zoo (Lintott et al., 2011; Willett et al., 2013) and BUDDA (de Souza et al., 2004), and found that the three morphological classifications are in good agreement, especially for low B/T values.

One of the first step of this study is to understand the reliability of disk parameters, specifically the inclination angle, for the galaxies we are interested in. In fact, it is straightforward to understand that disk parameters are more easy to retrieve from disk-dominated galaxies, while for bulge-dominated ones it is not

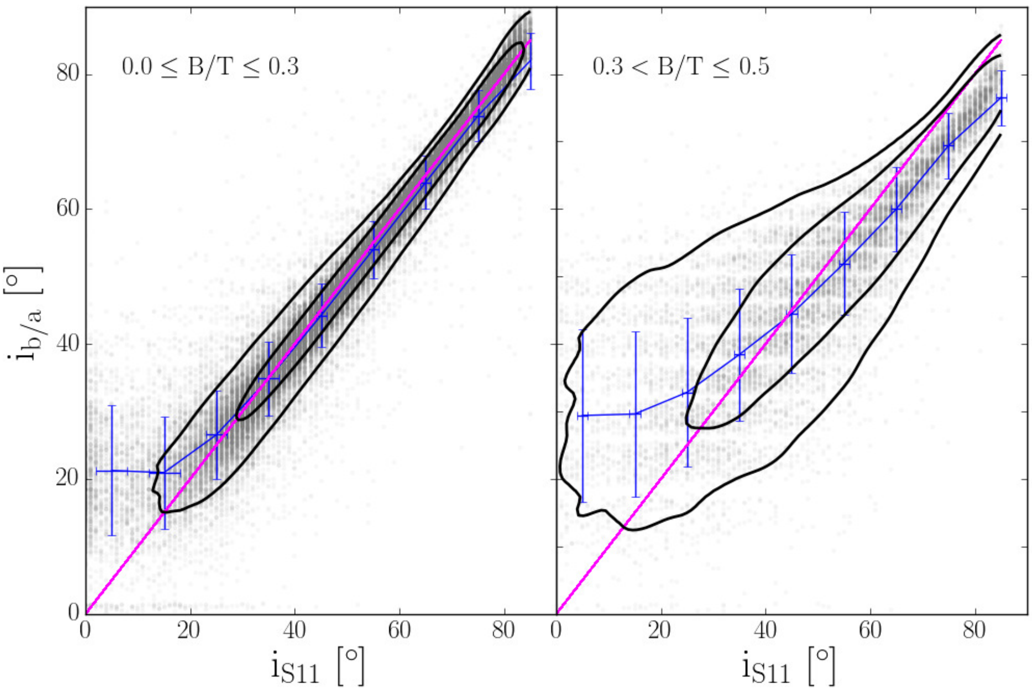

Figure 3.2: Disk inclination angle in the Simard et al. (2011) catalogue (i_{S11}) versus the inclination angle derived from the minor-to-major axis ratio of SDSS, computed from a single $n = 1$ Sérsic profile ($i_{b/a}$). In the left panel, the subsample of galaxies with B/T$\leq$ 0.3 is shown, while the right panel refers to galaxies with 0.3<B/T$\leq$0.5. The magenta line is the 1-to-1 relation, while the black contours encircle the 68% and 95% of the galaxy population. The blue points mark the median $i_{b/a}$ value in intervals of 10° in i_{S11}. The width of the errorbars in the y-direction is the standard deviation of the $i_{b/a}$ distribution in each bin while the width in the x-direction is the median of the errors in i_{S11} in each 10° wide bin. In the lowest B/T bin, the correlation i_{S11} and $i_{b/a}$ is extremely tight and consistent with the 1-to-1 relation. For galaxies with 0.3<B/T$\leq$0.5, the scatter of the i_{S11} - $i_{b/a}$ relation increases, but the slope is still consistent with $m = 1$.

trivial due to the presence of a luminous bulge. The aim of this work is to study the effect of disk inclination on star-forming galaxies and the contamination of inclined disks in the green valley region. Hence, it is useful to try to understand wether the disk inclination angle is reliable for the galaxies we are interested in. M17 shows that for galaxies in the range $0.02 < z < 0.1$ the MS region of the LogSFR - LogM$_\star$ plane is dominated by disk galaxies, with B/T values on the MS up to 0.3 for the most massive galaxies. The average B/T values increase when moving from the MS towards its upper envelope and towards the green valley and quiescent region. Here, for completeness, we repeat the same analysis but considering galaxies in the redshift range of this work: $0.02 < z < 0.2$. Figure 3.1 shows the LogSFR - LogM$_\star$ plane divided in bins that are 0.2 dex wide in LogM$_\star$, and 0.2 dex wide in LogSFR, where each bin is color-coded as a function of the average B/T ratio, as indicated by the color bar on the right. Here and trough

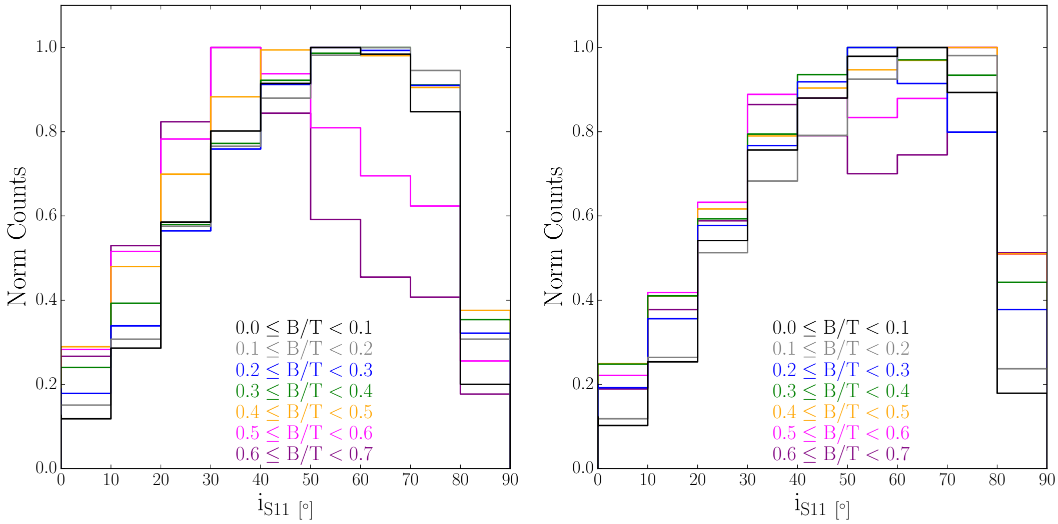

Figure 3.3: Distributions of the disk inclination angle in the S11 catalogue in different bins of B/Ts, indicated by different colours: 0.0≤B/T<0.1 in black, 0.1≤B/T<0.2 in gray, 0.2≤B/T<0.3 in blue, 0.3≤B/T<0.4 in green, 0.4≤B/T<0.5 in orange, 0.5≤B/T<0.6 in magenta, and 0.6≤B/T<0.7 in purple. The disk inclination angles for galaxies with B/T>0.5 is clearly biased by the presence of the luminous bulge, and hence not reliable.

the chapter, we make use of the B/T ratio computed from the r image. In Figure 3.1, the MS is indicated by the solid black line, and its equation is taken from R&P15. It is clear that star forming galaxies are on average disk-dominated, with an increase of the average B/T value on MS at higher stellar mass. It is evident that galaxies with SFRs up to ~ 1 dex below the MS have B/T values that are, on average, smaller than 0.5. Galaxies with the lowest SFRs have, on average, higher B/Ts, due to the presence of a mixed population of red spirals and red ellipticals in the passive region on the LogSFR - Log$M_\star$ plane (M17).

We continue our analysis with the comparison of the disk inclination angle from the S11 catalogue, i_{S11}, and the inclination angle given by the minor-to-major axis ratio (b/a) of the single Sérsic index $n = 1$ model that fits the surface brightness distribution of a galaxy, as from the SDSS pipelines ($i_{b/a} = arccos(b/a)$). This is done in two bins of B/T ratio, to access the reliability of the disk inclination angle in S11. In particular, we divide our sample in galaxies with B/T ≤ 0.3 (left panel of Figure 3.2), and $0.3 <$ B/T ≤ 0.5 (right panel), to check trends with morphology. The contours in both panels of Figure 3.2 encircle the areas where the 68% and 95% of the population are found. The magenta solid line marks the 1-to-1 relation, while the blue points are the median $i_{b/a}$ in intervals of 10° in i_{S11}. The errorbars in the y-direction are given from the standard deviation of the $i_{b/a}$ distribution in each bin, while the median of the errors in i_{S11} in each 10° wide bin give the error bar extension in the x-direction. As expected, for disk dominated galaxies the correlation between i_{S11} and $i_{b/a}$ is consistent with the 1-to-1 relation and the scatter is very small. This means that the GIM2D code is perfectly able to retrieve reliable disk inclination angles, also when a small bulge is present. For $i_{S11} < 20°$ there is a flattening to a value of $\sim 20°$ of the disk inclination angle given from the axis ratio. For galaxies with a larger bulge component, $0.3 <$ B/T ≤ 0.5, the correlation is still consistent with a 1-to-1 relation, but the scatter is larger and the slope slightly smaller than 1. For galaxies with $i_{S11} > 50°$, the disk inclination angle $i_{b/a}$ is always smaller than i_{S11}, and the difference increases for increasing inclination. It is straightforward to understand that this behaviour is the consequence of the fact that a single $n = 1$ Sérsic model is not anymore a good approximation of the surface brightness profile in this range of B/Ts. Especially in the case of nearly edge-on galaxies, even if the disk axis ratio is small (and hence the disk highly inclined), the presence of a luminous spherical bulge in the centre will result in an increase of the axis ratio that comes out from a single Sérsic fit.

The analysis shown in Figure 3.2 tells us that the disk inclination angle of the S11 catalogue is extremely reliable at low B/T values, but we further tested it as a function of morphology. A perfect tool would retrieve the same distribution of disks inclination angles, independently on how dominant the bulge component is. The left panel of figure 3.3 shows the distributions of the disk inclination angle i_{S11} for different subsamples of galaxies, defined by their B/T ratio, as indicated by different colours. For B/T < 0.4 the distributions are similar, with a peak between 50 and 70 degrees. For galaxies with $0.4 \leq$ B/T < 0.5, the distribution is broader, but the peak is still between 50 and 70 degrees. The distribution of disk inclination angles drastically changes when considering galaxies with more dominant bulges: the peak moves between 30 and 40 degrees, due to the presence of a massive, luminous bulge. This behaviour can be the result of a trend of the GIM2D code, well discussed in S11, of finding spurious disks in bulge-dominated galaxies. Hence, we repeated the same analysis of the distribution of disk inclination angles as a function of the galaxy B/T, just considering galaxies for which the statistical F-test confirms the need of a double component model to fit the galaxy surface brightness profile. This is done, as suggested by S11, by considering only galaxies with $P_{PS} < 0.32$, and it is shown in the right panel of Fig. 3.3. We first notice that the peak in the i_{S11} distribution for galaxies with B/T<0.1 slightly shifts between 40° and 50°; this is because when we restrict the sample to galaxies with $P_{PS} < 0.32$ we exclude all the pure disks that do not host a bulge, that have a peak in i_{S11} between 60° and 70°. For galaxies with $0.1 \leq$ B/T < 0.4 and $P_{PS} < 0.32$, the distributions of i_{S11} are very similar to the distributions shown in the left panel. When $0.4 \leq$ B/T < 0.5, the distribution is broader and the peak is found at slightly larger angles than for smaller B/Ts. The distributions become nearly flat between 30° and 70°, with a peak between 70° and 80° for galaxies with B/T ≥ 0.5. This could be interpreted as the fact that it is easier for the code to retrieve the presence of the disk in a bulge dominated

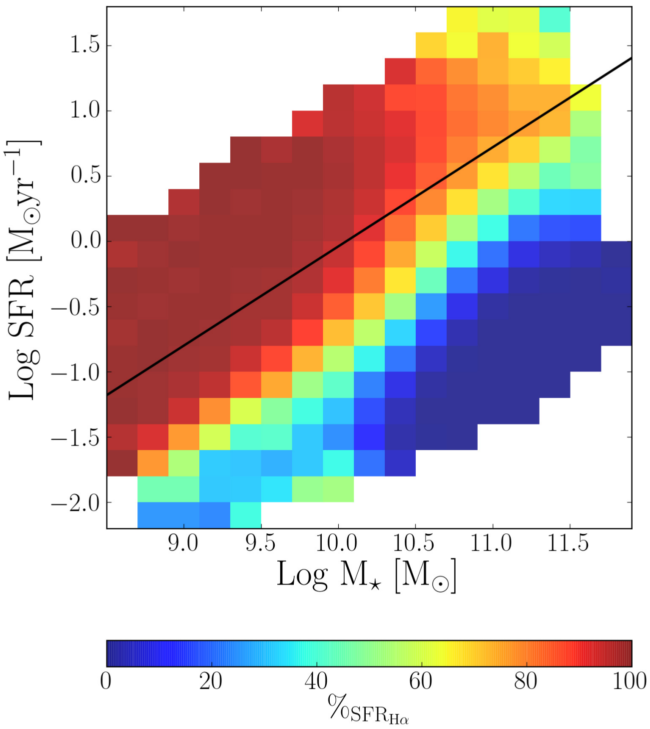

Figure 3.4: The LogSFR - LogM$_\star$ plane color coded by the fraction of galaxies for which the SFR was derived from the Hα flux, as opposed from D4000, as indicated by the color bar at the bottom. The black solid line is the MS computed by R&P15. A fraction always larger of 70% of MS galaxies has SFR from Hα. The fraction decreases when moving from the MS towards its lower envelop, but it is always larger than $\sim 50\%$ for the galaxies we focus on in this work.

galaxy when the disk is nearly edge-on.

This tests tell us that the code is able to retrieve meaningful disk inclination angles up to B/T $\simeq 0.5$ for the whole sample of galaxies. When a galaxy is strongly bulge dominated, the code tends to find spurious disks and to give them low inclination angles, most likely due to the fact that the axis ratio is controlled by the intrinsic shape of the spheroidal bulge.

We conclude that the disk inclination angle in S11 gives us the possibilities to study the disk inclination effects also on those galaxies that have a certain, non dominant (B/T ≤ 0.5) bulge component, giving us a more realistic estimate of the angle with respect to the disk inclination angle from the axis ratio obtain from a single Sérsic model fit. Those galaxies dominate the star forming and green valley regions of the LogSFR - LogM$_\star$ plane, the region we are interested in this work.

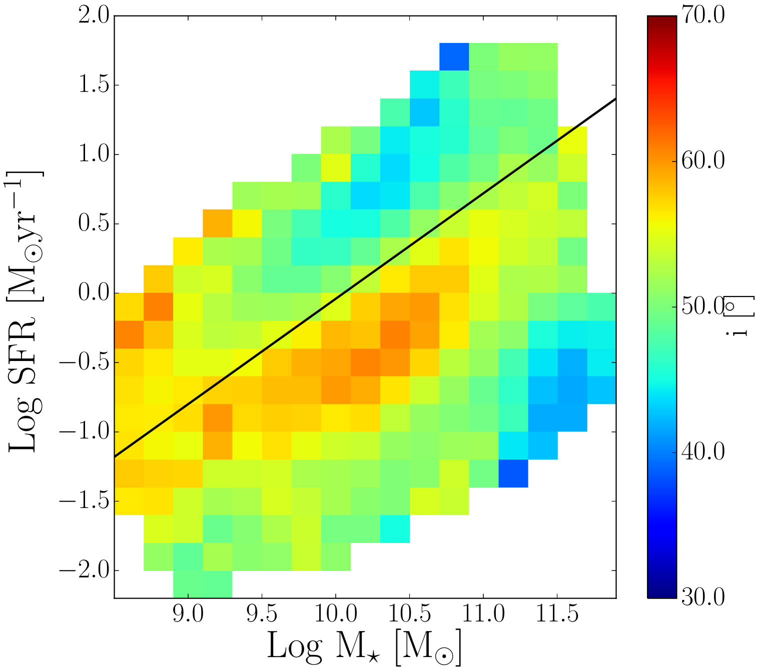

Figure 3.5: The SFR vs. stellar mass plane of galaxies with $0.02 < z < 0.2$ and B/T$\leq$ 0.5, color-coded by the average disk inclination angle (i) in the bin. The bins are 0.2 dex wide in Log(SFR) and 0.2 dex wide in Log($M_\star$), and each bin host a minimum number of 20 galaxies (as in Figure 3.1). The disk inclination angles are taken from the Simard et al. (2011) catalogue. The black solid line is the MS relation computed by Renzini & Peng (2015). The disk inclination angle is not randomly distributed in the plane, as expected if there would be no biases in the determination of the SFRs. On average, galaxies in the lower envelope of the MS relation are characterised by more inclined disks.

3.2.3 The final catalogue

In this work we consider only galaxies with Petrosian extinction-corrected magnitude $m_{Petro_r,corr} \leq 17.77$, which is the completeness limit of the Main Galaxy spectroscopic sample, $0.02 < z < 0.2$. We excluded active galactic nuclei (AGNs) from the sample, since SFR rate estimates could be affected by AGN emission lines. To do so, we consider only objects whose spectra are classified as *galaxy*, excluding galaxies with *SUBCLASS* of AGN; these criteria led to the exclusion of $\sim 4\%$ of sources which otherwise would have fulfilled the other selection criteria. Also, we focus our analysis on galaxies that have $8.5 \leq \mathrm{Log}(M_\star/M_\odot) \leq 11.25$. The SDSS DR7 galaxies that satisfy all those criteria are $\sim$ 520,000. Given the tests on the reliability of the disk inclination angle as measured in S11 and of the distribution of the B/T ratio in the LogSFR - Log$M_\star$ plane, we focus mainly on the $\sim$ 320,000 galaxies with B/T $\leq$ 0.5. However, we will briefly mention also how the derived SFRs correlate with the axis ratio of bulge-dominated (B/T $>$ 0.5) galaxies.

To correct for incompleteness at low stellar masses, we applied the V/V_{max} correction, where V_{max} is the maximum volume at which a galaxy with a given Hα flux would still be detected with S/N $\geq$ 3. We underline here that this correction, based on Hα, is valid only for galaxies whose SFR comes from the Hα flux. This is a good approximation since the SFR comes from Hα for the large fraction of low stellar mass galaxies for which incompleteness needs to be taken into account. Figure 3.4 shows the fraction of galaxies in our sample with SFR from Hα, as a function of their position in the LogSFR - LogM$_\star$ plane. This fraction is always very large on the MS, with average values always above 70%. For galaxies with M$_\star$ $< 10^{10} M_\odot$ this fraction is $\sim$ 100% on the MS and its upper envelope , while it decreases to 50% at $\sim$ 1 dex below the MS. Hence we can safely say that the incompleteness correction accounts for the majority of galaxies in the region of the LogSFR - LogM$_\star$ plane in which we are interested. At higher stellar masses, the fraction of star forming galaxies with SFR from Hα decreases on the MS, and more rapidly when moving from the MS to its lower envelop, but here the spectroscopic completeness is high, hence the correction is not needed. It is nevertheless important to underline that the SFR from D4000 should be less affected by dust extinction than SFR from Hα. The systematic change along the MS in the fraction of SFRs derived from Hα (or D4000) may introduce a bias in e.g., the derived slope of the MS or in the population of the green valley, an aspect we do not investigate further in the present paper.

3.3 Inclination effects on the SFR - M$_\star$ relation

If we had a perfect tool to derive the SFR of galaxies the results should be independent on their aspect with respect to the observer. In practice, however, our tools are not perfect. Edge-on galaxies are obviously more affected by reddening and extinction than face-on ones and reddening corrections are therefore more uncertain. In addition, self-extinction is not the only disk-inclination dependant effect that can result in a biased SFR estimate. In fact, for galaxies that have intermediate morphology, the inclination of the disk translates on the portion of the disk that enters the fiber, as we will discuss later. For example, a face-on galaxy with B/T $\sim$ 0.5 at low redshift, will have a fiber SFR that is substantially given by the bulge, and hence it is likely to be extremely low. On the contrary, when observing the same galaxy when the disk is edge-on, the fiber SFR will also have the contribution of the disk, even if it might be underestimated due to its internal extinction. To obtain the total SFR of a galaxy, a substantial aperture correction is applied, which relies on simplifying assumptions that may introduce errors and biases.

Here we want to study the effects of disk inclination on the determination of the galaxy SFR and, as a consequence, on the slope, shape and dispersion of the MS

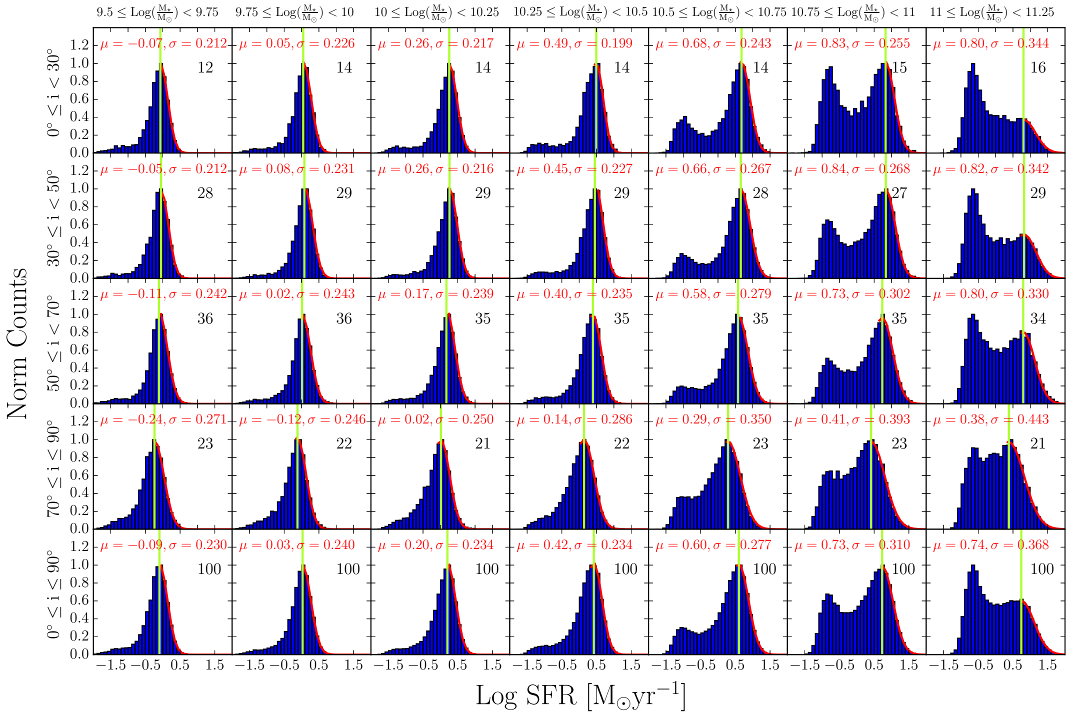

Figure 3.6: Total SFR distributions in bin of stellar mass (different columns, increasing from left to right) and in bins of disk inclination angle (different rows, increasing from top to bottom), for galaxies with B/T≤0.5. The bottom row shows the whole galaxy sample, i.e. $0° \leq i \leq 90°$. The right part of the SF distribution has been fitted with a gaussian (in red), and the best fit *mean* and *dispersion* values are written in each panel in red. In each panel, also the fraction of galaxies is shown. The green lines mark the position of the mean value of the best-fit gaussian. The number in each panel is the percentage of galaxies in that bin of disk inclination angle and total stellar mass. For a given stellar mass bin, the peak of the SF distribution shifts at lower SFR values with increasing disk inclination angle, and the dispersion of the distribution increases.

of SF galaxies. We start our analysis by showing how the disk inclination angle varies along the LogSFR - LogM$_\star$ plane for the galaxies in our sample. Results are shown in Figure 3.5, where each bin in stellar mass and SFR has been colour-coded as a function of the average value of the disk inclination angle, i_{S11}, in each bin. The black solid line is the MS of R&P15. It is clear that the highest average disk inclination angles run parallel to the MS, but offset by about 0.5 dex. Galaxies that are above the MS are characterised by lower average disk inclination angles. For SFRs ∼1 dex below the MS, the average inclination angle is between $\sim 45° - 55°$, i.e. in the range of the most probable disk inclination. The behaviour of the disk inclination angle in the LogSFR - LogM$_\star$ plane clearly reveals the presence of biases in the estimate of the SFRs.

To further investigate the dependence of the SFR estimate on the disk inclination angle, we plot in Figure 3.6 the distribution of the SFR in different bins of stellar mass (0.25 dex wide), increasing from left to right, and in different bins of disk inclination angle (from top to bottom, as indicated), for galaxies with B/T $\leq$ 0.5. The entire sample ($0° \leq i \leq 90°$) is illustrated in the bottom row. All the panels show the classical bimodal distribution for SF and for quenched galaxies, with the quenched peak becoming progressively more prominent with increasing mass. The star-forming peaks have been fitted with a gaussian that is shown in red, and the resulting mean (μ) and dispersion (σ) values are reported in each panel together with the fraction of galaxies in each bin. We fit only the right part of the SF distribution, to avoid a shift of the mean due to the likely presence of quenching galaxies in the *green valley.* We can identify different effects of the inclination. For each stellar mass bin, the peak of the SFR distribution moves to lower values with increasing inclination angle. This difference in the peak position between lowest and highest disk inclination bins is ~ 0.2 dex for galaxies with $\mathrm{Log}(M_\star/M_\odot) \leq 10.25$, and it increases with increasing stellar mass, up to ~ 0.4 dex for the most massive galaxies. Also, for a fixed stellar mass bin the dispersion of the star-forming gaussian increases with increasing disk inclination angle. This effect is relatively small (up to 0.1 dex in the most massive galaxies). A consequence of the shift to lower values of the SF peak is the progressive partial filling of the green valley, which almost disappears for the most massive, nearly edge-on galaxies. When considering the whole sample, irrespective of inclination, the distributions closely resembles those for the most probable disk inclination, i.e. $\sim 50°$. For the most massive galaxies, $\mathrm{Log}(M_\star/M_\odot) > 10.5$, a change in the relative strength of the two peaks in the SFR distribution, the quenched and star forming ones, is also noticeable. With the disk inclination angle increasing from 0° to 90°, the peak of passive galaxies becomes less prominent, in favour of a more significant SF peak. More massive MS galaxies are, on average, more bulge dominated, hence the fiber samples different portions of the disk depending on the disk inclination angle. For nearly face-on galaxies the fiber may sample just the passive bulge and the whole galaxy is assigned a low SFR. With increasing disk inclination angle, the portion of the disk that enters the fiber increases, so the galaxy is recognized as star-forming and assigned a high SFR. This is further discussed in Section 4.1.

As discussed in Section 3.2, a key step in determining the SFR of a galaxy is the aperture correction, hence we now check whether the shift in the SF peak is present also when considering the fiber values, i.e., the SFR measured within the portion of the galaxy sampled by the fiber, without applying the aperture correction. Figure 3.7, analogues to Figure 3.6, shows the results. We can identify two different behaviours of the fiber SFR with disk inclination, depending on the stellar mass.

- Galaxies with $M_\star < 10^{10.25} M_\odot$. The trend reverses with respect to the one in Figure 3.6: the peak of the SF distribution shifts to slightly higher values

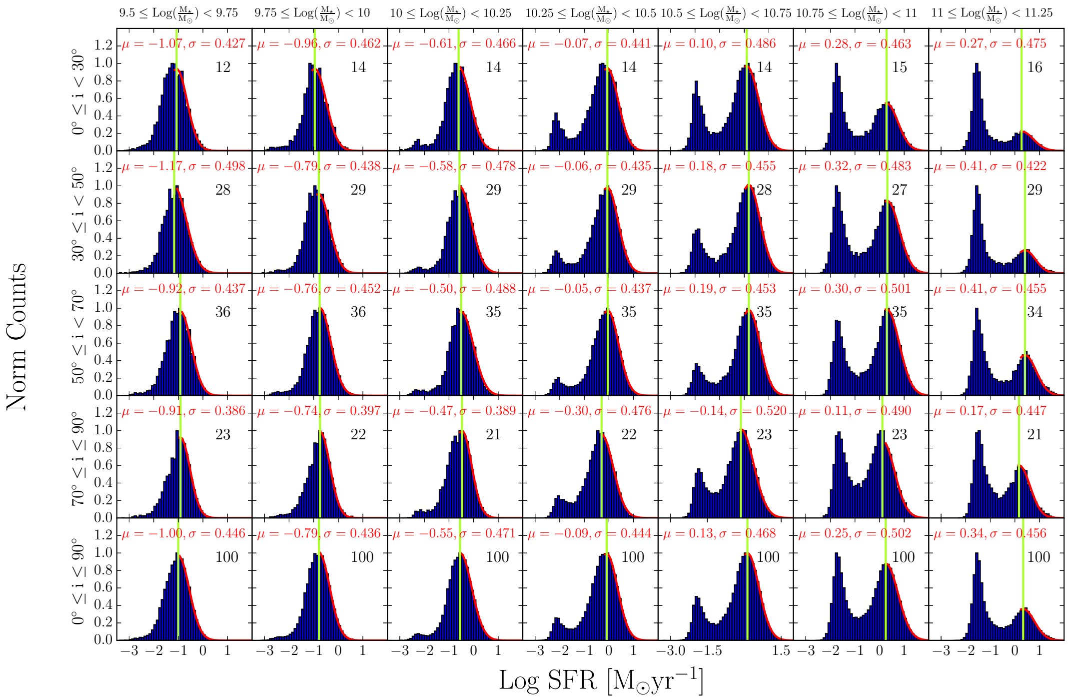

Figure 3.7: Same as in Fig. 3.6, but considering the fiber SFR, not aperture-corrected.

for increasing disk inclination angle, whereas it shifts to slightly lower values in Figure 3.6.

- Galaxies with $M_\star \geq 10^{10.25} M_\odot$. We notice that the fiber SF peaks at lower SFR values for nearly face-on disks ($i < 30°$) than for higher disk inclination angles ($30° < i < 70°$). This is because the bulge component of MS galaxies becomes more prominent for increasing stellar masses (see Figure 3.1), and hence the fiber SFR of a galaxy with a face-on disk is affected by the passive bulge component. This is confirmed by the fact that, for the most massive galaxies with disk inclination angle between 0° and 30°, the passive peak is more predominant in the fiber SFR distribution (Figure 3.7) than in total SFR distribution (Figure 3.6). [2] For increasing disk inclination angles ($i > 70°$), the SF peak shifts to smaller values (~ 0.2 dex), and is more predominant than for lower disk inclination angles. We infer that since a larger portion of the disk enters the fiber, a larger number of galaxies is identified as star-forming, but the dust correction results in an underestimate of the SFR. In fact, morphology alone can not account for this as dust correction shifts the fiber SF peak to lower values (quantitatively less pronounced), even for nearly edge-on pure-disk massive galaxies.

---

[2] On the contrary, for nearly face-on galaxies with lower stellar masses, the shape of the SFR distribution does not change when considering the total SFR instead of the fiber value, because these galaxies are either pure disks or have very low B/T values.

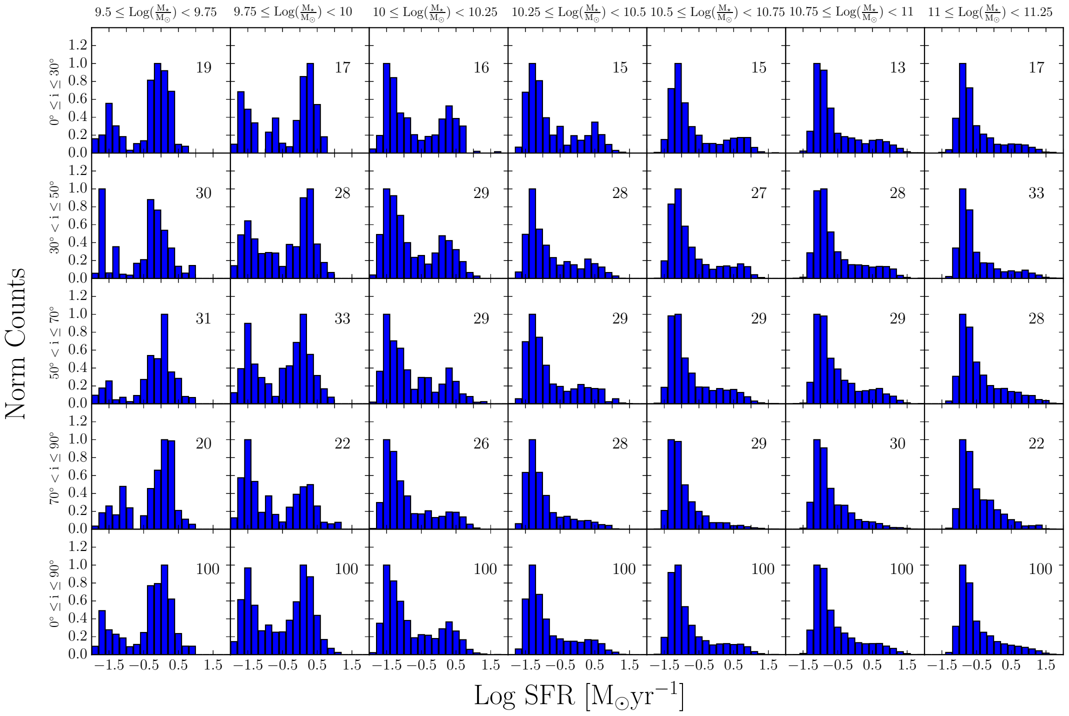

Figure 3.8: Total SFR distributions in bin of stellar mass and disk inclination angle (i_{S11}) analogues to Figure 3.6, but for galaxies with 0.5<B/T<0.9 and P_{PS} <0.32 (to exclude spurious disks from the subsample of bulge-dominated galaxies).

The varying trends in the position of the fiber SFR peak as a function of disk inclination, for galaxies with different stellar masses, can be attributed to their dust content. As shown in Brinchmann et al. (2004), with increasing stellar mass galaxies have a higher dust content, hence the trend of self absorption with disk inclination is more important for more massive galaxies.

For completeness, we repeated the same analysis for the bulge-dominated galaxies, with $0.5 < \mathrm{B/T} < 0.9$. We know that the S11 catalogue is affected by the presence of spurious disks in bulge-dominated galaxies, and that those disks are given, on average, lower inclination angles. For this reason, we restrict the sample for this qualitatively analysis only to galaxies that have a secure disk-component, i.e. $P_{PS} < 0.32$. Figure 3.8 shows the total SFR histograms in mass and axis ratio bins, analogues to Figure 3.6, but now for bulge-dominated galaxies. Not unexpectedly, the quenched peak is dominant in virtually all bins, including the low mass ones, contrary to Figure 3.6 where passive galaxies are almost completely absent in the low-mass bins. We can observe, especially for more massive galaxies, a progressive filling of the green valley region with increasing disk inclination. This progressive filling is due to the shift at lower values of the peak of the SF gaussian, that at high disk inclinations and stellar masses it is not distinguishable anymore from the tail of the passive gaussian.

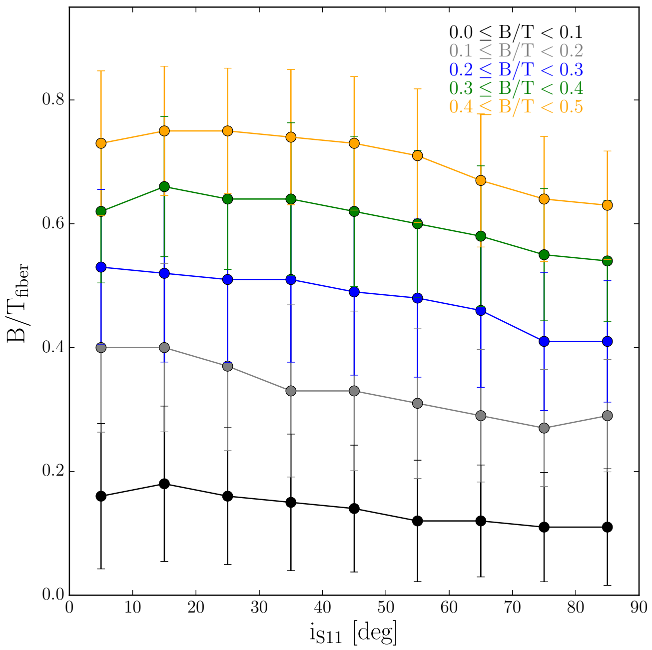

Figure 3.9: Fiber B/T (B/T$_{fiber}$) as a function of the disk inclination angle (i_{S11}) for galaxies with total stellar mass in the range $10.75 \leq \mathrm{Log}(M_\star/M_\odot) < 11.0$. Different colours mark galaxies in certain ranges of B/T, as indicated in the legend of the figure. There is a weak trend of decreasing B/T$_{fiber}$ with increasing disk inclination angle, as expected since the fraction of disk light entering the fiber is an increasing function of the disk inclination.

3.4 Discussion

3.4.1 Interpretation of the inclination effects

Figure 3.6 illustrates the two major inclination effects, which grow more prominent with increasing stellar mass: with increasing disk inclination- (1) the SF peak shifts to lower SFRs, and (2) the strength of the SF peak increases relative to the peak of quenched galaxies. We believe that they reflect two inclination-dependant effects that have a role in determining the total SFR of a galaxy and are dependent on the stellar mass of the galaxy. The first effect is independent of morphology and is related to dust obscuration. For more inclined galaxies as photons have to travel longer distances within the disk itself before reaching the observer, an increasing fraction of the Hα and Hβ fluxes gets absorbed within the plane of the galaxy along the line of sight. As discussed in the previous section, from Fig. 3.7 we can distinguish two different ranges of stellar mass where the trends in the position of the *fiber* SFR peak with increasing disk inclinations are opposite to each other. For low mass galaxies, $\mathrm{M}_\star < 10^{10.25}\mathrm{M}_\odot$, the peak of the SF gaussian gradually shifts to larger values when going from face-on to edge-on disks. This implies that the shift at lower values of the *total* SF peak seen for low mass galaxies in Fig. 3.6 is actually caused by the aperture correction. At larger stellar masses, the aperture correction acts together with the dust content of the galaxy resulting in a shift of $\sim 0.15 - 0.20$ dex towards lower values of the *total* SF peak for a galaxy going from a nearly face-on disk to a nearly edge on disk.

The second effect is dependant on galaxy morphology and it is more evident for more massive galaxies, since MS massive galaxies are characterised by larger B/T values than MS counterparts at lower stellar mass. In particular, as we discussed earlier, we believe that this effect is due to a trend, with disk inclination, of the bulge and disk fractions that are sampled by the fibers. To show this effect, we make use of the fiber B/T ratio, B/T$_{fiber}$, that is given in the S11 catalogue. As for the total B/T, we use here the B/T$_{fiber}$ computed from the $r-$band. In Fig. 3.9, B/T$_{fiber}$ is shown as a function of the disk inclination angle, i_{S11}, for galaxies in different bins of total B/T (in different colours) and stellar mass in the range $10^{10.75}$-$10^{11}M_{\odot}$. As expected, there is a weak trend of decreasing B/T$_{fiber}$ as the disk inclination increases, due to a larger fraction of the disk entering the fiber. This effect is small as the total B/T is fixed and the decrease in B/T$_{fiber}$ with increasing i_{S11} is steeper for galaxies with larger B/T. The slope also varies with stellar mass, and it is steeper for more massive galaxies than for lower mass ones. This is because at fixed B/T the bulge component in more massive galaxies is characterised by a larger radius than the bulge of a lower mass galaxy, hence the variations with disk inclination within the fiber are stronger. In massive, face-on star-forming galaxies the $3''$ fibers sample –in most cases– just the bulge of the galaxies. Since most bulges are quenched most fibers sample just the quenched part of the galaxies. Apparently, in such cases the aperture correction is not sufficient to properly include the full SFR of the disk. However, as the inclination increases, an increasing fraction of the SF disk enters the fiber, the galaxy is recognised as SF and the aperture correction goes some way towards including the SFR of the disk. Still, quite possibly not all of it, as we know that the aperture correction and dust content are responsible, in massive galaxies, of a shift of $\sim 0.15 - 0.20$ dex towards lower values of the *total* SF peak. The shift of ~ 0.4 dex in the position of the SF peak in the most massive edge-on galaxies indicates that the actual SFR is on average underestimated by a factor ~ 2.5 for these galaxies, a quite significant effect.

Overall, this extreme inclination effect is relevant for only a small fraction of galaxies, say $\sim 25 - 30\%$ of the whole sample, and especially confined to the most massive galaxies. Therefore, by and large the bulk of the population is reasonably well accounted for. But minorities count for some interesting issue, as discussed next.

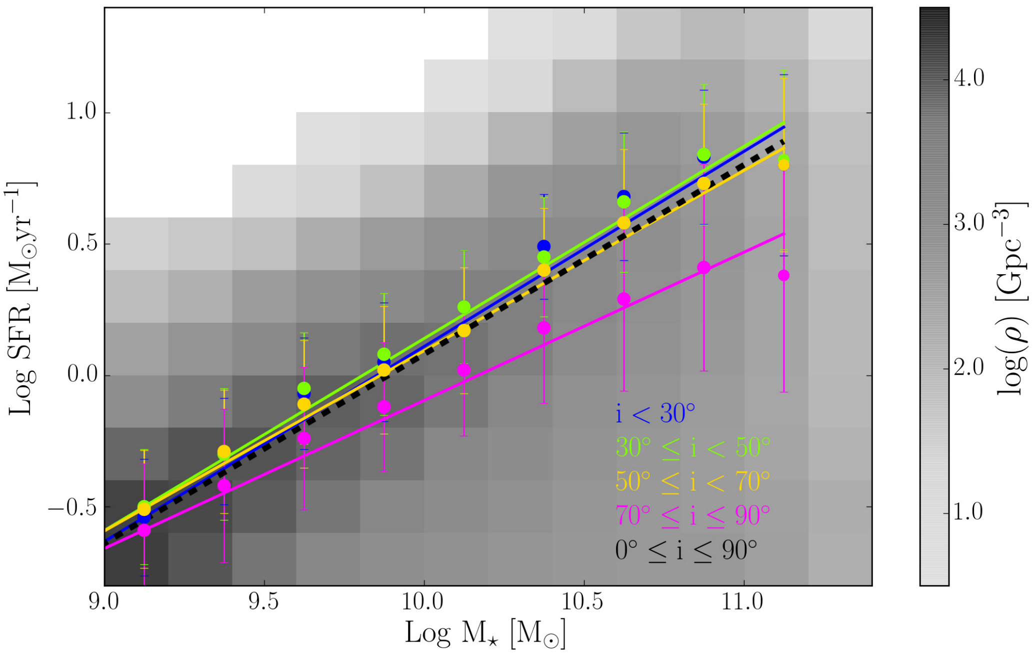

Figure 3.10: The SFR-$M_\star$ plane and the MS relation for galaxies that have different disk inclination angles. Each bin has been color-coded as a function of the number of galaxies divided by the average V_{max} value in the bin. The dotted black line is the MS for all galaxies in our final catalogue, i.e. for galaxies with disk inclination angles $0° \leq i \leq 90°$. The MS relations are obtained from a linear regression of the mean values of the gaussian fit to the high side of the SFR distributions, as shown in Figure 3.5 (red gaussians). The same applies to the dispersion values, shown as vertical bars. The MS fit for the total sample, irrespective of inclination, is shown in black.

3.4.2 Effects on the Main Sequence

Figure 3.10 shows the LogSFR - LogM$_\star$ plane where each bin in LogSFR and LogM$_\star$ has been colour coded as a function of the space density in that bin, computed as the ratio of the number of galaxies and the average V_{max}, and it is indicated by the greyscale. The best fit MS relations, i.e., LogSFR $= m\, Log(M_\star) + c$, computed in different bins of disk inclination angle, are shown in Figure 3.10 with different colours. In each stellar mass bin, the MS value and dispersion are the values written in red in each panel of Figure 3.6, and are the peak and dispersion of the gaussian curve obtained from the fit to the right part of the SF distribution of SFR (gaussians are shown in red in Figure 3.6). The slope and intercept of the MS relation in each disk inclination angle interval are obtained from a linear regression using the MS values in each stellar mass bin, covering the range ($10^{8.5} - 10^{11.25}$ M$_\odot$). The resulting LogSFR - LogM$_\star$ relation for the whole sample of SF galaxies (black dotted line in Figure 3.10) has a slope of $m = 0.72 \pm 0.02$ and an intercept of -7.12. If we limit the stellar mass range to

$10^{8.5}$–$10^{11.0}$ M$_{\odot}$, hence avoiding the most massive bin, for the whole galaxy sample we obtain $m = 0.76 \pm 0.02$, that is the slope found by Renzini & Peng (2015). For the subsample of galaxies characterised by nearly face-on disks ($i < 30°$; in blue in Figure 3.10) we obtain a slope $m = 0.74 \pm 0.02$, with $c = -7.31$. Galaxies with disk inclination angle between $30° \leq i < 50°$ (in green) have a slope of $m = 0.73 \pm 0.02$ and $c = -7.17$, while for disk inclination angle between and $50° \leq i < 70°$ (in yellow) the slope is smaller and the intercept is larger: $m = 0.68 \pm 0.03$, $c = -6.76$. Finally, for nearly edge-on disks, ($i \geq 70°$; in magenta in Figure 3.5) the slope is flatter, $m = 0.56 \pm 0.03$, and the intercept larger, $c = -5.73$. Hence, the MS becomes progressively flatter and the intercept increases when considering galaxies with increasingly inclined disks. In addition to the change of slope and intercept of the MS for different disk inclination angles, another effect that seems clear from Figure 3.10 is that the lower envelope of the MS relation and the green valley region seem to be contaminated by galaxies with highly inclined disks. We analyze this effect in the next section.

3.4.3 Contaminating the Green Valley

The shift to lower SFRs of the SF peak of massive galaxies with increasing inclination has an adverse effect on efforts of identifying really *quenching* galaxies, i.e., galaxies that have left the main sequence, their SFR is dropping, and are destined to join the *graveyard* of quenched galaxies. Even if the total number of high inclination galaxies is relatively small, within the green valley they may even outnumber the truly quenching galaxies.

To quantify the contamination of high-inclined disks in the green valley, we plot, for each stellar mass bin, the fraction of galaxies with disk inclination $i \geq 70°$, $f_{i>70°}$, as a function of the LogSFR distance from the MS, Δ_{MS}. Here, the MS values are the ones obtained for the total population of galaxies, regardless of the disk inclination. Δ_{MS} has been computed in bins that are 0.2 dex wide, and it is negative for galaxies above the MS, positive for galaxies below the MS. Results are shown in Figure 3.11: the left panel shows galaxies with B/T ≤ 0.3, while in the right panel galaxies with $0.3 <$ B/T ≤ 0.5 are shown, to underline trends with morphology. Each stellar mass bin is indicated by a different colour.

There is a strong increase of the fraction of nearly edge-on galaxies, $f_{i>70°}$, when moving from the upper envelope of the MS towards its lower envelop. For disk galaxies with M$_{\star} < 10^{10.75}$M$_{\odot}$, $f_{i>70°}$ computed 0.8 dex below the MS is 4 times larger than $f_{i>70°}$ at 0.6 dex above the MS. For more massive disk galaxies, the peak value of $f_{i>70°}$ is smaller, $\sim 35\%$ for M$_{\star} < 10^{10.75-11.0}M_{\odot}$ and $\sim 27\%$ for M$_{\star} < 10^{11.0-11.25}M_{\odot}$. In fact, the SFR of the most massive galaxies is derived mainly from the D4000 break as soon as we move below the MS. As shown in

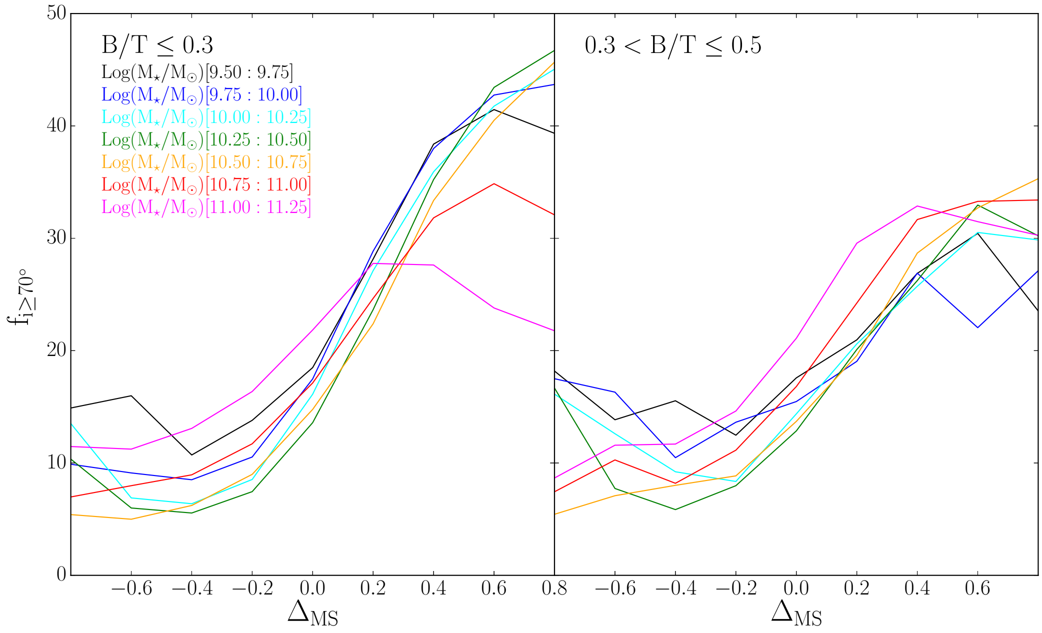

Figure 3.11: Fraction of galaxies with disk inclination angle $i_{S11} \geq 70°$ as a function of the distance from the MS of star forming galaxies. In the *left panel* the subsample of galaxies with B/T≤0.3 is shown, while the *right panel* shows galaxies with 0.3<B/T≤0.5. The distance from the MS is computed in bins of 0.2 dex, and it is negative for galaxies above the MS, positive for galaxies below the MS. Different colours mark different stellar mass bins. There is a strong trend of increasing fraction of nearly edge-on galaxies when moving at fixed stellar mass from 0.8 dex above the MS, towards lower SFR, up to 0.8 dex below the MS. This trend is stronger for the lowest B/T galaxies.

Figure 3.11, for $M_\star > 10^{10.8} M_\odot$, the fraction of galaxies that have SFR from $H\alpha$ is ∼70% on the MS, and quickly drops to ∼ 20% at ∼0.8 dex below the MS. Since the SFR from D4000 is less affected by reddening as it is derived from a break of the continuum, the increase of $f_{i>70°}$ from the upper to the lower envelop of the MS is milder for the most massive galaxies. The increase in $f_{i>70°}$ is less steep for galaxies with 0.3<B/T≤0.5 (right panel in Figure 3.11), where $f_{i>70°}$ computed at 0.8 dex below the MS is a factor from 2 to 3 larger than above MS, and it shows less variation as a function of stellar mass. We believe that the different increase in $f_{i>70°}$ for galaxies with different morphology could be caused by two effects: 1) the disk inclination angle in nearly edge-on disks might be underestimated by S11 for galaxies with $0.4 < B/T \leq 0.5$, that mainly populate the lower envelop of the MS, and 2) the increase in the fraction of SFR from D4000 when moving from the MS towards its lower envelop is stronger for intermediate B/T galaxies than for disk-dominated galaxies.

It is indeed clear that, at any stellar mass, the fraction of galaxies with highly inclined disks increases when moving from the upper MS envelope toward the lower MS envelope and the green valley region. This rises two important points:

1) there is a fraction highly inclined disks *intruders* in the green valley that should be removed if the goal is to identify galaxies in which the quenching is ongoing, and 2) the scatter of the MS seems to be dependent on the disk inclination angle, and hence the relation could be tighter when correcting for the inclination effect.

3.4.4 Conclusions

We have used the spectroscopic catalogue of SDSS DR7 and the bulge-disk decomposition of Simard et al. (2011) to study the effects of disk inclination on the MS of star-forming galaxies and the contamination of highly inclined disks in the green valley region. The main findings of this work can be summarized as follows:

- The peak of the total SFR distribution of star-forming galaxies shifts to lower values with increasing disk inclination angles. Such a shift amounts to ~ 0.2 dex for $\mathrm{Log}(\mathrm{M}_\star/\mathrm{M}_\odot) < 10.25$, and increases to ~ 0.4 dex for more massive galaxies. The dispersion of the best-fit gaussian to the SF peak slightly increases with increasing disk inclination angles, but this is a small effect (at most ~ 0.1 dex in σ).

- When considering the fiber SFR, in less massive galaxies we observe an opposite trend than the one that characterises the total SFR with increasing disk inclination angle. This implies that, for low stellar masses, the shift of 0.2 dex towards lower SFR in the total SF peak is caused by the aperture correction applied in Brinchmann et al. (2004). For more massive galaxies, we observe an average shift of the SF peak of 0.2 dex towards lower SFR values when considering nearly edge-on disks as compared to galaxies with $30^\circ < i < 70^\circ$. For galaxies with nearly face-on disks, the peak of the SFR distribution of star forming galaxies is found at lower values than for galaxies with $30^\circ < i < 70^\circ$. This shift to lower fiber SFR values in massive galaxies with nearly face-on disks is due to the presence of a massive non-star-forming bulge in the the SDSS fiber.

- The relative strength of the SF and passive peaks of the SFR distributions is a function of inclination, particularly at high stellar masses, with the SF peak growing more prominent with increasing inclination. This effect reflects a change in the morphology of MS galaxies, that at high stellar masses are characterised by an increase of the bulge component. For a galaxy at a given stellar mass and B/T, the relative fractions of disk and bulge within the fiber are a function on the disk inclination, with the bulge fraction that decreases for increasing disk inclination angle.

- The shift in the SFR peak with increasing inclination is the result of the combination of the different effects explained above. At low stellar masses, MS galaxies are mostly pure disks, and the shift is attributed to the aperture correction that is applied to compute the total SFR from the fiber SFR. At larger stellar masses the dust content of galaxies increases and the final shift of the SF peak in nearly edge on disks is the result of: 1) extinction correction to the SFR being systematically underestimated in high inclination galaxies, 2) aperture correction, and 3) increase of the B/T ratio in MS galaxies.

- For the subsample of nearly edge-on galaxies, the MS relation is significantly flatter than for the total sample, with a slope of $m = 0.56 \pm 0.02$, with respect to the $m = 0.74 \pm 0.02$ for the whole sample. Also the intercept significantly differs, going from -7.31 (whole sample) to -5.37 (nearly edge-on).
- The fraction of galaxies with disk inclination angle $i \geq 70°$ is a strong function of the position in the LogSFR - LogM$_\star$ plane with respect to the MS. In fact, the fraction of disk dominated galaxies with $i \geq 70°$ increases by a factor of ~ 4 at all stellar masses when moving from 0.8 dex above the MS to 0.8 below it. When considering more bulge dominated galaxies ($0.3 < \mathrm{B/T} \leq 0.5$), the effect is still important, but the fraction of galaxies with highly inclined disks changes by a factor of ~ 3 from the upper to the lower envelope of the MS.

Galaxies characterised by highly inclined disks are likely to be strongly obscured, hence their SFR estimates are more uncertain. Masters et al. (2010) and Sodré Jr et al. (2013) conclude that significant amounts of dust are present in inclined spirals, and that edge-on disks are the reddest objects in the local Universe. Knowing that, many recent works which focus on the study of quenching mechanism of galaxies based on a colour selection of the galaxy samples tend to remove inclined disks to avoid their obscuration problem (Tojeiro et al., 2013; Willett et al., 2015). Schawinski et al. (2014) show that the effect of inclination is small, and that the green valley is not appreciably depopulated after correcting for dust extinction. Still, Schawinski et al. (2014) did not consider green valley galaxies with intermediate morphology, which are the relative majority in the morphological classification of Galaxy Zoo. In principle, the green valley region can provide information on the nature and duration of the process that causes the transition of a galaxy from the blue cloud to the red sequence or, in other terms, from the MS to the passive region of the LogSFR - LogM$_\star$ plane. For this reason, a careful estimate of the galaxy population of the green valley cannot proceed without taking the disk inclination into account, as we have shown that a large fraction of highly inclined disks tend to fill the green valley and lie in the lower envelope of the MS relation.

4 Spatial distribution of stellar mass and star formation activity at higher redshift

This chapter collects the work I have been doing in the past year and not yet published, based on the collaboration with Professor Pascal Oesch and with Paola Popesso, Erica Nelson, Anna Cibinel and Mireia Montes.

4.1 Introduction

In Chapter 2 the contribution of the star formation activity to the total star formation rate of a galaxy was investigated in depth for a sample of local SDSS galaxies at $z < 0.1$. The aim was to understand what drives galaxies above or below the Main Sequence. As a natural next step, we carry out a similar analysis for galaxies up to redshift z $\sim$ 1, to motivate a coherent picture of the change in the star formation activity of galaxies during the last 8 billion years of our Universe's evolution.

From the theoretical point of view, Tacchella et al. (2015b) propose that episodes of compaction and gravitational instabilities could drive gas towards the centre of galaxies. This would lead to the creation of a blue, star forming, central component. Following that, AGN feedback and gas consumption would then quench the central star formation episode, leaving a quenched, red bulge. A sequence of compaction-quenching episodes could move galaxies above and below the MS and along it and explain the observed scatter. Thus it became clear that in order to understand the evolution of the star formation activity and thereby the migration of galaxies across the MS, it is mandatory to obtain observational data that can spatially resolve galactic structure (Allen et al., 2006; Abramson et al., 2014; Morselli et al., 2017). At low redshift, Spindler et al. (2017) found that galaxies classified as AGN/LI(N)ER typically have centrally-suppressed sSFR profiles, possibly indicating a relation between central quenching and AGN activity. They also found that suppression of sSFR, both central and at outer radii, happens in galaxies that are more bulge-dominated than typical star forming ones, further suggesting that morphological quenching might be a key contributor to the overall quenching mechanism. Lin et al. (2017) concluded that SF has to be first suppressed in the bulge due to depletion of cold gas, and subsequently in to disk (an $inside - out$ mechanism). In addition, they argue that AGN feedback is responsible for the lack of cold gas in the central regions of galaxies. Using MaNGA data, Belfiore et al. (2017) argue that a slow quenching process must result in the suppression of the star formation activity at all radii, and not only in the central regions, as they find that green valley galaxies have typically non star forming bulges and lower star formation in the disk. Contrary to what has been said thus far, based on their analysis of the Manga data Goddard et al. (2017) found that early type galaxies are characterised by slightly positive age gradients, hence favouring a outside-in evolution of star formation in galaxies. At larger redshifts, Nelson et al. (2016) use H_α stacked profiles and find that H_α above (below) the MS is enhanced (suppressed) at all radii, suggesting a scenario where the physical processes driving the change in star formation activity are independent of the host galaxy mass and act throughout the galactic disk in a coherent manner. $Inside - out$ quenching was instead used by Morishita & Ichikawa (2016), Tacchella et al. (2015a), Tacchella et al. (2016), and Tacchella et al. (2017) to explain trends of sSFR, colours, and dust, observed in real and simulated galaxies in the redshift range 1-7. The exact nature of quenching is yet not understood, and this work is partly aimed at elucidating the issue.

In this study, we exploit the combination of 3DHST (a near-infrared spectroscopic survey with the Hubble Space Telescope) photometric data with the deepest UV observation to date (see Sec. 4.2) collected in the central part of the GOODS fields with the UVIS camera onboard HST as part of the HDUV survey (Oesch et al., submitted), to understand how the spatial distribution of mass and star formation activity changes as a function of the integrate $M_\star$ and SFR.

4.2 Data

This work was carried out using galaxies located in the the central parts of the GOODS fields (Giavalisco et al., 2004), that overlaps with the Hubble Deep UV survey (HDUV, PI: P. Oesch), representing the deepest and high resolution UV data to date. The HDUV is a legacy imaging program carried out with the WFC3/UVIS camera onboard HST that with a total of 132 orbits allows to get very deep images (27.5-28 mag) with the F275W and F336W filters, over a wide area of ∼100 arcmin^2 and with high spatial resolution (<0.1”). More details on the survey strategy can be obtained from Oesch et al. (submitted), while the survey coverage of the GOODS fields is shown in Fig. 4.1. Also available in the central parts of the GOODS fields are: 1) the photometric and spectroscopic

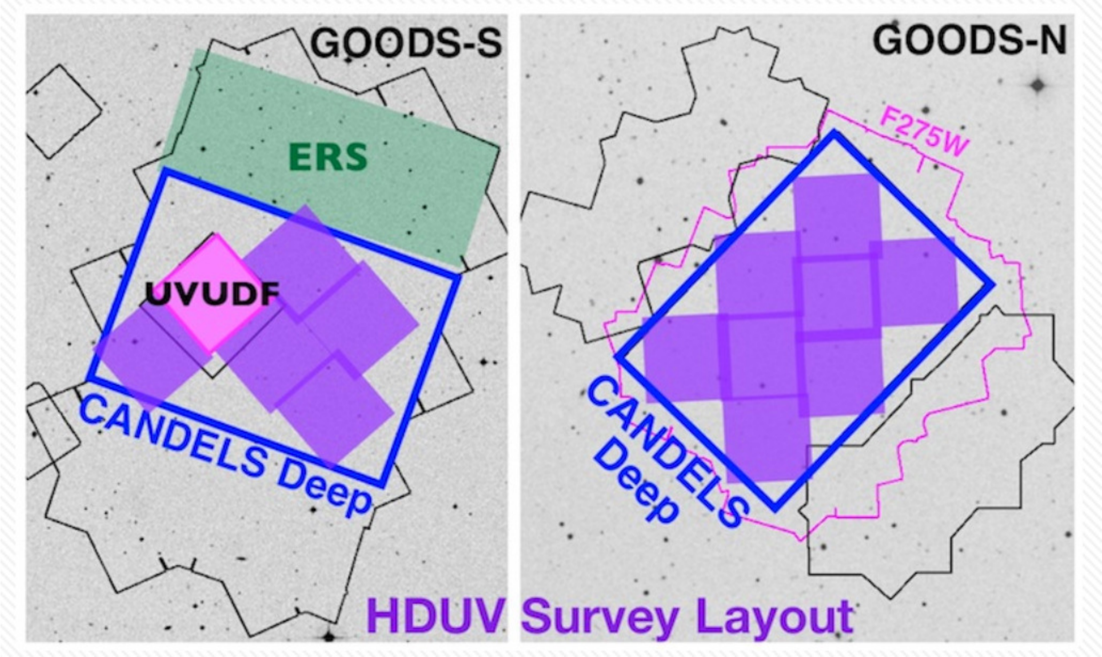

Figure 4.1: The HDUV survey covers most of the CANDELS-DEEP region. The GOODS-South region (left panel) is be covered by 5 pointings, while the GOODS-North region (right panel) with 8 pointings. [From Oesch et al. (submitted)]

observations taken as part of the 3DHST survey with HST/WFC3 and ACS; 2) the deepest far-IR data to date, obtained combining observations of the GOODS fields taken with PACS (Photodetector Array Camera and Spectrometer) as part of the PACS Evolutionary Probe survey (PEP) with the GOODS-Herschel key programmes (Lutz et al., 2011; Elbaz et al., 2011; Magnelli et al., 2013). The IR data allow an accurate determination of IR luminosity (L_{IR}), and as a result the obscured SFR of dusty high redshift star forming galaxies. Together with the other available imaging data in the central parts of the GOODS fields, it is thus possible to construct SEDs over a large wavelength range.

4.2.1 Redshifts, Stellar Masses, SFRs and structural parameters

Redshift and stellar masses come from the public releases of 3D-HST data products, in particular from the catalogue of W14. In W14, the best available redshift is used for the computation of the stellar masses, rank ordered spectroscopic, grism or photometric (Momcheva & Team, 2016). Stellar masses are obtained from fitting the 0.3-8μm SED range with the FAST code (Kriek et al., 2009) using the Bruzual & Charlot (2003) stellar population synthesis models, a Chabrier (2003) IMF, solar metallicities, a Calzetti et al. (2000) dust attenuation law and a exponentially declining star formation history (the same procedure followed by Skelton et al. 2014, with the difference that only photometric redshifts were used). SFRs are considered as the sum of the UV unobscured and the IR obscured contributions. For sources that are in the GOODS-H catalogue of M13, the SFR_{IR} is computed through the Kennicutt relation (Robert C Kennicutt, 1998) from L_{IR}. The total L_{IR}, covering the range 8-1000μm, was estimated by fitting the flux densities at 70, 100 and 160 μm when available with the SED templates of Elbaz et al. (2011). For details on the procedure, see Ziparo et al. (2013). For sources that are not in the GOODS-H catalogue (mainly galaxies with low SFRs, located in the lower envelop of the MS, and passive galaxies) SFR_{IR} comes from W14. Briefly, W14 derived a photometric catalogue of Spitzer/MIPS 24μm sources from the images and weight maps using the approach described in Skelton et al. (2014). The 24μm flux density is then used to estimate L_{IR} through a luminosity-independent conversion, that was demonstrated to recover L_{IR} in good median agreement with Herschel-PACS estimates (Wuyts et al., 2011a). The UV contribution to the SFRs is also taken from W14, and it was estimated from the 2800A luminosity, following the work of Bell et al. (2005). We underline here that for all the sources with L_{IR} the SFR is given by $\mathrm{SFR} = \mathrm{SFR}_{IR} + \mathrm{SFR}_{UV}$. For galaxies with $1 < \mathrm{S/N} < 3$ at 24μm, W14 provides an upper limit of L_{IR}, and thus of SFR_{IR}. For sources undetected in 24μm the SFR is purely based on the UV contribution, and thus it is a lower limit.

4.2.2 Final Sample

For this work we focus on a mass and redshift limited sample with $\mathrm{LogM}_\star > 9.5$ $\mathrm{M}_\odot$ and $0.2 < z < 1.2$. In the area common between HDUV and GOODS-H (~100 arcmin^2) 820 galaxies in Whitaker et al. (2014, W14 hereafter) satisfy the afore mentioned criteria in $\mathrm{M}_\star$ and z. In this range of redshift and stellar masses, 95% completeness is confidently reached, as shown in W14, Muzzin et al. (2013) and Tal et al. (2013). For this subsample, 65% of redshifts are spectroscopic, and the remaining are grism ones. As the aim of this work is to spatially map the SFR in galaxies, AGN contribution to the UV emission represents a source of contamination. For this reason, we removed X ray selected AGN by cross matching our sample with the X-ray selected AGN catalogue of (Shao et al., 2010, for GOODS-N) and (Brusa et al., 2010, for GOODS-S). This results in the omission of $\sim$ 5% of the sources. We then cross-correlated the W14 subsample of our interest with the M13 catalogue to get L_{IR} from Herschel/PACS where possible, and found 55% of galaxies with counterparts in M13. Finally, 30% of the remaining sources have $\mathrm{S/N} < 1$ at 24μm and hence have SFR estimated only from the UV, while for the rest both IR and UV contribution are considered.

4.2.3 Main Sequence definition

The aim of this work is to characterise the scatter around the MS as a function of the spatial distribution of the star formation activity within galaxies. Thus, we need to locate the MS at each redshift and define the position of each galaxy with respect to it. We use the MS of Karim et al. (2011, K11 hereafter), where SFR was computed from 1.4GHz emission, considering a Chabrier (2003) IMF, Bruzual & Charlot (2003) models, and Calzetti et al. (2000) extinction curve. The K11 MS was chosen as it covers the redshift range $0.2 < z < 1.2$ in small redshift steps of 0.2 and has been computed using a relatively wide range in stellar masses (∼2dex) that also includes low mass galaxies. While the former point is key in getting the right normalisation of the MS at each redshift, the latter is important to avoid possible biases due to the flattening of the MS. The MS flattening, still highly debated in literature (e.g. Erfanianfar 2016, Whitaker 2014), if present would induce a bias in a selection of galaxies based on a MS computed only with massive sources.

Using the K11 definition of the MS at each redshift bin, we compute the distance of each galaxy from the relation at the galaxy's redshift. Fig. 4.2 shows the distribution of galaxies in the final sample on the Δ_{MS} - LogM$_\star$ plane, where Δ_{MS} = LogSFR$_{gal}$ - LogSFR$_{MS}$. The colours indicate different SFRs used to compute Δ_{MS}, as explained in the previous section. Herschel detected galaxies (blue) mainly populate the upper envelop of the MS. MIPS-only detected galaxies (grey) mainly populate the lower envelop of the MS, especially at low masses. MIPS upper limits with $1 < S/N < 3$ (orange) populate the valley and quiescent region ∼ 1 dex below the MS. Galaxies undetected in MIPS (maroon), that only have the UV contribution to the SFR, are mainly found at distances larger that 1 dex below the MS.

We define six subsamples of galaxies based on their distance from the MS, chosen to have enough statistics and, at the same time, to take into account the average scatter of the MS (∼0.2 - 0.3 dex). All galaxies with $\Delta_{MS} > 0.6$ constitute the starburst (SB) sample, indicated with the blue shaded region. Galaxies in the upper envelop of the MS, with $0.2 < \Delta_{MS} < 0.6$, make up the SUB1 sample (light blue area in Fig. 4.2). The MS sample is comprised of galaxies that have $-0.2 < \Delta_{MS} < 0.2$ (gray area in Fig. 4.2). The lower envelop on the MS is divided in the SUB1 and SUB 2 samples, that include galaxies with $-0.6 < \Delta_{MS} < -0.2$ (light pink area in Fig. 4.2), and $-1.0 < \Delta_{MS} < -0.6$ (orange area in Fig. 4.2), respectively. Finally, all galaxies with $\Delta_{MS} < -1.0$ form the quiescent (QUIE) sample marked by the shaded red colour. We note that due to the small area covered by the HDUV survey, the number of real starbursts (usually defined in literature as galaxies with $\Delta_{MS} > 1.0$) is limited. Tab. 4.1 shows the number of galaxies in each bin of mass, redshift, and distance from the MS.

Table 4.1: Number of galaxies in each bin of distance from the MS, stellar mass, and redshift.

Sample	$\mathrm{Log}(M_\star/M_\odot)$ 9.5:10.0		$\mathrm{Log}(M_\star/M_\odot)$ 10.0:10.5		$\mathrm{Log}(M_\star/M_\odot)$ 10.5:11.0	
	high z	*low-z*	high z	*low-z*	high z	*low-z*
QUIE	21	9	29	21	34	12
SUB2	16	6	19	8	25	8
SUB1	56	16	11	5	13	4
MS	106	29	34	14	19	7
SUP1	55	44	46	23	12	6
SB	8	12	10	8	1	2

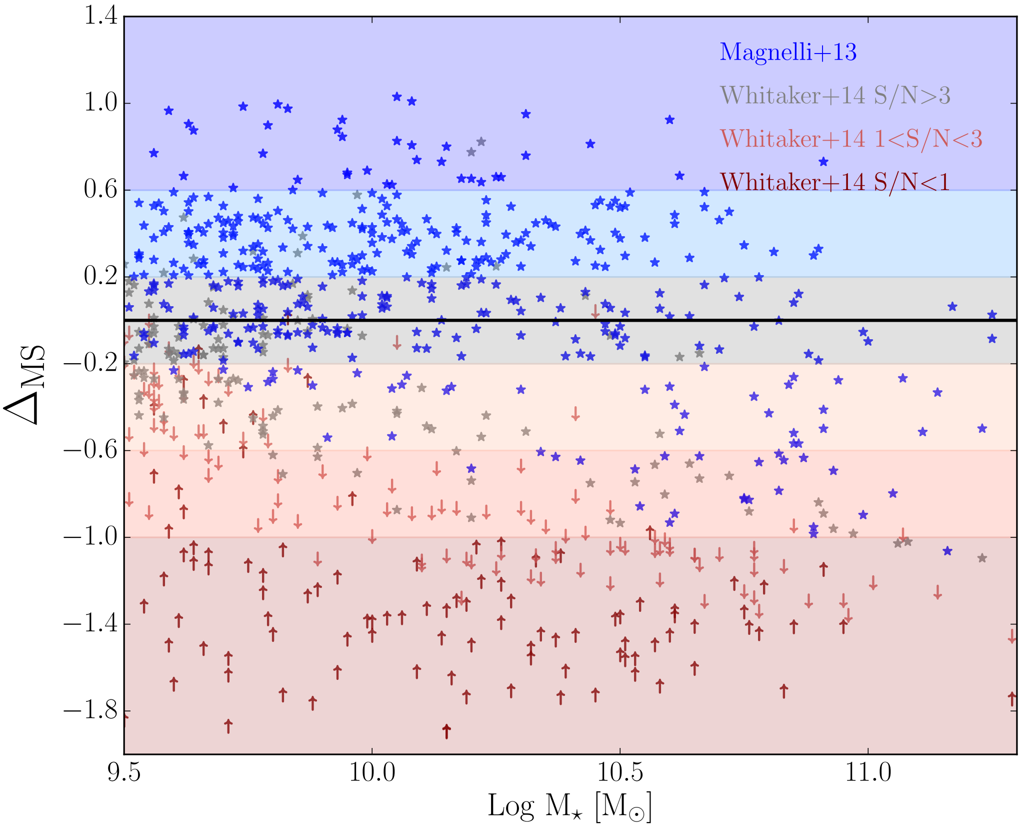

Figure 4.2: Distribution of galaxies in the Δ_{MS} - $\mathrm{Log}M_\star$ plane. The shaded regions mark the bins defined accordingly to the distance from the MS, and will be used from now on in this work.

4.2.4 Maps creation

In recent years, several studies exploited resolved maps of galaxy properties (mass, SFR, age) to study galaxies and their evolution (e.g. Welikala et al., 2008; Zibetti, 2009; Wijesinghe et al., 2010; Guo et al., 2012; Lang et al., 2014). A similar

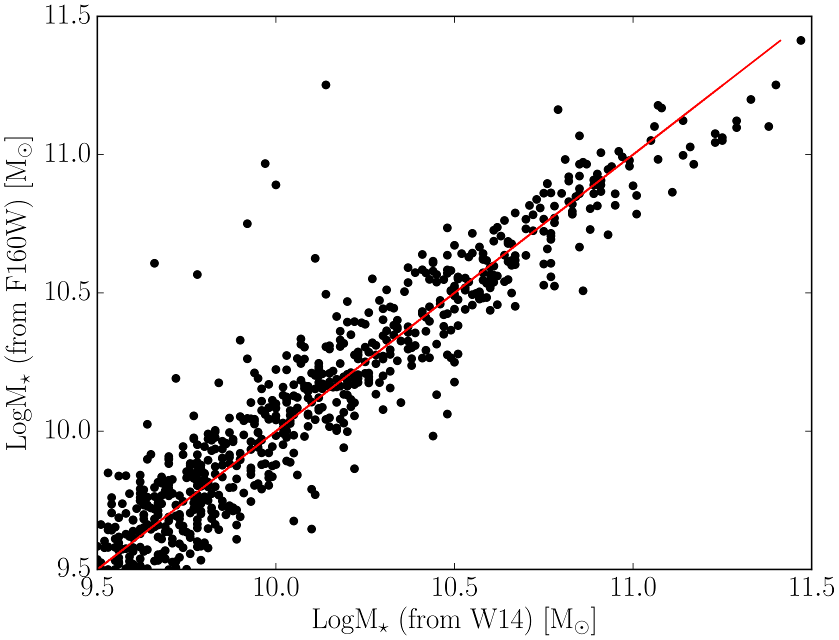

Figure 4.3: Comparison between the stellar mass obtained from SED fitting in the work of W14, and the stellar mass computed as sum of the value in each pixel of the stellar mass maps created for this work, also from SED fitting. The red line is the 1-to-1 relation.

approach has been employed in this work, and we will now describe our map creation process (further details can be found in Cibinel et al., 2015). As a first step, we extracted pixel-by-pixel fluxes within an elliptical aperture equal to the galaxy *H*-band semi-major axis and fitted them with stellar population models. To overcome the problem of relatively low flux in individual pixels, we applied the ADAPTSMOOTH code of Zibetti (2009) to the galaxy images in all the available filters. When, for a given pixel, the S/N is lower than a given threshold, the code replaces that value with an average of the values over a lager circular area. As explained in Cibinel et al. (2015), an advantage of using ADAPTSMOOTH is the facility to smooth images in different filters on the same scale length, a step necessary to obtain self-consistent SEDs. We ran the code on stacked images of all ACS and WCF3 stamps (to ensure that smoothing is applied on those pixels where the majority of the bands reach a low S/N while preserving the structural variations in the different filters) by requiring a minimum S/N = 5 and stopped the algorithm when the averaging area reached the maximum radius of 5 pixels. The smoothing pattern obtained as output was then then applied to all available bands (we tested that our results are not affected by a different choice of the smoothing kernel).

The pixel-by-pixel SED maps that were obtained were then fitted with Lephare (Arnouts et al., 1999; Ilbert et al., 2006) using the Bruzual & Charlot (2003) synthetic spectral library with a Chabrier (2003) IMF and a delayed exponential

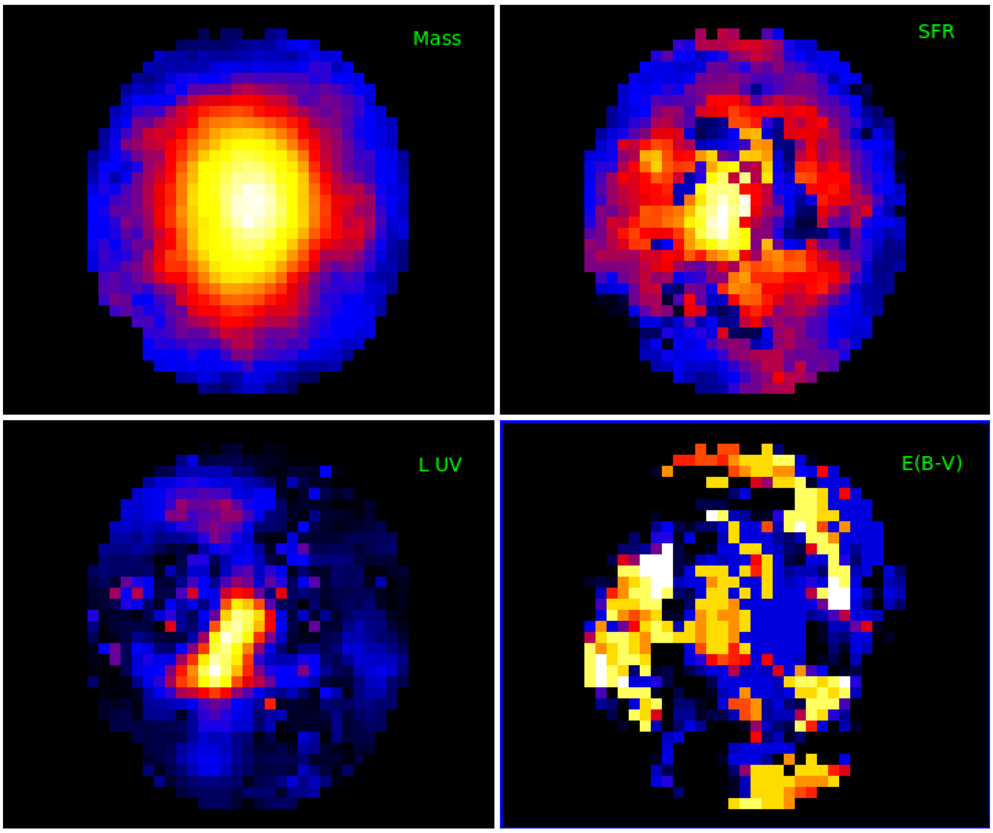

Figure 4.4: Example of a stellar mass (upper left), SFR (upper right), UV luminosity, not corrected for dust (bottom left), and E(B-V) maps (bottom right) for a galaxy in GOODS-N.

star formation history ($\psi \propto (t/\tau^2)\exp(-t/\tau)$). For the SED fitting we applied the following constrains: the typical timescale τ was chosen to vary between 0.01 and 10 Gyr in 22 steps and template ages were selected between 100 Myr and the age of the Universe at the given redshift. We applied a Calzetti et al. (2000) extinction law, with E(B-V) varying between 0 and 0.9 mag and allowing for three values of metallicity Z ($Z = Z_\odot$, $Z = 0.2\ Z_\odot$, $Z = 0.4\ Z_\odot$). As result of the fitting procedure, we obtain median maps (of stellar mass, SFR, age, UV luminosity and extinction), where the value of each pixel is given by the median of the full probability distribution function from all templates, and a best-fit map (i.e., minimum χ^2). In the following analysis, we make use of the median maps, but results do not change when using the best-fit maps instead.

The SED-fitting procedure allows us to obtain the median maps of SFR, E(B-V) and mass-to-light ratio (M/L). We use the M/L maps to obtain the stellar mass maps, by multiplying the H-band flux in each pixel of the H-band images with the best-fit M/L value. This is done to include the sky-noise contribution in the mass maps, needed to obtain a better fit of the 2D mass using GALFIT (see

Sec. 4.2.5). To check the trustability of this procedure, in Fig. 4.3 we show a comparison between the total stellar mass computed as sum of the values in each pixel of the mass map obtained from the H-band image, and the stellar mass in the W14 catalogue. The two estimates are in good agreement, with a scatter of ~0.15 dex.

Finally, the UV luminosity maps are constructed from interpolation to the observed photometry, and they can be non-dust corrected, or corrected for dust using the UV beta slope - A_{UV} relation (Meurer et al., 1999; Overzier et al., 2011), where the UV beta slope is obtained from a linear fit to the best-fit SED model. Fig. 4.4 shows the stellar mass, SFR, UV luminosity and E(B-V) maps for a galaxy in GOODS-S.

4.2.5 Structural parameters from GALFIT

We use GALFIT (Peng, 2010) to fit the 2D stellar mass maps of each galaxy in the sample and obtain its structural parameters. Structural properties of galaxies in GOODS-S and GOODS-N have already been studied as part of the work of van der Wel et al. (2012, vdW12 hereafter). The authors used GALFIT to derived structural parameters by fitting the cutouts of each galaxy in different filters (H160W, J125W and, when available, Y105W) with a single Sérsic profile. 55% of the galaxies in our sample have unreliable fits results in vdW12. Thus, we recompute the structural parameters of the galaxies in our sample as our stellar mass maps are computed with SED fitting on a larger number of filters. In our fitting procedure, the total stellar mass is constrained to vary by ±0.5 dex with respect to the mass obtained as sum of the values in each pixel of the stellar mass maps. The stellar mass maps are fitted using a single Sérsic model. Our fits are reliable for the $\sim$ 98% of the sample, while only $\sim$ 2% of fits retrieve unreliable estimates of the parameters. Fig. 4.5 shows a comparison of the structural parameters obtained from GALFIT in this work and in vdW12. The panels show: the position angle (PA, top-left panel), the axis ratio (q, top-right panel), the effective radii (r_{eff}, bottom-left panel) and the Sérsic index (n, bottom-right panel), respectively. Galaxies that have reliable fits in vdW12 are marked in black, while the green symbols refer to the ones with reliable fits in this work (but not in vdW12). Finally, galaxies with suspicious fits in both works are shown in magenta (as the final parameters are not within the input ranges), while the blue line is the 1-to-1 relation. We notice that, as expected, there is good agreement between the two studies, even when broader constrains are given for each parameter. Galaxies for which the GALFIT fit is unreliable in both works constitute a very small fraction (less than 1%); in vdW12 they have $n = 8$ and large axis ratios, while in this work are found to have very small axes ratios and a broader distribution of n.

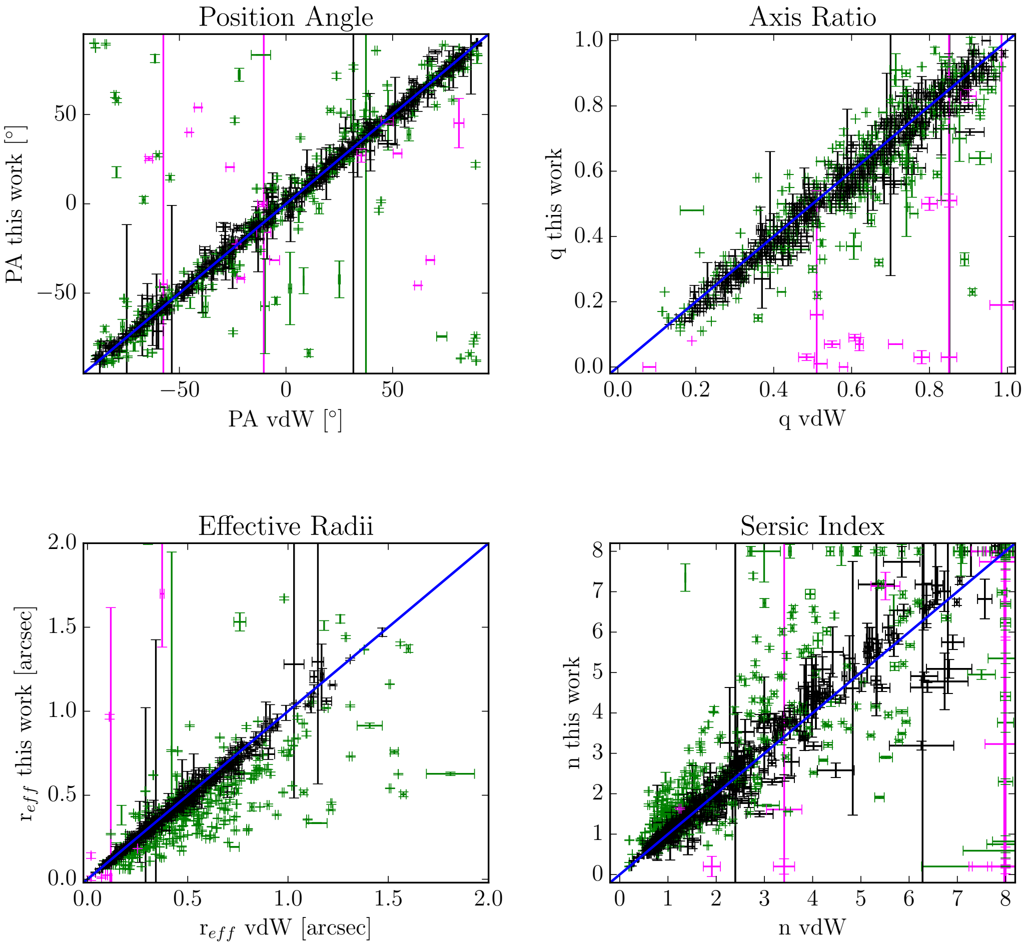

Figure 4.5: Comparison between the structural parameters obtained from a single Sérsic component GALFIT 2D fitting technique in this work and in the one of van der Wel et al. (2012). From left to right: position angle, axis ratio, effective radii in arcsec, and Sérsic index. In all four panels, the black symbols indicate galaxies that in vdW12 have reliable fits, while green ones mark galaxies with trustable fits in this work, but not in vdW12. Finally, galaxies that in both works have unreliable structural parameters from GALFIT are indicated in magenta. The blue line is the 1-to-1 relation.

4.2.6 Radial profiles creation

The 1D azimuthally averaged profiles of stellar mass, SFR, sSFR and UV luminosity of each galaxy are created from the 2D maps using the structural parameters obtained with GALFIT. First, a gaussian kernel is applied to the mass map to find the position of the peak, that we take as centre of the galaxy. Then, concentric ellipses are drawn on the 2D map of the analysed quantity (e.g. SFR or sSFR), where the major axis inclination depends on the galaxy position angle, together with the axis ratio used to define the ellipses. We build two types of radial profile: 1) the one normalised for the effective radii of each galaxy, where r_e comes from the GALFIT fitting procedures; and 2) the physical one, where the radius is given in kpc. While the first method allows us to take care of the intrinsic distribution of r_e with redshift (as galaxies at larger redshifts are more compact), it suffers from the large uncertainties in the estimate of r_e. On the other hand the second approach applied on a large redshift range, inevitably suffers from physical variation in the size of galaxies at different redshifts. Thus, in the analysis, we split the sample in two redshift bins: [0.2:0.7] (*low-z* sample) and [0.7:1.2] (*high-z* sample).

The median profile for a given mass and redshift bin is just the arithmetic median of all the profiles at a certain distance from the centre, while the error is computed via bootstrapping. We truncate the median profile at the radius that contains 50% of the galaxies of the given subsample. In the specific case of the mass profiles, each profile has been normalised to the total mass obtained by integrating the profile before computing the median, to take into account small variations of the median stellar mass in a given mass bin, and hence avoid biases in the analysis. The observed trends do not vary when considering the average profiles instead of the median ones. To check the consistency of the profile procedure, we compare the mass obtained as sum of the values in each pixels of the map, and the total mass obtained from the integration of the radial profiles. The two are in very good agreement.

4.3 Results

4.3.1 SFR, $M_\star$, and sSFR profiles

In Fig. 4.6, we show the median SFR (first raw), $M_\star$ (second raw), and sSFR (third raw) profiles in the different bins of distance from the MS and stellar mass for the *low-z* subsample. The profiles are computed as a function of the physical distance from the center in kpc. The three columns of Fig. 4.6 represent three stellar mass bins: $9.5 < \mathrm{Log}(M_\star/M_\odot) < 10.0$, $10.0 < \mathrm{Log}(M_\star/M_\odot) < 10.5$, and

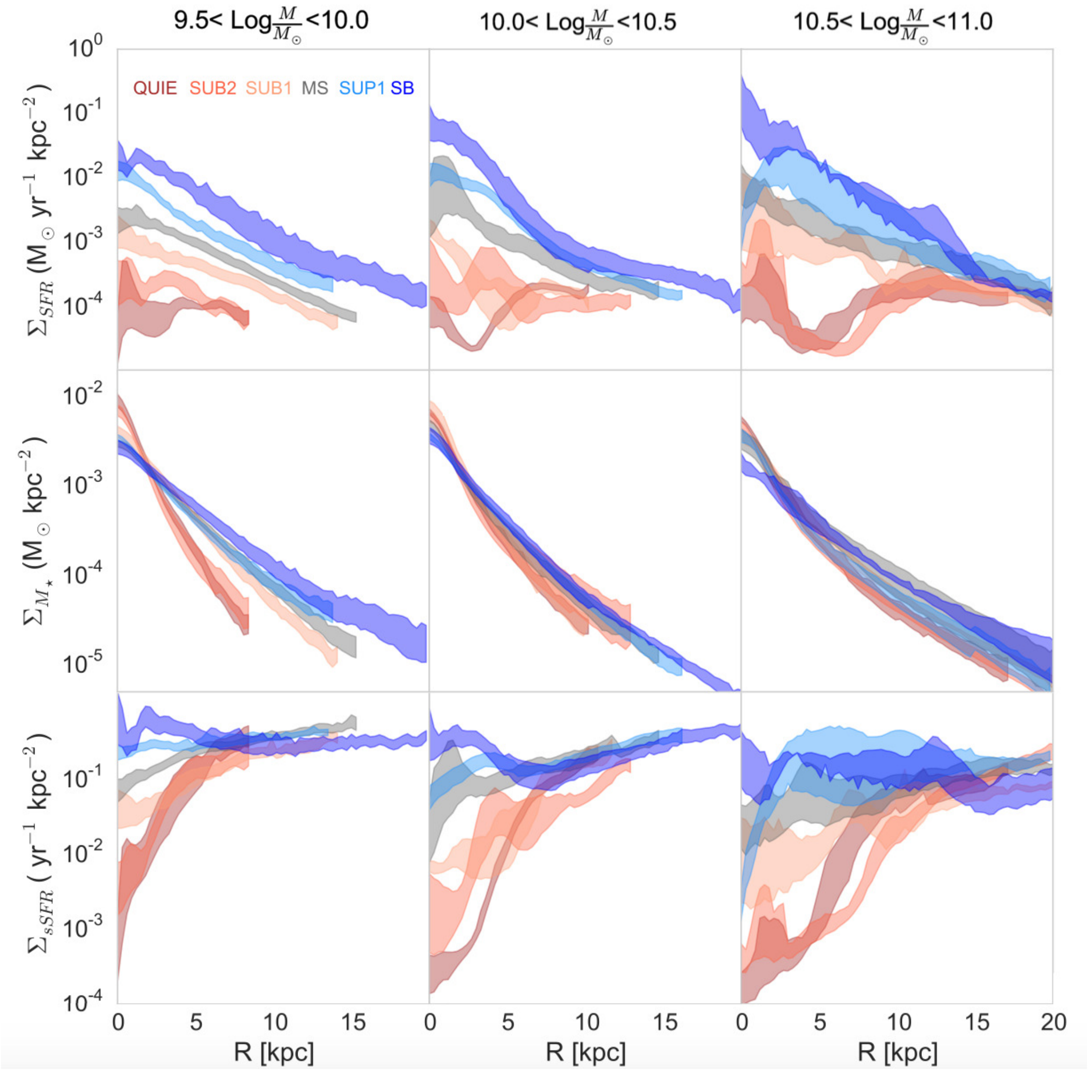

Figure 4.6: median SFR (first raw), stellar mass (second raw), and sSFR (third raw) surface densities as a function of distance from the centre (in kpc) for galaxies in the redshift range [0.2:0.7]. The three columns indicate galaxies with different stellar masses: $9.5<\text{Log}(M_\star/M_\odot)<10.0$ in the first, $10.0<\text{Log}(M_\star/M_\odot)<10.5$ in the second, and $10.5<\text{Log}(M_\star/M_\odot)<11.0$ in the third column, respectively. Different colours mark different bins of distance from the MS, as defined in Fig. 4.2. In the second raw, the average Sérsic indexes of galaxies in the 6 bins are written at the top of the panel, with colours corresponding to the bins.

$10.5 < \text{Log}(M_\star/M_\odot) < 11.0$, respectively. In all panels, the colours correspond to galaxies at different distances from the MS: from passive (red) to MS galaxies (grey) and upper MS galaxies (blue), as defined in Fig. 4.2. For galaxies with $9.5 < \text{Log}(M_\star/M_\odot) < 10$,the SFR profile of QUIE and SUB2 galaxies is almost flat at every radii, while the SFR profiles of SUB1, MS, SUP1, and SB galaxies increases towards the inner radii. For larger stellar masses, the increase of SFR in

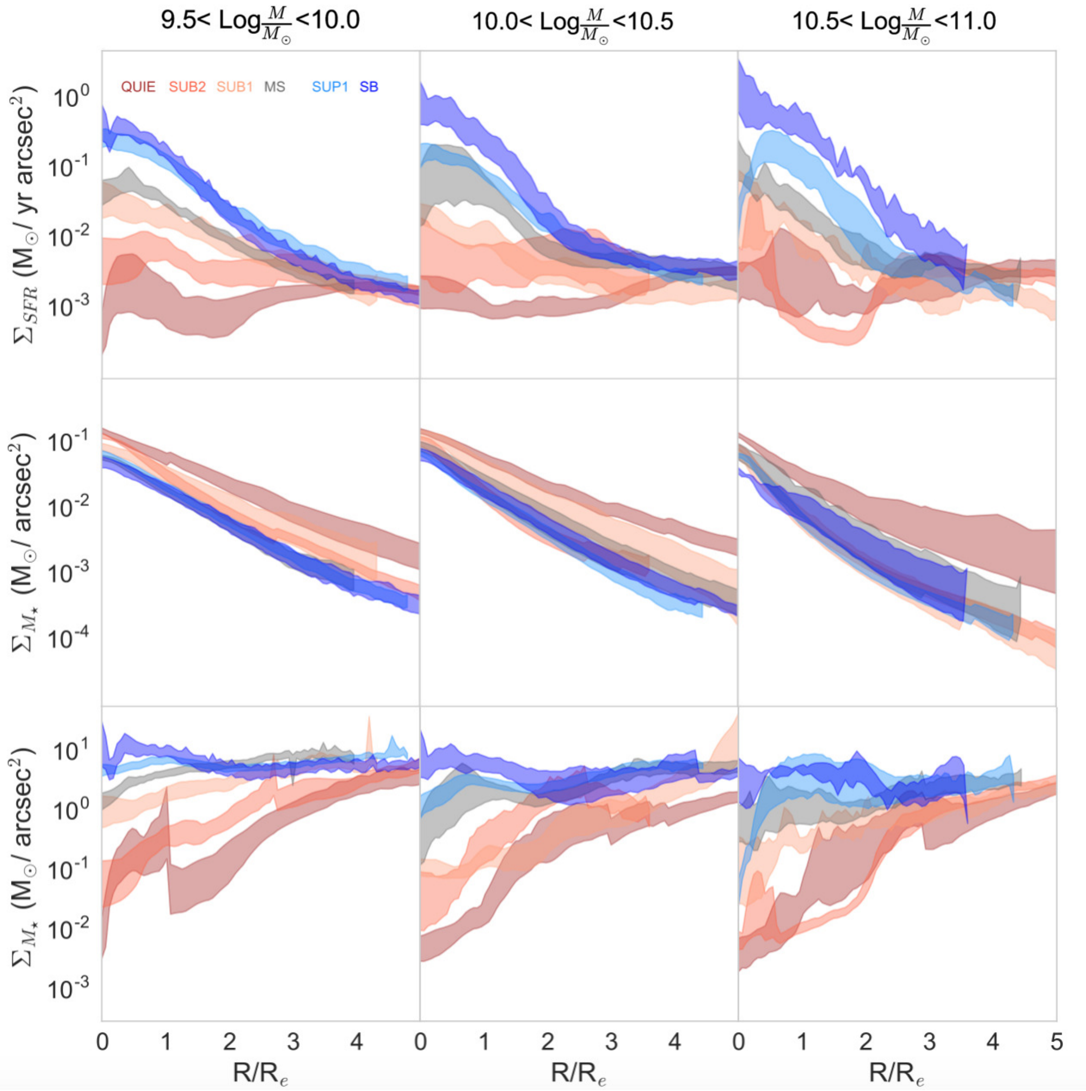

Figure 4.7: median SFR (first raw), stellar mass (second raw), and sSFR (third raw) surface densities as a function of distance from the centre (in R/R$_e$) for galaxies in the redshift range [0.2:0.7]. The three columns indicate galaxies with different stellar masses: 9.5<Log(M$_\star$/M$_\odot$)<10.0 in the first, 10.0<Log(M$_\star$/M$_\odot$)<10.5 in the second, and 10.5<Log(M$_\star$/M$_\odot$)<11.0 in the third column, respectively. Different colours mark different bins of distance from the MS, as defined in Fig. 4.2. In the second raw, the average Sérsic indexes of galaxies in the 6 bins are written at the top of the panel, with colours corresponding to the bins.

the central part is more enhanced for galaxies at higher SFR, with SB showing the largest SFR surface density in the inner ~ 5 kpc. At $R < 5$ kpc, the difference between the SFR profiles of QUIE and SB galaxies with Log(M$_\star$/M$_\odot$) > 10 reaches 3 orders of magnitudes. At larger radii ($r > 5$ kpc) the SFR surface density decreases significantly in SB, SUP1 and MS galaxies, reaching values comparable with the SUB1/2 and QUIE subsamples, that on contrary are characterised by a

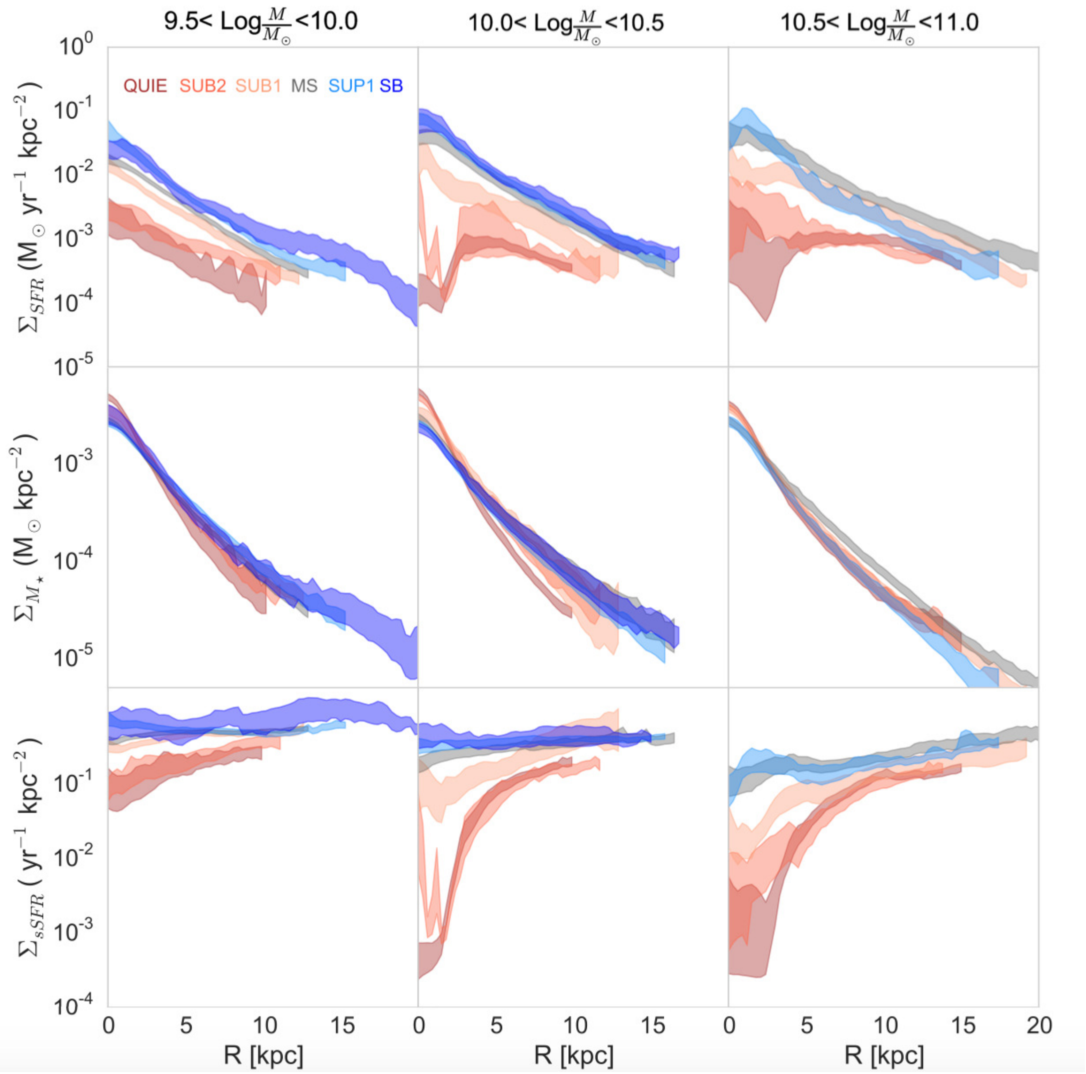

Figure 4.8: Same as Fig.4.6, but for galaxies in the redshift range [0.7:1.2].

dip in the SFR distribution at small radii.

The second row of Fig. 4.6 shows the stellar mass profiles of galaxies. We recall here that each single profile has been normalised for the total stellar mass obtained integrating the profile, to account for differences in $M_\star$ within the 0.5 dex bin, before the computation of the median profile. As expected, passive galaxies are always less extended and more concentrated with respect to MS galaxies. MS galaxies become more extended with increasing stellar mass and their mass distribution seems to become more enhanced at the centre, consistent with the idea of the build-up of the bulge component in MS galaxies with increasing stellar masses. Galaxies located above the MS are more extended than MS counterparts, and show no central enhancement of their stellar mass distribution. The third row of Fig. 4.6 shows the sSFR profiles of galaxies. At large radii, r > 5 kpc,

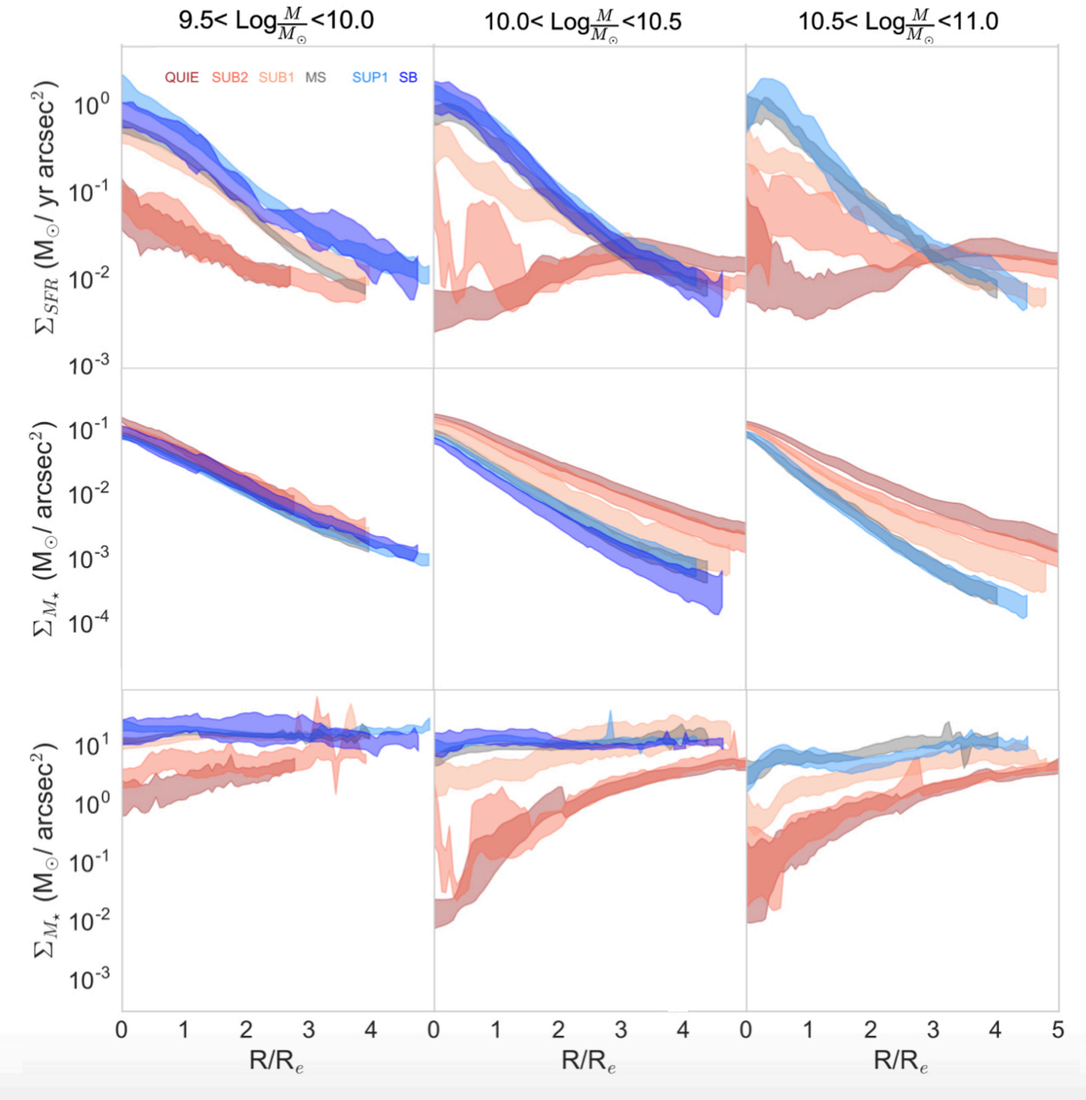

Figure 4.9: Same as Fig.4.7, but for galaxies in the redshift range [0.7:1.2].

the median sSFR profile does not show significant differences for the subsamples of galaxies located at various distances from the MS; galaxies with the largest SFR (SB) and QUIE ones have the same sSFR surface density, or they differ of $\lesssim 0.5$ dex. At small radii, $r < 5$ kpc, the sSFR profiles depend dramatically on the distance from the MS. The sSFR profiles of galaxies below the MS are characterised by a decrease which is proportional to the distance from the MS, with QUIE galaxies showing the largest decline. MS and SUP1 galaxies are characterised by a small decline of sSFR in the inner radii, while SB galaxies have flat or enhanced sSFR profile in the innermost 5kpc.

The trends observed in Fig. 4.6, in which the surface densities are shown as a function of the physical distance from the centre (in kpc) are also observed in Fig. 4.7 where we the surface densities are shown as a function of the distance from the centre, normalised by the galaxies' effective radii. At r $< 2R_e$ the SFR and sSFR surface densities of the most star forming galaxies (SB) and of galaxies below the MS (SUB1 & 2) differ up to 2 orders of magnitude, and the difference increases when considering QUIE instead of SUB galaxies. On the contrary, at r $> 2R_e$ the median profiles of SFR and sSFR do not show significant differences among the different subsamples.

Figures 4.8 and 4.9 show the median SFR, stellar mass, and SFR profiles of galaxies in the *high-z* sample, computed as a function of the physical distance from the centre in kpc or normalised by R_e, respectively. No significant evolution within the two redshift bin is observed, as the trends in the *high-z* sample are very similar to the *low-z* one. The only difference concerns the SFR profile of SB galaxies (notice that we do not have SB galaxies in the most massive bin). While in the *low-z* sample the SB SFR profile is the one characterised by the largest SFR surface density at small radii, in the *high-z* one the SFR profile of SB galaxies is consistent with the one of SUB1 and MS galaxies.

To further study the mass distribution in galaxies above/below the MS, both in the low and high redshift sample, we show in Fig.4.10 the distribution of the average Sérsic index n as a function of the distance from the MS, Δ_{MS}. The Sérsic index used here is the one that was obtained as output of the GALFIT fitting procedure explained in Sec. 4.2.5. The errorbars in this analysis have been computed via bootstrapping. We observe, as discussed qualitatively when analysing the stellar mass profiles, a quasi-monotonic decrease of n with increasing Δ_{MS} in each stellar mass and redshift bin: galaxies below the MS are more concentrated than galaxies located on the MS or above it. Galaxies on the MS become more concentrated with increasing stellar mass, transforming from pure disks structures to bulge+disk ones. Also for galaxies below the MS the n increases with increasing stellar mass. No increase in n is observed in galaxies above the MS with respect to MS counterparts at fixed stellar mass.

4.3.2 Stacked maps

From what has been discussed thus far, the central part of a galaxy seems to be the key in determining its location in the LogSFR-LogM$_\star$ plane. Nevertheless, the sSFR and SFR surface density profiles from which these conclusions are drawn come from SED fitting, which is very sensitive to dust and, in general is the least stable method to derive SFRs. For this reason, we decided to further investigate the distribution of dust and UV luminosity (corrected and not-corrected for dust). Fig. 4.11 shows the stacked maps of SFR, stellar mass, sSFR, not-corrected UV

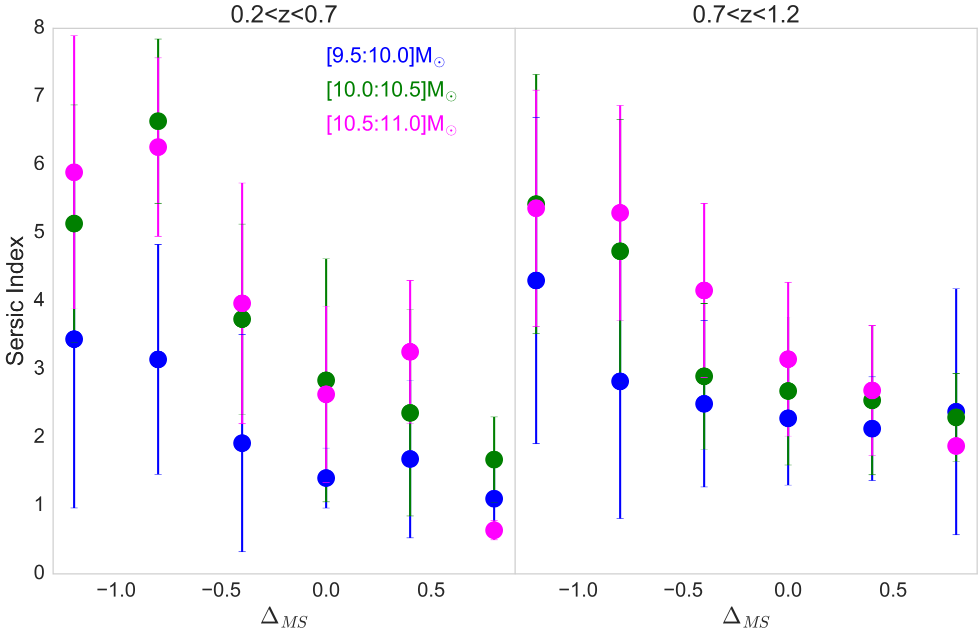

Figure 4.10: Sérsic index, obtained from the GALFIT fit, as a function of distance from the MS, Δ_{MS}, for the low and high redshift samples (left and right panels, respectively). The three stellar mass bins are represented with different colours.

luminosity, dust-corrected UV luminosity and E(B-V). The stacked maps have been built by excluding galaxies with $q < 0.4$ and $0.01'' < re < 0.8''$. These cuts avoid biases due to highly inclined galaxies, or to extremely compact or extremely extended galaxies that are not representative of the galaxy population in the bins. We focus is on the range $0.04 < z < 0.7$ and $9.5 <$ Log($M_\star/M_\odot$)< 10.0 so as to ensure the best statistics while trying to limit the width of the redshift range, as intrinsic differences in the shape of galaxies at different cosmic times can bias the results.

The SFR maps show a monotonic increase of the SFR in the centre of galaxies when moving towards larger integrated SFRs. We underline here that even if the star formation activity is taking place in clumps in individual galaxies, the stacking procedure produces a "smooth" distribution of SFR in the disk. In the SB bin, the distribution of SFR (as well as other properties) looks more disturbed, as the number of galaxies in this bin is lower. Nevertheless, the increase of SFR in the central part is visible. The mass distribution clearly shows that galaxies below the MS, in the quiescent region of the LogSFR-LogM$_\star$ plane, are more concentrated than MS and upper MS galaxies, reflecting the trends in Sérsic index observed both in the *low-z* and *high-z* sample (Fig.4.10). As discussed above, galaxies above the MS are more extended than MS counterparts. sSFR maps enhance the trends visible in the SFR maps. Below the MS we can clearly see that star formation activity is taking place only in the outskirts of galaxies.

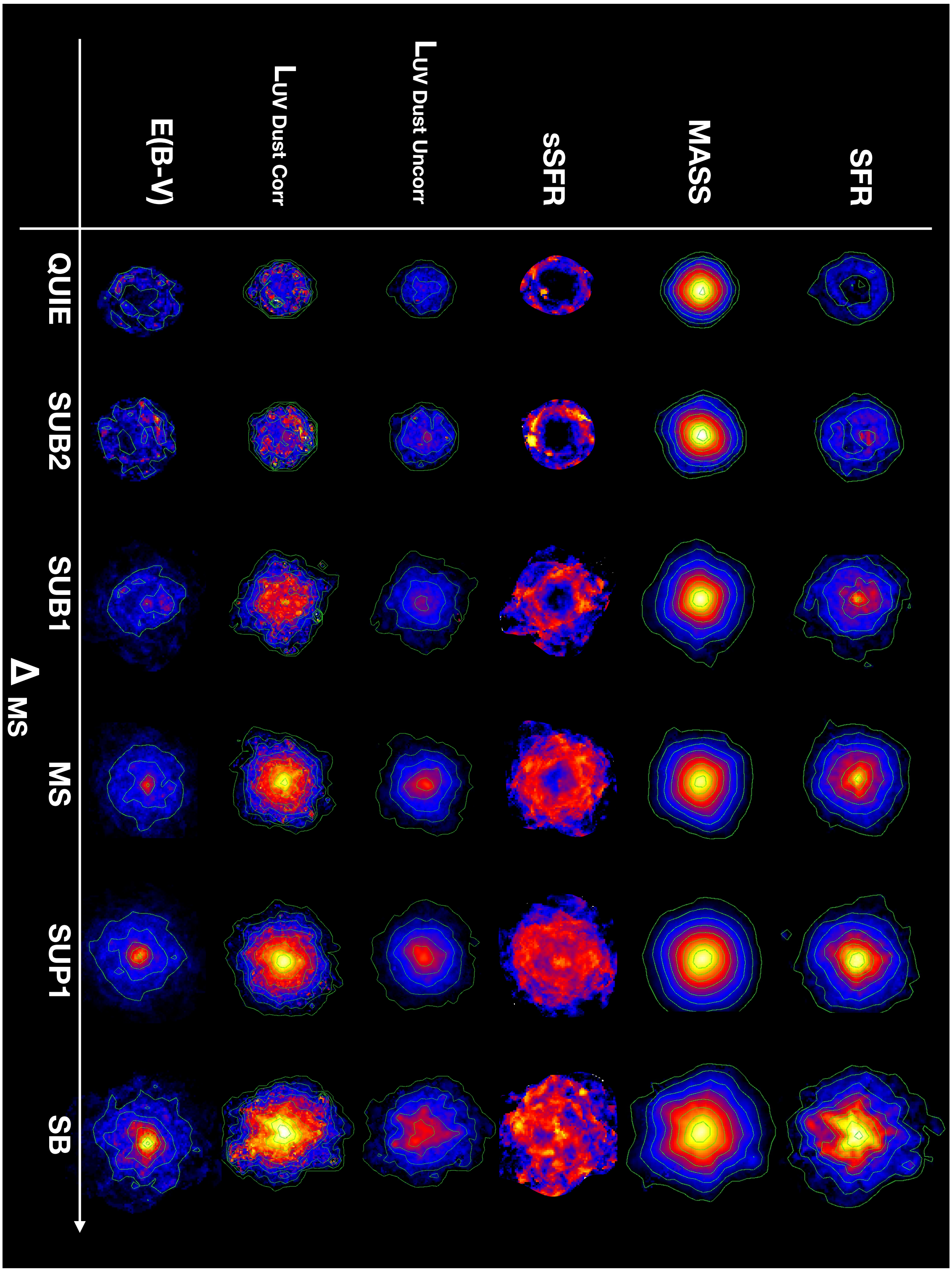

Figure 4.11: From top to bottom: stacked maps of SFR, stellar mass, sSFR, uncorrected L_{UV}, dust corrected L_{UV}, and E(B-V) of galaxies with axis ratio $q > 0.4$, $0.4 < z < 0.7$, and $9.5 < \text{Log}(M_\star/M_\odot) < 10.0$. The six columns are the six bins of distance from the MS.

The position of the clumps of star formation obtained as a result of stacking analysis are irrelevant to the study. However, note that the holes (or the lack of star formation) seen in the central part is a common feature of all the galaxies in the QUI, SUB2, and SUB1 samples. The sSFR in the centre increases in the central part of the galaxy going from the quiescent bins towards the MS, but it is interesting to observe that also in the MS the sSFR in the outskirts is larger than the one in the inner part of the galaxy. Above the MS, the distribution is smoother in the SUP1 sample. In the SB sample, the distribution reveals an increase of sSFR in the central part of the galaxy, as well as other clumps of SF in the outskirts. The UV luminosity maps also show a trend of increasing L_{UV} in the centre with increasing integrated SFR, even without dust correction. The distribution is smooth for QUIE galaxies and progressively peaks in the central part of galaxies when moving towards larger integrated SFRs. Correcting for dust reveals a clumpy distribution of UV luminosity in the outskirts of galaxies in the QUIE and SUB2 samples, and further unveils the presence of a central depression of UV luminosity not visible when dust correction is not taken into account. When dust correction is applied the UV luminosity in the central part of SB galaxies becomes more peaked than for SUP1 and MS galaxies. Finally, the trends seen in dust distribution are analogous to the ones seen for the SFR. A central hole in $E(B-V)$ is visible in the stacked maps of QUIE and SUB2 galaxies, while for the remaining bins the distribution peaks at the centre, and the peak value increases with increasing integrated SFR.

The analysis of the stacked maps of galaxy properties presented in Fig. 4.11 shows that the radial trends observed in SFR and sSFR are reliable against dust correction. We will discuss the possible scenarios arising from such trends in the next section.

4.4 Discussion

In this work we have presented the spatially resolved properties of galaxies in the central region of the GOODS fields up to $z = 1.2$. Studies of resolved properties of galaxies gained importance in the past years, thanks to the increased availability of data at high spatial resolution. We now discuss how our results compare others in literature, as well as the emerging picture on how galaxies move in the LogSFR-LogM$_\star$ plane.

4.4.1 SFR and sSFR profiles at low redshift

The SFR and sSFR profiles of galaxies in the *low-z* sample suggest a fundamental role of the star formation activity in the central part of galaxies in determining the location of a galaxy around the MS and thus in the LogSFR-LogM$_\star$ plane. Galaxies with the largest integrated SFRs are also the ones with the largest SFR and sSFR surface densities in the inner 5 kpc. On the other hand, at any stellar mass galaxies on and below the MS are characterised by a central depression of sSFR. In the outskirts, differences between the SFR surface density of star forming and passive galaxies are more significant in the smallest stellar mass bin, while for more massive galaxies it reaches a maximum value of $\sim$ 0.5 dex. Hence, we can conclude that there is also suppression of star formation in the outskirts for those galaxies that have strongly suppressed star formation in the centre, even if the magnitude of the two is different: $\sim$0.5 dex in the outskirts, and up to 3 dex in the inner part. Spindler et al. (2017) analyse the distribution of star formation activity in MaNGA galaxies and its dependence on integrated mass, structure, and environment. They propose the existence of two classes of galaxies, namely *Centrally Suppressed* and *Unsuppressed*, defined as galaxies that have sSFR in their disk at least 10 times larger than the core, and galaxies with flat sSFR profiles respectively. They find that there is a strong dependence of the classification of galaxies as *Centrally Suppressed* and *Unsuppressed* on stellar mass. This is consistent with our finding of more pronounced decrease of sSFR in the inner part of galaxies with increasing stellar mass. *Centrally Suppressed* galaxies have up to $\sim$ 0.5 dex suppression in their sSFR at larger radii compared to *Unsuppressed* galaxies, which is also the maximum difference seen in the sSFR values at r $>$ 5 kpc for star forming and quiescent galaxies. Finally, when studying the dependence of central suppression of star formation on galaxy morphology they conclude that it is strongly related to the presence of a bulge, in agreement with our findings of increased Sérsic index in galaxies with the deepest central depression in their sSFR profiles. Belfiore et al. (2017), analysing the Hα equivalent width profiles of MaNGA galaxies, found that the typical sSFR profile of MS galaxies is flat at LogM$_\star$ $<$ 10.5 M$_\odot$, while the sSFR of more massive MS galaxies shows a decrease in the central region. This result is partially in disagreement with our findings for the *low-z* sample, as we observe that the sSFR profiles of MS galaxies is always smaller in the central 5 kpc than at larger radii even if the difference is only up to 0.5 dex. This discrepancy is most likely due to different selection criteria for MS galaxies in the two works. In fact, in Belfiore et al. (2017) MS galaxies are not distinguishable from upper MS galaxies and SB, where the profile might show an enhancement according to our results. As a consequence, the median profile is flat and shows a decrease at inner radii only at larger stellar masses, when the depression in the SFR profile of MS galaxies becomes more significant. Our median SFR profiles as a function of galaxies' distance from the MS are compatible with the ones reported by Ellison et al. (2017). In both studies, galaxies above the MS are characterised by a considerable enhancement of SFR surface density in the central regions, while passive galaxies show a depression in their SFR profiles in the inner part. The result of centrally-suppressed SFR profile in passive galaxies is also in agreement with the study of Delgado et al. (2013) where they analysed CALIFA galaxies to study dependency of the SFR profile on morphological classification. They find that SFR profiles of disk-like galaxies increase towards the centre, while $S0$ galaxies and ellipticals have suppressed profiles particularly at the centre. This is compatible with our observations as galaxies whose SFR profile is suppressed at the centre also exhibit Sérsic indexes comparable to bulge+disk systems, or pure spheroidal morphologies.

We can compare the trends seen in the SFR profiles with photometric results at low redshift, extracted from SDSS galaxies. In Morselli et al. (2017) the authors studied the colour of bulges and disks as a function of the location of a galaxy in the LogSFR-LogM$_\star$ plane, and found that galaxies in the upper envelope of the MS are not only more bulge-dominated than MS counterparts, but that their bulge is also significantly bluer. This is in agreement with an increase of the central SFR surface density when moving from the MS towards its upper envelope. Nevertheless, while in Morselli et al. (2017) bulges were found to be already "red and dead" on the MS, hence implying the reddening of the disk to be responsible of moving a galaxy towards the passive region, in this work the SFR surface density of the central region decreases more significantly than in the outskirts. Further work needs to be done in order to understand the interplay between bulge and disk in moving a galaxy in the passive region, especially in the local Universe where morphological classification of galaxies with intermediate bulge+disk morphology is more reliable.

4.4.2 SFR and sSFR profiles at high redshift

As we discussed above, no evolution is seen between the *low-z* and *high-z* samples. The only significant difference between the two samples is related to SB galaxies. In fact, while at *low-z* the SFR and sSFR profiles of SB galaxies show a central enhancement compared to galaxies at lower integrated SFRs, at *high-z* the the profiles of SB and SUP1 are consistent. This is most likely due to a larger amount of dust expected at higher redshifts, especially in galaxies with the largest SFRs, resulting in uncertain dust correction estimates. Below the MS, galaxies in the SUP2 and QUIE subsamples show significantly flatter SFRs than their MS counterparts, or are characterised by a central depression as seen in the *low-z* case. The central suppression/enhancement seen in the SFR and sSFR profiles in this work is in disagreement with the coherent star formation picture of Nelson et al. (2016), where the authors presented the average surface brightness profiles of H$_\alpha$ and stellar continuum emission for 3DHST galaxies in the redshift range [0.7:1.5]. They find that above the MS the H$_\alpha$ profile is enhanced at all radii, while below the MS, it is suppressed at all radii. On the contrary, our findings point towards a key role of the inner region ($\lesssim$ 5 kpc) in placing a galaxy below the MS. As discussed previously, more caution needs to be taken for galaxies in the upper envelope of the MS, but there are hints suggesting that the difference between the SFR and sSFR surface densities of SUB1 and MS galaxies is larger at small radii than in the outskirts, as seen at lower redshifts. The SFR surface density in the outskirts of galaxies above the MS is enhanced with respect to MS galaxies only in the smallest stellar mass bin, while it is comparable or smaller in the other stellar mass bins. One possible explanation for the significant difference in the results of work and Nelson et al. (2016) lies in the selection of MS, below MS and above MS galaxies. In fact, in the work of Nelson et al. (2016) galaxies above the MS are selected as the ones located in the region at 0.4 - 1.2 dex above the relation, but the bulk of the sample is located at a maximum distance of 0.6 dex from the MS. On the other hand, galaxies below the MS have been selected to be at a distance between -0.4 and -0.8 from the MS, but again due to the gaussian nature of the relation, the bulk of the population lies within -0.4 and -0.6 dex from the MS. Thus, the stacked H_α profile below the MS is dominated by galaxies that are close to the MS sample, that according to our results as well do not show a significant decrease of the SFR in the inner part. On the other hand, in comparison to the work of Nelson et al. (2016) the smaller statistics of this work (as we focus on the inner part of the GOODS fields), translates to a smaller number of galaxies located ~1 dex above the MS that are intrinsically rare. These objects might be the ones with a different distribution of SFR surface density, causing the enhancement of SFR at large radii.

Other recent works investigating the spatial distribution of SFR in galaxies are based on small samples for which high spatial resolution data is available. Tacchella et al. (2015c) studied H_α derived SFR profiles in 22 galaxies at $z \sim 2$ (resolution ~ 1 kpc) and observed that the profiles averaged in stellar mass bins do not change with stellar mass (and are consistent with a disk-like profile). We also do not observe significant changes in the SFR profiles of MS galaxies at different stellar masses. More recently, Tacchella et al. (2017) studies dust and UV profiles for 10 galaxies at $z \sim 2$ and found centrally suppressed sSFR profiles only in the most massive bin ($M_\star > 10^{11} M_\odot$), while a flat sSFR profile is observed at $M_\star > 10^{11} M_\odot$. In our sample, central suppression is always visible in the sSFR profiles of galaxies in the *high-z* sample, but the suppression becomes more significant at increasing stellar masses. In the same work, the authors also argue that galaxies above the MS have sSFR characterised by a central enhancement, in agreement with what is suggested by the trends in our profiles.

4.4.3 Stellar mass distribution across - along the MS

While our work on the sSFR and SFR profiles is in clear agreement with previous results, the trends in stellar mass distribution across the MS and for galaxies with the largest SFRs present a challenge. In Morselli et al. (2017) we study the the structure of z $\sim$ 0 SDSS galaxies using the B/T decomposition of Simard et al. (2011) and find that the MS of star-forming galaxies corresponds to the minimum of the B/T distribution at each stellar mass; in other words, galaxies in the upper envelop of the MS are characterised by a larger B/T with respect to MS counterparts. The result, while in agreement with the original work of Wuyts et al. (2011a), does not comply with the findings of this work where an opposite trend of decreasing Sérsic index is observed when moving from the MS towards its upper envelope. We propose two possible explanations behind this discrepancy. Firstly, the light profile (on which the morphological classification of Morselli et al. (2017) and Wuyts et al. (2011a) are based) of galaxies above the MS is more concentrated than the mass profile (from which the Sérsic indexes of this work were computed). Secondly, since we employ the small inner region of the GOODS sample, we are missing real starburst galaxies located more than one dex above the MS. These galaxies that we miss in our current sample could be pure spheroidals (Almaini et al., 2017), the inclusion of which would increase the average Sérsic index of galaxies above the MS.

On the other hand, the morphological trend of increasing Sérsic index along the MS is confirmed by different works in recent literature, both at low (Bluck et al., 2014; Morselli et al., 2017) and high (Lang et al., 2014) redshift. Such trends, together with the more pronounced decrease of the sSFR of MS galaxies with increasing stellar mass, indicate that galaxies grow their bulge component while moving along the MS, and that star formation in massive MS galaxies takes place only in the disk, while the bulges remain passive.

4.4.4 Moving galaxies across the MS and implications on quenching mechanism

The shapes of the observed SFR and sSFR profiles are compatible with the compaction-depletion scenario of Tacchella et al. (2015b), based on the VELA simulations (Ceverino et al., 2014). These studies propose a scenario where star forming galaxies migrate across the MS due to the successive episodes of gas inflow and star formation ongoing in the central part. Here, cold gas flowing to the inner region of galaxies causes an overall compaction of the system, which in turn leads to a phase of high star formation activity. Following this, central depletion of gas due to star formation forces a galaxy below the MS. As a result, sSFR profiles of galaxies are expected to be centrally enhanced (suppressed) above (below) the MS, which is in good agreement with our findings.

The shape of the SFR and sSFR profiles is also a powerful tool to obtain information on the nature of the quenching mechanism. The coherent star formation picture presented in Nelson et al. (2016) was used to conclude that the suppression of star formation at all radii, observed for galaxies below the MS, must be related to a quenching mechanism that acts not only in the central part of galaxies but also troughout the disk. The central suppression observed in the sSFR profiles of galaxies below the MS is compatible with the so-called $inside - out$ quenching mechanism, where the star formation halts first in the innermost radii and then in the outer regions of the disk, implying that disks are still forming stars when the central part of a galaxy is dominated by a passive bulge. Such a quenching mechanism has been advocated frequently in recent studies. Morishita & Ichikawa (2016) used HST/WFC3 and ACS observations to study UV rest frame colours of Milky Way progenitors in $0.5 < z < 3$. Despite the uncertainties in using UV colours as SFR tracers, they find that quenching must first occur in the central region, followed by the outskirts. Tacchella et al. (2015a) employ the centrally-suppressed sSFR profiles of massive MS galaxies to conclude that quenching must proceed in an $inside - out$ fashion, with timescales ranging from 1 billion years in the central regions to a few billion years at larger radii. In Tacchella et al. (2016) the authors used cosmological simulations to extract a sample of 26 galaxies at $1 < z < 7$ and found that the onset of gas depletion occurs in the central 1 kpc and follows a phase of wet compaction and SFR peaked in the centre. The quenching hence also proceeds $inside - out$, implying that when the central region is passive star formation is still ongoing in an outer ring. A small sample of 10 star forming galaxies at z $\sim$ 2, observed as part of a SINS/zC-SINF AO program, is used in Tacchella et al. (2017) to study dust and UV profiles. They find that only massive galaxies ($\mathrm{M}_\star > 10^{11}\mathrm{M}_\odot$) show sSFR profiles that are suppressed in the centre with respect to the outskirts and hence must be experiencing $inside - out$ quenching. More work needs to be done in order to understand the main driver behind the suppression of the central star formation.

4.4.5 Summary

In this work, we study the spatially resolved properties of galaxies located in the central parts of the GOODS fields. We summarise our main findings as follows:

- the sSFR profiles of galaxies in the redshift range $0.2 < z < 1.2$ is centrally enhanced above the MS and centrally suppressed below the MS, with quiescent galaxies characterised by the deepest suppression. The sSFR in the outer region does not show systematic trends of enhancement or suppression above or below the MS.

- the Sérsic index of MS galaxies increases with increasing stellar mass, indicating that bulges are growing when galaxies are still on the relation. Galaxies are also more bulge-dominated in the lower envelop of the MS, while galaxies in the upper envelop are more extended and have Sérsic indexes that are always smaller than or comparable to their MS counterparts.

These findings suggest that galaxies above the MS could be in a evolutionary phase where cold gas is available in the central region, possibly due to minor mergers or disk instabilities, but no compaction has still taken place. Furthermore, our work indicates that $inside-out$ quenching is indeed taking place, as star formation is centrally-suppressed in galaxies below the MS, but still occurs in the outer regions. Follow up studies are warranted in order to: 1) increase the statistics, especially above the MS so as to cover the area at $\sim$1 dex from the relation, and 2) investigate the spatial distribution of cold gas so as to understand the reasons behind the growth of the bulge observed below the MS, e.g. the stabilisation of the disk against further collapse vs. removal of cold gas due to AGN activity.

5 Conclusions

In this thesis, we have studied the scatter around the MS as a function of the spatial distribution of the star formation activity within galaxies. In the local Universe, this was done by exploiting the bulge-disk decomposition of SDSS galaxies and using the color of the individual components as a tracer of their star formation activity. In the redshift range $0.2 < z < 1.2$ this was achieved by studying the SFR and sSFR distribution within galaxies. Both approaches suggest a fundamental role of the star formation activity in the central part of galaxies in determining the location of a galaxy around the MS and, generally speaking, in the LogSFR - LogM$_\star$ plane. The photometric study of SDSS galaxies published in Morselli et al. (2017) and presented in Chapter 2 suggests that the individual star formation activity of a galaxy's components define its location around the MS. The upper envelope of the MS is populated by galaxies that are more bulge-dominated than MS counterparts, and with blue or extremely dusty bulges. Galaxies with blue disks but red and dead bulges are found on the MS relation, while structures with red disks and red bulges are found below the MS. These trends seem to indicate that a process responsible for the reddening of the disk component must be in place and responsible for moving galaxies from the relation to the passive region. The photometric trends are in agreement with the recent results of Ellison et al. (2017), based on MaNGA galaxies, who report that galaxies above the MS are characterised by an enhancement of SFR surface density in the central regions, while passive galaxies show a depression in their SFR profiles in the inner part, and a less significant difference at larger radii.

The study on the SFR and sSFR profiles shown in Chapter 4 confirms the importance of the SFR activity of the inner radii in setting the position of a galaxy with respect to the MS. In particular, we found that central star formation activity is enhanced above the MS, suppressed below the MS, and heavily suppressed in the passive region, while star formation activity in the outskirts varies by a small amount compared to the inner part. Our results are in good agreement with recent studies based on spatially resolved observations of galaxies, both at low and at high redshift. The more pronounced decrease observed in the sSFR in the inner part of galaxies with increasing stellar mass is also observed in Spindler et al. (2017), a study based on MaNGA galaxies. The authors also find that galaxies with centrally-suppressed sSFR profiles show a difference of 0.5 dex in the sSFR at outer radii with respect to galaxies with flat inner sSFR profiles, also in compliance with our findings. The central suppression of the sSFR profile in MS galaxies is also found when studying the Hα profile of MS massive galaxies (Belfiore et al., 2017).

While at low redshift a coherent picture is emerging, where the SFR of the inner part plays a major role in determining the MS scatter, at larger redshifts the situation is less clear. Our results are not in agreement with the work of Nelson et al. (2016), where they find that above the MS the H_α profile is enhanced at all radii, while below the MS, it is suppressed at all radii, in a so-called coherent star formation picture. Other works in literature agree with our findings on the enhancement/suppression of the star formation activity above/below the MS Tacchella et al. (2015c, 2017). Thus more works needs to be done in order to understand the typical SFR profiles of galaxies above and below the MS at $z \sim 1$.

The shapes of the observed SFR and sSFR profiles are compatible with the compaction-depletion scenario of Tacchella et al. (2015b), based on the VELA cosmological zoom-in hydrodynamical simulations (Ceverino et al., 2014). These studies together present a paradigm where star forming galaxies oscillate above and below the MS depending on the interplay between gas inflow and star formation that occurs in the central part. In this scenario, the flow of cold gas in the inner region of galaxies could be enabled by minor mergers or violent disc instabilities, thus causing an overall compaction of the system. The compaction phase leads to high star formation activity in the central region of galaxies, and in turn leads results in bulge growth for galaxies above the MS. Gas exhaustion in the central region would then shift a galaxy below the MS. In this scenario, sSFR profiles are expected to be centrally enhanced (suppressed) for galaxies above (below) the MS, in agreement with our findings. Also in agreement with this scenario is the progressive bulge growth of galaxies along the MS that is found both at low and at high redshift, which is presented in this thesis as well as reported by other studies in literature (Bluck et al. 2014, Lang et al. 2014, Morselli et al. 2017). That said, the scenario concerning the mass distribution across the MS is unclear. While in local galaxies, at every stellar mass, we see an increase of the bulge dominance in galaxies above and below the MS with respect to MS counterparts, such trends do not characterise the stellar mass profiles of galaxies at $z > 0.2$. Further work needs to be done in order to understand the origin of the discrepancy between our results and contrasting claims in literature (e.g. Wuyts et al., 2011). Such a study would unravel a coherent picture of the mass distribution in the most actively star forming galaxies.

We also discussed the implications of our findings on the quenching mechanism. The analysis of the bulge and disk colours above/below the MS revealed that a characteristic feature of galaxies located below the MS is the reddening of the disk component. When studying correlations between the colour of the disk and quantities used as proxy for different quenching mechanisms (BH mass, B/T, and

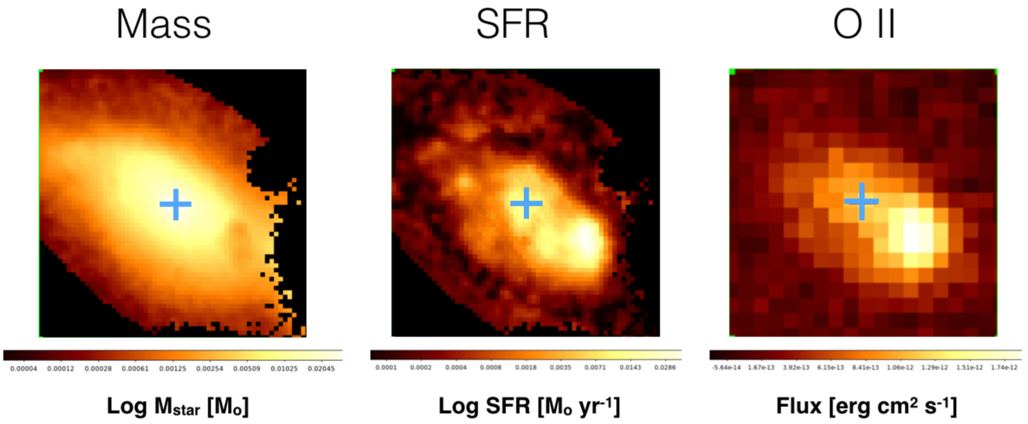

Figure 5.1: Stellar mass map (left panel), SED-based SFR map (central panel) and OII flux map (right panel) of a galaxy in the sample described in Chapter 4.

DMH mass) we found that the two quantities that have the largest correlation coefficients are the BH mass and the B/T, but the large scatter reveals that none of the quantities alone plays a prominent role in determining the passivity of a galaxy. Nevertheless, the presence of the bulge seems to be a necessary condition for passivity, as bulge-less passive galaxies constitute a non-significant tail of the quiescent population. The analysis of the SFR and sSFR profiles instead revealed that the passivity of the disk component is not the main characteristic of quiescent galaxies at $z > 0.2$. The fundamental role of the inner part in placing a galaxy in the LogSFR - Log$M_\star$ plane can be interpreted as a result of the so-called $inside - out$ quenching mechanism, where the star formation halts first in the innermost radii and then in the outer regions of the disk, implying that disks are still forming stars when the central part of a galaxy is dominated by a massive bulge (e.g. Tacchella et al., 2016; Morishita & Ichikawa 2016; Tacchella et al. 2016; Tacchella et al. 2017). Galaxies located below the MS and in the quiescent region are more bulge-dominated than MS counterparts and, at the same time, are characterised by centrally-suppressed sSFR profiles. This indicates that a possible relation is in place between the mechanism responsible for the growth of the bulge and for halting the star formation. Further work needs to be done in order to understand the reason for bulge growth, e.g. disk stabilisation against instabilities preventing cold gas from collapsing and forming new stars (as expected in the morphological quenching scenario), vs. internal processes related to bulge growth like AGN feedback. Studies of the distribution of cold gas in galaxies above and below the MS will play a key role in obtaining a clearer picture of quenching.

This work serves as a motivation for future studies to further investigate the link between the morphology of galaxies and their star formation activity, with special focus on the scatter of the MS relation. I have already commenced work in this direction at the time of writing this the thesis, as summarised below.

- Analysis of the distribution of dust in local galaxies in the MaNGA and CALIFA survey: to help understand the inter-dependancy between SFR and dust in inclined galaxies.
- Analysis of OII distribution as a proxy of SFR in galaxies observed with MUSE (Bacon et al., 2004): to validate our results obtained using SED-based SFRs, as shown in Fig. 5.1.

In addition, a comparison between the photometric bulge-disk decomposition and the one based on spatially resolved kinematics (from MaNGA, CALIFA or SAMI) will be essential in determining the reliability of decomposition codes based on photometry. Finally, studies of the distribution of molecular gas in galaxies (carried out, for example, with ALMA) are essential to further constrain the scatter of the MS and its relation to galaxy morphology.

Acknowledgements

First and foremost I want to thank my supervisor Dr. Paola Popesso, that despite not being my official supervisor is the person that gave me the opportunity to come to Munich to start my PhD and my career as a researcher and followed me during these four and a half years. She thought me the ability to handle difficult situations and I look up to her as a woman with a family thriving in science. I want to thank my official supervisor, Prof. Elisa Resconi, for her availability and kindness that were always present also in the busiest times. I am thankful to Dr. Ghazaleh Erfanianfar for the help received in the initial phases of my PhD, and I apologise for all the stupid questions I asked her. She always had a great patience with me, and I thank her for that. A special thank goes to Professors Alvio Renzini and Pascal Oesch, with whom I had the fortune to collaborate during my PhD. Prof. Renzini is an inspiration; in him the thirst for answers and the passion for science seem to be never ending. Prof. Oesch gave me the opportunity to enter the HDUV collaboration and I immensely thank him for the trust he gave me. I want to thank the Excellence Cluster staff, in particular Sonja Lutz, for all the help she offered me in navigating bureaucratic processes.

During the years I spent in Munich I had the opportunity to share the stress and happiness of my PhD with many other PhD students and PostDocs. A big thank goes to Angeles, Anna and Alessia for having shared with me the payment of the college fees of the son/daughter of the Chinese restaurant's owner in Garching. Despite having spent there an incredible amount of time, it is amazing how the dishes we tried from the menu are only five! Also, a big thank for having supported my crazy running ideas! I wish you three all the best, as you really are good people. I want to thank Matias, as he has been a good friend in this time. I also want to thank Karina, Chris, Claudia, Florian, Matthieu, Matteo, Fabrizio, Jethro for the fun times we spent together. I have beautiful memories of the time here that I will keep with me for the rest of my life.

A special hug goes to the friends in Italy that despite the distance I always feel extremely close to me. Thank you Mirco, for your daily messages on Whatsapp checking on my status and your genuine invasive happiness, Sara and the other girls for the laughs every time I come home, Irene and Cippi for listening to me when I needed a friend to talk to. Thank you Breu and Marcio for making me feel like we are still in high school every time we meet all together.

If I am here in this moment writing the acknowledgements in my PhD thesis is mostly due to the constant support of one person. Bhaskar, you are not just my partner in love, laughs and life, you are the person that more than everyone else in the world believes in me and my abilities. Your unconditional support enabled me to see some light when I was lost in the dark tunnels that a PhD student has to inevitably cross. Thank you, with all of me, for being a part of this journey and never loosing hope when I did not know what to do with myself. Thank you for supporting my crazy ideas (i.e. Poldo) despite having to pay severe consequences.

I conclude thanking my family members, that supported me during this adventure, as always.

Bibliography

Abazajian K. N. et al. The Seventh Data Release of the Sloan Digital Sky Survey, 2009, The Astrophysical Journal Supplement, 182, 543

Abell G. O. Clustering of Galaxies, 1965, Annual Review of Astronomy and Astrophysics, 3, 1

Abraham R. G., Valdes F., Yee H. K. C., van den Bergh S. The morphologies of distant galaxies. 1: an automated classification system, 1994, Astrophysical Journal, 432, 75

Abraham R. G., van den Bergh S., Nair P. A New Approach to Galaxy Morphology. I. Analysis of the Sloan Digital Sky Survey Early Data Release, 2003, The Astrophysical Journal, 588, 218

Abramson L. E., Gladders M. D., Dressler A., Oemler A. J., Poggianti B., Vulcani B. Matching the Evolution of the Stellar Mass Function Using Log-Normal Star Formation Histories, 2015, The Astrophysical Journal Letters, 801, L12

Abramson L. E., Kelson D. D., Dressler A., Poggianti B., Gladders M. D., Oemler A. J., Vulcani B. The Mass-independence of Specific Star Formation Rates in Galactic Disks, 2014, The Astrophysical Journal Letters, 785, L36

Allen P. D., Driver S. P., Graham A. W., Cameron E., Liske J., De Propris R. The Millennium Galaxy Catalogue: Bulge/Disc Decomposition of 10095 Nearby Galaxies, 2006, arXiv.org, 2

Almaini O. et al. Massive post-starburst galaxies at z $>$ 1 are compact proto-spheroids, 2017, Monthly Notices of the Royal Astronomical Society, 472, 1401

Alpher R. A., Bethe H., Gamow G. The Origin of Chemical Elements, 1948, Physical Review, 73, 803

Andredakis Y. C., Sanders R. H. Exponential bulges in late-type spirals: an improved description of the light distribution, 1994, Monthly Notices of the Royal Astronomical Society, 267, 283

Arnouts S., Cristiani S., Moscardini L., Matarrese S., Lucchin F., Fontana A., Giallongo E. Measuring and modelling the redshift evolution of clustering: the Hubble Deep Field North, 1999, Monthly Notices, 310, 540

Athanassoula E. Secular Evolution of Disc Galaxies and of their Components, 2008, Mapping the Galaxy and Nearby Galaxies, 4, 47

Bacon R. et al., 2004, in Ground-based Instrumentation for Astronomy. Edited by Alan F. M. Moorwood and Iye Masanori. Proceedings of the SPIE, Observatoire de Lyon, France, SPIE, pp. 1145–1149

Bahé Y. M., McCarthy I. G., Balogh M. L., Font A. S. Why does the environmental influence on group and cluster galaxies extend beyond the virial radius?, 2013, Monthly Notices of the Royal Astronomical Society, 430, 3017

Baldry I. K., Balogh M. L., Bower R. G., Glazebrook K., Nichol R. C., Bamford S. P., Budavari T. Galaxy bimodality versus stellar mass and environment, 2006, Monthly Notices of the Royal Astronomical Society, 373, 469

Balogh M. L., Baldry I. K., Nichol R., Miller C., Bower R., Glazebrook K. The Bimodal Galaxy Color Distribution: Dependence on Luminosity and Environment, 2004, The Astrophysical Journal, 615, L101

Bamford S. P. et al. Galaxy Zoo: the dependence of morphology and colour on environment*, 2009, Monthly Notices of the Royal Astronomical Society, 393, 1324

Behroozi P. S., Wechsler R. H., Conroy C. On the Lack of Evolution in Galaxy Star Formation Efficiency, 2013a, The Astrophysical Journal Letters, 762, L31

Behroozi P. S., Wechsler R. H., Conroy C. The Average Star Formation Histories of Galaxies in Dark Matter Halos from z = 0-8, 2013b, The Astrophysical Journal, 770, 57

Belfiore F. et al. SDSS IV MaNGA - sSFR profiles and the slow quenching of discs in green valley galaxies, 2017, arXiv.org, arXiv:1710.05034

Bell E. F. Galaxy Bulges and their Black Holes: a Requirement for the Quenching of Star Formation, 2008, The Astrophysical Journal, 682, 355

Bell E. F. et al. Toward an Understanding of the Rapid Decline of the Cosmic Star Formation Rate, 2005, The Astrophysical Journal, 625, 23

Bertola F., 1987, in IN: Structure and dynamics of elliptical galaxies; Proceedings of the IAU Symposium, Padova, Università, Padua, Italy, pp. 135–144

Binney J. The physics of dissipational galaxy formation, 1977, Astrophysical Journal, 215, 483

Birnboim Y., Dekel A. Virial shocks in galactic haloes?, 2003, Monthly Notices of the Royal Astronomical Society, 345, 349

Birnboim Y., Dekel A. Gravitational quenching by clumpy accretion in cool-core clusters: convective dynamical response to overheating, 2011, Monthly Notices of the Royal Astronomical Society, 415, 2566

Birnboim Y., Dekel A., Neistein E. Bursting and quenching in massive galaxies without major mergers or AGNs, 2007, Monthly Notices of the Royal Astronomical Society, 380, 339

Blanton M. R., Eisenstein D., Hogg D. W., Schlegel D. J., Brinkmann J. Relationship between Environment and the Broadband Optical Properties of Galaxies in the Sloan Digital Sky Survey, 2005, The Astrophysical Journal, 629, 143

Blanton M. R., Moustakas J. Physical Properties and Environments of Nearby Galaxies, 2009, Annual Review of Astronomy and Astrophysics, 47, 159

Blanton M. R., Roweis S. K-Corrections and Filter Transformations in the Ultraviolet, Optical, and Near-Infrared, 2007, The Astronomical Journal, 133, 734

Bluck A. F. L., Mendel J. T., Ellison S. L., Moreno J., Simard L., Patton D. R., Starkenburg E. Bulge mass is king: the dominant role of the bulge in determining the fraction of passive galaxies in the Sloan Digital Sky Survey, 2014, Monthly Notices of the Royal Astronomical Society, 441, 599

Boselli A., Cortese L., Boquien M., Boissier S., Catinella B., Gavazzi G., Lagos C., Saintonge A. Cold gas properties of the Herschel Reference Survey. III. Molecular gas stripping in cluster galaxies, 2014, Astronomy & Astrophysics, 564, A67

Boselli A., Gavazzi G. Environmental Effects on Late-Type Galaxies in Nearby Clusters, 2006, The Publications of the Astronomical Society of the Pacific, 118, 517

Bouché N. et al. The Impact of Cold Gas Accretion Above a Mass Floor on Galaxy Scaling Relations, 2010, The Astrophysical Journal, 718, 1001

Bournaud F., Elmegreen B. G., Elmegreen D. M. Rapid Formation of Exponential Disks and Bulges at High Redshift from the Dynamical Evolution of Clump-Cluster and Chain Galaxies, 2007, The Astrophysical Journal, 670, 237

Bower R. G., Benson A. J., Malbon R., Helly J. C., Frenk C. S., Baugh C. M., Cole S., Lacey C. G. Breaking the hierarchy of galaxy formation, 2006, Monthly Notices of the Royal Astronomical Society, 370, 645

Bower R. G., McCarthy I. G., Benson A. J. The flip side of galaxy formation: a combined model of galaxy formation and cluster heating, 2008, Monthly Notices of the Royal Astronomical Society, 390, 1399

Brandenberger R. H. Cosmological perturbations in a universe dominated by a coherent scalar field, 1985, Physical Review D (Particles and Fields), 32, 501

Brinchmann J., Charlot S., White S. D. M., Tremonti C., Kauffmann G., Heckman T., Brinkmann J. The physical properties of star-forming galaxies in the low-redshift Universe, 2004, Monthly Notices of the Royal Astronomical Society, 351, 1151

Brusa M. et al. The XMM-Newton Wide-field Survey in the Cosmos Field (XMM-COSMOS): Demography and Multiwavelength Properties of Obscured and Unobscured Luminous Active Galactic Nuclei, 2010, The Astrophysical Journal, 716, 348

Bruzual G., Charlot S. Stellar population synthesis at the resolution of 2003, 2003, Monthly Notices of the Royal Astronomical Society, 344, 1000

Burkert A. et al. High-redshift Star-forming Galaxies: Angular Momentum and Baryon Fraction, Turbulent Pressure Effects, and the Origin of Turbulence, 2010, The Astrophysical Journal, 725, 2324

Byrd G., Valtonen M. Tidal generation of active spirals and S0 galaxies by rich clusters, 1990, Astrophysical Journal, 350, 89

Cacciato M., Dekel A., Genel S. Evolution of violent gravitational disc instability in galaxies: late stabilization by transition from gas to stellar dominance, 2012, Monthly Notices of the Royal Astronomical Society, 421, 818

Calzetti D., Armus L., Bohlin R. C., Kinney A. L., Koornneef J., Storchi-Bergmann T. The Dust Content and Opacity of Actively Star-forming Galaxies, 2000, The Astrophysical Journal, 533, 682

Cano-Díaz M. et al. Spatially Resolved Star Formation Main Sequence of Galaxies in the CALIFA Survey, 2016, The Astrophysical Journal Letters, 821, L26

Cappellari M. et al. The ATLAS3D project - I. A volume-limited sample of 260 nearby early-type galaxies: science goals and selection criteria, 2011a, Monthly Notices of the Royal Astronomical Society, 413, 813

Cappellari M. et al. The ATLAS3D project - VII. A new look at the morphology of nearby galaxies: the kinematic morphology-density relation, 2011b, Monthly Notices of the Royal Astronomical Society, 416, 1680

Cattaneo A. et al. The role of black holes in galaxy formation and evolution, 2009, Nature, 460, 213

Cen R. Evolution of Cold Streams and the Emergence of the Hubble Sequence, 2014, The Astrophysical Journal Letters, 789, L21

Chabrier G. Galactic Stellar and Substellar Initial Mass Function, 2003, The Publications of the Astronomical Society of the Pacific, 115, 763

Charlot S., Longhetti M. Nebular emission from star-forming galaxies, 2001, Monthly Notices of the Royal Astronomical Society, 323, 887

Cheung E. et al. Galaxy Zoo: Observing Secular Evolution Through Bars, 2013, arXiv.org, 162

Cheung E. et al. The Dependence of Quenching upon the Inner Structure of Galaxies at 0.5 ¡= z ¡ 0.8 in the DEEP2/AEGIS Survey, 2012, The Astrophysical Journal, 760, 131

Cibinel A. et al. A Physical Approach to the Identification of High-z Mergers: Morphological Classification in the Stellar Mass Domain., 2015, The Astrophysical Journal, 805, 181

Cicone C. et al. Massive molecular outflows and evidence for AGN feedback from CO observations, 2014, Astronomy & Astrophysics, 562, A21

Coenda V., Martínez H. J., Muriel H. Green Valley galaxies as a transition population in different environments, 2017, arXiv.org, arXiv:1710.05928

Collaboration S., Blanton M. R. The Luminosity Function of Galaxies in SDSS Commissioning Data, 2000, arXiv.org, 2358

Combes F. Secular Evolution and the Assembly of Bulges, 2009, Galaxy Evolution: Emerging Insights and Future Challenges ASP Conference Series, 419, 31

Conroy C., Wechsler R. H. Connecting Galaxies, Halos, and Star Formation Rates Across Cosmic Time, 2009, The Astrophysical Journal, 696, 620

Conselice C. J., Wilkinson A., Duncan K., Mortlock A. The Evolution of Galaxy Number Density at z ¡ 8 and Its Implications, 2016, The Astrophysical Journal, 830, 83

Cortese L. et al. The dust scaling relations of the Herschel Reference Survey, 2012, Astronomy & Astrophysics, 540, A52

Cowie L. L., Songaila A. Thermal evaporation of gas within galaxies by a hot intergalactic medium, 1977, Nature, 266, 501

Cowie L. L., Songaila A., Hu E. M., Cohen J. G. New Insight on Galaxy Formation and Evolution From Keck Spectroscopy of the Hawaii Deep Fields, 1996, Astronomical Journal v.112, 112, 839

Cox T. J., Dutta S. N., Hopkins P. F., Hernquist L. Galaxy Mergers: Driving Galaxy Formation, 2008, Panoramic Views of Galaxy Formation and Evolution ASP Conference Series, 399, 284

Croom S. M. et al. The Sydney-AAO Multi-object Integral field spectrograph, 2012, Monthly Notices of the Royal Astronomical Society, 421, 872

Croton D. J. et al. The many lives of active galactic nuclei: cooling flows, black holes and the luminosities and colours of galaxies, 2006, Monthly Notices of the Royal Astronomical Society, 365, 11

Daddi E. et al. Multiwavelength Study of Massive Galaxies at z˜2. I. Star Formation and Galaxy Growth, 2007, The Astrophysical Journal, 670, 156

Dale D. A. et al. The Wyoming Survey for Hα: Initial Results at z 0.16 And 0.24, 2007, American Astronomical Society, 211, 97.03

Davé R., Oppenheimer B. D., Finlator K. Galaxy evolution in cosmological simulations with outflows - I. Stellar masses and star formation rates, 2011, Monthly Notices of the Royal Astronomical Society, 415, 11

De Lucia G., Fontanot F., Wilman D., Monaco P. Times, environments and channels of bulge formation in a Lambda cold dark matter cosmology, 2011, Monthly Notices of the Royal Astronomical Society, 414, 1439

De Lucia G., Springel V., White S. D. M., Croton D., Kauffmann G. The formation history of elliptical galaxies, 2006, Monthly Notices of the Royal Astronomical Society, 366, 499

De Rossi M. E., Avila-Reese V., Gonzalez-Samaniego A., Pedrosa S. Downsizing of galaxies vs upsizing of dark-halos in a Lambda-CDM cosmology, 2013, arXiv.org, arXiv:1309.0919

de Souza R. E., Gadotti D. A., dos Anjos S. BUDDA: A New Two-Dimensional Bulge/Disk Decomposition Code for Detailed Structural Analysis of Galaxies, 2004, arXiv.org, 411

de Vaucouleurs G. Photoelectric photometry of the Andromeda nebula in the UBV system, 1958, Astrophysical Journal, 128, 465

de Vaucouleurs G. Integrated Colors of Bright Galaxies in the u, b, V System., 1961, Astrophysical Journal Supplement, 5, 233

de Vaucouleurs G. Classification of Galaxies by Form, Luminosity and Color, 1962, Problems of Extra-Galactic Research, 15, 3

de Vaucouleurs G., 1974, in In: The formation and dynamics of galaxies; Proceedings of the Symposium, Texas, University, Austin, Tex., pp. 1–52

DeGraf C., Di Matteo T., Treu T., Feng Y., Woo J. H., Park D. Scaling relations between black holes and their host galaxies: comparing theoretical and observational measurements, and the impact of selection effects, 2015, Monthly Notices of the Royal Astronomical Society, 454, 913

Dekel A., Birnboim Y. Galaxy bimodality due to cold flows and shock heating, 2006, Monthly Notices of the Royal Astronomical Society, 368, 2

Dekel A., Burkert A. Wet Disc Contraction to Galactic Blue Nuggets and Quenching to Red Nuggets, 2013, arXiv.org, 1870

Dekel A., Silk J. The origin of dwarf galaxies, cold dark matter, and biased galaxy formation, 1986, Astrophysical Journal, 303, 39

Dekel A., Zolotov A., Tweed D., Cacciato M., Ceverino D., Primack J. R. Toy models for galaxy formation versus simulations, 2013, Monthly Notices of the Royal Astronomical Society, 435, 999

Delgado R. G. et al. CALIFA survey: The spatially resolved star formation history of massive galaxies, 2013, The Intriguing Life of Massive Galaxies, 295, 300

Deng X.-F. A tool for the morphological classification of galaxies: the concentration index, 2013, Research in Astronomy and Astrophysics, 13, 651

Doi M., Fukugita M., Okamura S. Morphological Classification of Galaxies Using Simple Photometric Parameters, 1993, Monthly Notices of the Royal Astronomical Society, 264, 832

Draine B. T. Interstellar Dust Grains, 2003, Annual Review of Astronomy &Astrophysics, 41, 241

Draine B. T. et al. Dust Masses, PAH Abundances, and Starlight Intensities in the SINGS Galaxy Sample, 2007, The Astrophysical Journal, 663, 866

Dressler A. Galaxy morphology in rich clusters - Implications for the formation and evolution of galaxies, 1980, Astrophysical Journal, 236, 351

Dunn R. J. H., Allen S. W., Taylor G. B., Shurkin K. F., Gentile G., Fabian A. C., Reynolds C. S. The radio properties of a complete, X-ray selected sample of nearby, massive elliptical galaxies, 2010, Monthly Notices of the Royal Astronomical Society, 404, 180

Dutton A. A., van den Bosch F. C., Dekel A. On the origin of the galaxy star-formation-rate sequence: evolution and scatter, 2010, Monthly Notices of the Royal Astronomical Society, 405, 1690

Efstathiou G. A model of supernova feedback in galaxy formation, 2000, Monthly Notices of the Royal Astronomical Society, 317, 697

Elbaz D. et al. The reversal of the star formation-density relation in the distant universe, 2007, Astronomy & Astrophysics, 468, 33

Elbaz D. et al. GOODS-Herschel: an infrared main sequence for star-forming galaxies, 2011, Astronomy & Astrophysics, 533, A119

Eliche-Moral M. C. et al. On the buildup of massive early-type galaxies at z ¡ 1. I. Reconciling their hierarchical assembly with mass downsizing, 2010, Astronomy & Astrophysics, 519, A55

Ellison S. L., Sanchez S. F., Ibarra-Medel H., Antonio B., Mendel J. T., Barrera-Ballesteros J. Star formation is boosted (and quenched) from the inside out: radial star formation profiles from MaNGA, 2017, arXiv.org, arXiv:1711.00915

Elmegreen D. M., Elmegreen B. G., Frogel J. A., Eskridge P. B., Pogge R. W., Gallagher A., Iams J. Arm Structure in Anemic Spiral Galaxies, 2002, The Astronomical Journal, 124, 777

Erb D. K., Steidel C. C., Shapley A. E., Pettini M., Reddy N. A., Adelberger K. L. Hα Observations of a Large Sample of Galaxies at z ˜ 2: Implications for Star Formation in High-Redshift Galaxies, 2006, The Astrophysical Journal, 647, 128

Erfanianfar G. et al. Non-linearity and environmental dependence of the star-forming galaxies main sequence, 2016, Monthly Notices of the Royal Astronomical Society, 455, 2839

Fabian A. C. The obscured growth of massive black holes, 1999, Monthly Notices of the Royal Astronomical Society, 308, L39

Fabian A. C. Obscured Accretion and Black Holes, 2002, Issues in Unification of Active Galactic Nuclei, 258, 185

Fabian A. C. Observational Evidence of Active Galactic Nuclei Feedback, 2012, Annual Review of Astronomy and Astrophysics, 50, 455

Falcón-Barroso J., Sánchez-Blázquez P., Vazdekis A., Ricciardelli E., Cardiel N., Cenarro A. J., Gorgas J., Peletier R. F. An updated MILES stellar library and stellar population models, 2011, Astronomy & Astrophysics, 532, A95

Ferrarese L., Merritt D. A Fundamental Relation between Supermassive Black Holes and Their Host Galaxies, 2000, The Astrophysical Journal, 539, L9

Feruglio C., Maiolino R., Piconcelli E., Menci N., Aussel H., Lamastra A., Fiore F. Quasar feedback revealed by giant molecular outflows, 2010, Astronomy & Astrophysics, 518, L155

Fontanot F., 2010, in HUNTING FOR THE DARK: THE HIDDEN SIDE OF GALAXY FORMATION. Edited by Victor P. Debattista and Cristina C. Popescu AIP Conference Proceedings, INAF-OsservatorioAstronomico di Trieste, Italy, AIP, pp. 327–330

Forbes J. C., Krumholz M. R., Burkert A., Dekel A. Balance among gravitational instability, star formation and accretion determines the structure and evolution of disc galaxies, 2014, Monthly Notices of the Royal Astronomical Society, 438, 1552

Fossati M. et al. Hα3: an Hα imaging survey of HI selected galaxies from ALFALFA. IV. Structure of galaxies in the Local and Coma superclusters, 2013, Astronomy & Astrophysics, 553, A91

Franx M., van Dokkum P. G., Förster Schreiber N. M., Wuyts S., Labbé I., Toft S. Structure and Star Formation in Galaxies out to z = 3: Evidence for Surface Density Dependent Evolution and Upsizing, 2008, The Astrophysical Journal, 688, 770

Fraser C. W. Concentration indices of galaxies, 1972, The Observatory, 92, 51

Gadotti D. A. Structural properties of pseudo-bulges, classical bulges and elliptical galaxies: a Sloan Digital Sky Survey perspective, 2009, Monthly Notices of the Royal Astronomical Society, 393, 1531

Gammie C. F. Nonlinear Outcome of Gravitational Instability in Cooling, Gaseous Disks, 2001, The Astrophysical Journal, 553, 174

Gamow G. The Origin of Elements and the Separation of Galaxies, 1948, Physical Review, 74, 505

Gavazzi G., Fumagalli M., Fossati M., Galardo V., Grossetti F., Boselli A., Giovanelli R., Haynes M. P. Hα3: an Hα imaging survey of HI selected galaxies from ALFALFA. II. Star formation properties of galaxies in the Virgo cluster and surroundings, 2013, Astronomy & Astrophysics, 553, A89

Gebhardt K. et al. A Relationship between Nuclear Black Hole Mass and Galaxy Velocity Dispersion, 2000, The Astrophysical Journal, 539, L13

Genel S., Bouché N., Naab T., Sternberg A., Genzel R. The Growth of Dark Matter Halos: Evidence for Significant Smooth Accretion, 2010, The Astrophysical Journal, 719, 229

Genzel R. et al. Combined CO and Dust Scaling Relations of Depletion Time and Molecular Gas Fractions with Cosmic Time, Specific Star-formation Rate, and Stellar Mass, 2015, The Astrophysical Journal, 800, 20

Giavalisco M. et al. The Great Observatories Origins Deep Survey: Initial Results from Optical and Near-Infrared Imaging, 2004, The Astrophysical Journal, 600, L93

Gobat R. et al. Satellite content and quenching of star formation in galaxy groups at z ˜ 1.8, 2015, Astronomy & Astrophysics, 581, A56

Goddard D. et al. SDSS-IV MaNGA: stellar population gradients as a function of galaxy environment, 2017, Monthly Notices of the Royal Astronomical Society, 465, 688

Gómez P. L. et al. Galaxy Star Formation as a Function of Environment in the Early Data Release of the Sloan Digital Sky Survey, 2003, The Astrophysical Journal, 584, 210

Governato F. et al. Forming a large disc galaxy from a z ¡ 1 major merger, 2009, Monthly Notices of the Royal Astronomical Society, 398, 312

Graham A. W. Galaxy Bulges and Their Massive Black Holes: A Review, 2016, Galactic Bulges, 418, 263

Graham A. W., Scott N., Schombert J. M. Super-Massive Black Hole Mass Scaling Relations, 2015, Publications of The Korean Astronomical Society, 30, 335

Gültekin K. et al. The M-σ and M-L Relations in Galactic Bulges, and Determinations of Their Intrinsic Scatter, 2009, The Astrophysical Journal, 698, 198

Gunn J. E., Gott J. R. I. On the Infall of Matter Into Clusters of Galaxies and Some Effects on Their Evolution, 1972, Astrophysical Journal, 176, 1

Guo K., Zheng X. Z., Fu H. The Intrinsic Scatter along the Main Sequence of Star-forming Galaxies at z ˜ 0.7, 2013, The Astrophysical Journal, 778, 23

Guo K., Zheng X. Z., Wang T., Fu H. The Star-Formation Main Sequence: The Dependence of Specific Star Formation Rate and Its Dispersion on Galaxy Stellar Mass, 2015, arXiv.org, L49

Guo Q. et al. From dwarf spheroidals to cD galaxies: simulating the galaxy population in a ΛCDM cosmology, 2011, Monthly Notices of the Royal Astronomical Society, 413, 101

Guo Q., White S., Li C., Boylan-Kolchin M. How do galaxies populate Dark Matter halos?, 2009, arXiv.org, 1111

Guo Y. et al. Rest-frame UV-Optically Selected Galaxies at 2.3 ¡˜ z ¡˜ 3.5: Searching for Dusty Star-forming and Passively Evolving Galaxies, 2012, The Astrophysical Journal, 749, 149

Guth A. H. Inflationary universe: A possible solution to the horizon and flatness problems, 1981, Physical Review D (Particles and Fields), 23, 347

Guth A. H., Pi S. Y. Fluctuations in the new inflationary universe, 1982, Physical Review Letters, 49, 1110

Hansen S. M., Sheldon E. S., Wechsler R. H., Koester B. P. The Galaxy Content of SDSS Clusters and Groups, 2009, The Astrophysical Journal, 699, 1333

Häring N., Rix H.-W. On the Black Hole Mass-Bulge Mass Relation, 2004, The Astrophysical Journal, 604, L89

Harrison E. R. Galaxy formation in the early Universe, 1970, Monthly Notices of the Royal Astronomical Society, 148, 119

Heavens A., Panter B., Jimenez R., Dunlop J. The Complete Star Formation History of the Universe, 2004, arXiv.org, 625

Hensler G., Burkert A. The Initial Conditions of Proto-Galaxies - Constraints from Galactic Evolution, 1989, Cosmology and Gravitational Lensing. Workshop on Cosmology and Gravitational Lensing, 203

Hirschmann M., De Lucia G., Wilman D., Weinmann S., Iovino A., Cucciati O., Zibetti S., Villalobos Á. The influence of the environmental history on quenching star formation in a Λ cold dark matter universe, 2014, Monthly Notices of the Royal Astronomical Society, 444, 2938

Hogg D. W. et al. The Dependence on Environment of the Color-Magnitude Relation of Galaxies, 2004, The Astrophysical Journal, 601, L29

Hogg D. W. et al. The Overdensities of Galaxy Environments as a Function of Luminosity and Color, 2003, The Astrophysical Journal, 585, L5

Holmberg E. A photographic photometry of extragalactic nebulae., 1958, Lund Medd. Astron. Obs. Ser. II, 136, 1

Hopkins P. F., Bundy K., Hernquist L., Wuyts S., Cox T. J. Discriminating between the physical processes that drive spheroid size evolution, 2010, Monthly Notices of the Royal Astronomical Society, 401, 1099

Hopkins P. F., Hernquist L., Cox T. J., Di Matteo T., Robertson B., Springel V. A Unified, Merger-driven Model of the Origin of Starbursts, Quasars, the Cosmic X-Ray Background, Supermassive Black Holes, and Galaxy Spheroids, 2006a, The Astrophysical Journal Supplement Series, 163, 1

Hopkins P. F., Somerville R. S., Hernquist L., Cox T. J., Robertson B., Li Y. The Relation between Quasar and Merging Galaxy Luminosity Functions and the Merger-driven Star Formation History of the Universe, 2006b, The Astrophysical Journal, 652, 864

Hubble E., Humason M. L. The Velocity-Distance Relation among Extra-Galactic Nebulae, 1931, Astrophysical Journal, 74, 43

Huertas-Company M., Aguerri J. A. L., Bernardi M., Mei S., Sánchez Almeida J. Revisiting the Hubble sequence in the SDSS DR7 spectroscopic sample: a publicly available Bayesian automated classification, 2011, Astronomy & Astrophysics, 525, A157

Huertas-Company M. et al. A Catalog of Visual-like Morphologies in the 5 CANDELS Fields Using Deep Learning, 2015, The Astrophysical Journal Supplement Series, 221, 8

Humason M. L. Spectral Types of Faint Stars in Kapteyn's Selected Areas 1-115, 1932, Astrophysical Journal, 76, 224

Humason M. L. The Apparent Radial Velocities of 100 Extra-Galactic Nebulae, 1936, Astrophysical Journal, 83, 10

Ilbert O. et al. Evolution of the specific star formation rate function at z¡ 1.4 Dissecting the mass-SFR plane in COSMOS and GOODS, 2015, Astronomy & Astrophysics, 579, A2

Ilbert O. et al. Accurate photometric redshifts for the CFHT legacy survey calibrated using the VIMOS VLT deep survey, 2006, Astronomy & Astrophysics, 457, 841

Ilbert O. et al. Galaxy Stellar Mass Assembly between 0.2, 2009, arXiv.org, 644

Illingworth G. D. et al. The HST eXtreme Deep Field (XDF): Combining All ACS and WFC3/IR Data on the HUDF Region into the Deepest Field Ever, 2013, The Astrophysical Journal Supplement, 209, 6

Jorgensen I., Franx M., Kjaergaard P. Spectroscopy for E and S0 galaxies in nine clusters, 1995, Monthly Notices of the Royal Astronomical Society, 276, 1341

Kang Y., Kim Y.-L., Lim D., Chung C., Lee Y.-W. Early-type Host Galaxies of Type Ia Supernovae. I. Evidence for Downsizing, 2016, The Astrophysical Journal Supplement Series, 223, 7

Karim A. et al. The Star Formation History of Mass-selected Galaxies in the COSMOS Field, 2011, The Astrophysical Journal, 730, 61

Kauffmann G. et al. The dependence of star formation history and internal structure on stellar mass for 105 low-redshift galaxies, 2003, Monthly Notice of the Royal Astronomical Society, 341, 54

Kennicutt R. The History of Star Formation in Galaxies, 1992, Star Formation in Stellar Systems, 191

Kereš D. Galaxy Buildup by Gas Accretion, 2009, American Astronomical Society, 213, 313.06

Kereš D., Katz N., Weinberg D. H., Davé R. How do galaxies get their gas?, 2005, Monthly Notices of the Royal Astronomical Society, 363, 2

King A. R., Pounds K. A. Black hole winds, 2003, Monthly Notices of the Royal Astronomical Society, 345, 657

Knapp G. R., 1987, in IN: Structure and dynamics of elliptical galaxies; Proceedings of the IAU Symposium, Princeton University, NJ, pp. 145–153

Knapp G. R., Turner E. L., Cunniffe P. E. The statistical distribution of the neutral-hydrogen content of elliptical galaxies, 1985, Astronomical Journal (ISSN 0004-6256), 90, 454

Kormendy J. Brightness distributions in compact and normal galaxies. II - Structure parameters of the spheroidal component, 1977, Astrophysical Journal, 218, 333

Kormendy J., 1993, in Galactic bulges: proceedings of the 153rd Symposium of the International Astronomical Union held in Ghent, pp. 209–

Kormendy J. Secular Evolution in Disk Galaxies, 2013, Secular Evolution of Galaxies, 1

Kormendy J., Fisher D. B. Secular Evolution in Disk Galaxies: Pseudobulge Growth and the Formation of Spheroidal Galaxies, 2008, Formation and Evolution of Galaxy Disks ASP Conference Series, 396, 297

Kormendy J., Ho L. C. Coevolution (Or Not) of Supermassive Black Holes and Host Galaxies, 2013, Annual Review of Astronomy and Astrophysics, 51, 511

Kormendy J., Richstone D. Inward Bound—The Search For Supermassive Black Holes In Galactic Nuclei, 1995, Annual Review of Astronomy and Astrophysics, 33, 581

Kravtsov A., Vikhlinin A., Meshscheryakov A. Stellar mass – halo mass relation and star formation efficiency in high-mass halos, 2014, arXiv.org, arXiv:1401.7329

Kriek M., van Dokkum P. G., Franx M., Illingworth G. D., Magee D. K. The Hubble Sequence Beyond z = 2 for Massive Galaxies: Contrasting Large Star-forming and Compact Quiescent Galaxies, 2009, The Astrophysical Journal Letters, 705, L71

Kuntschner H. et al. The SAURON project - XVII. Stellar population analysis of the absorption line strength maps of 48 early-type galaxies, 2010, Monthly Notices of the Royal Astronomical Society, 408, 97

Lang P. et al. Bulge Growth and Quenching since z = 2.5 in CANDELS/3D-HST, 2014, The Astrophysical Journal, 788, 11

Larson R. B. Models for the formation of elliptical galaxies, 1975, Monthly Notices of the Royal Astronomical Society, 173, 671

Larson R. B., Tinsley B. M., Caldwell C. N. The evolution of disk galaxies and the origin of S0 galaxies, 1980, Astrophysical Journal, 237, 692

Law D. R., Steidel C. C., Erb D. K., Pettini M., Reddy N. A., Shapley A. E., Adelberger K. L., Simenc D. J. The Physical Nature of Rest-UV Galaxy Morphology during the Peak Epoch of Galaxy Formation, 2007, The Astrophysical Journal, 656, 1

Law D. R., Team M. Mapping Nearby Galaxies at APO: The MaNGA IFU Galaxy Survey, 2014, American Astronomical Society, 223, 254.31

Le Floch E., team t. M. A "UV+IR" history of star formation at 0¡z¡1, 2005, arXiv.org, arXiv:astro

Lee N. et al. Multi-Wavelength SEDs of Herschel Selected Galaxies in the COSMOS Field, 2013, arXiv.org, 131

Lee N., Team C. A Turn-over in the Galaxy Main Sequence of Star Formation at M* ˜ 1010 Msun, 2015, American Astronomical Society, 225, 329.03

Lees J. F., Knapp G. R., Rupen M. P., Phillips T. G. Molecular gas in elliptical galaxies, 1991, Astrophysical Journal, 379, 177

Leitner S. N. On the Last 10 Billion Years of Stellar Mass Growth in Star-forming Galaxies, 2012, The Astrophysical Journal, 745, 149

Lewis I. et al. The 2dF Galaxy Redshift Survey: the environmental dependence of galaxy star formation rates near clusters, 2002, Monthly Notices of the Royal Astronomical Society, 334, 673

Lilly S. J., Carollo C. M., Pipino A., Renzini A., Peng Y. Gas Regulation of Galaxies: The Evolution of the Cosmic Specific Star Formation Rate, the Metallicity-Mass-Star-formation Rate Relation, and the Stellar Content of Halos, 2013, The Astrophysical Journal, 772, 119

Lilly S. J., Le Fevre O., Hammer F., Crampton D. The CANADA-FRANCE REDSHIFT SURVEY XIII: The luminosity density and star-formation history of the Universe to z ˜ 1, 1996, arXiv.org, L1

Lin L. et al. Resolved star formation and molecular gas properties of green valley galaxies: a first look with ALMA and MaNGA, 2017, arXiv.org, arXiv:1710.08610

Lin L., Capak P., Laigle C., Ilbert O. Clustering analysis and large-scale environments of galaxies out to z˜3 in SPLASH, 2015, IAU General Assembly, 22, 2254579

Lintott C. et al. Galaxy Zoo 1: data release of morphological classifications for nearly 900 000 galaxies, 2011, Monthly Notices of the Royal Astronomical Society, 410, 166

Lintott C. J. et al. Galaxy Zoo : Morphologies derived from visual inspection of galaxies from the Sloan Digital Sky Survey, 2008, arXiv.org, 1179

Lotz J. M., Jonsson P., Cox T. J., Primack J. R. The effect of mass ratio on the morphology and time-scales of disc galaxy mergers, 2010, Monthly Notices of the Royal Astronomical Society, 404, 575

Lotz J. M., Primack J., Madau P. A New Nonparametric Approach to Galaxy Morphological Classification, 2004, The Astronomical Journal, 128, 163

Lutz D. et al. PACS Evolutionary Probe (PEP) - A Herschel key program, 2011, Astronomy & Astrophysics, 532, A90

Madau P., Dickinson M. Cosmic Star-Formation History, 2014, Annual Review of Astronomy and Astrophysics, 52, 415

Madau P., Ferguson H. C., Dickinson M. E., Giavalisco M., Steidel C. C., Fruchter A. High-redshift galaxies in the Hubble Deep Field: colour selection and star formation history to z˜4, 1996, Monthly Notices of the Royal Astronomical Society, 283, 1388

Magdis G. E. et al. KROSS: mapping the Hα emission across the star formation sequence at z $\approx$ 1, 2016, Monthly Notices of the Royal Astronomical Society, 456, 4533

Magdis G. E. et al. The Molecular Gas Content of z = 3 Lyman Break Galaxies: Evidence of a Non-evolving Gas Fraction in Main-sequence Galaxies at z ¿ 2, 2012, The Astrophysical Journal Letters, 758, L9

Magnelli B. et al. The deepest Herschel-PACS far-infrared survey: number counts and infrared luminosity functions from combined PEP/GOODS-H observations, 2013, Astronomy & Astrophysics, 553, A132

Magorrian J. et al. The Demography of Massive Dark Objects in Galaxy Centers, 1998, The Astronomical Journal, 115, 2285

Maier C. et al. The Dependence of Star Formation Activity on Stellar Mass Surface Density and Sersic Index in zCOSMOS Galaxies at 0.5 ¡ z ¡ 0.9 Compared with SDSS Galaxies at 0.04 ¡ z ¡ 0.08, 2009, The Astrophysical Journal, 694, 1099

Maragkoudakis A., Zezas A., Ashby M. L. N., Willner S. P. The sub-galactic and nuclear main sequences for local star-forming galaxies, 2017, Monthly Notices of the Royal Astronomical Society, 466, 1192

Marconi A., Hunt L. K. The Relation between Black Hole Mass, Bulge Mass, and Near-Infrared Luminosity, 2003, The Astrophysical Journal, 589, L21

Martig M., Bournaud F., Teyssier R., Dekel A. Morphological Quenching of Star Formation: Making Early-Type Galaxies Red, 2009, The Astrophysical Journal, 707, 250

Marulli F., Bonoli S., Branchini E., Gilli R., Moscardini L., Springel V. The spatial distribution of X-ray selected AGN in the Chandra deep fields: a theoretical perspective, 2009, Monthly Notices of the Royal Astronomical Society, 396, 1404

Masters K. L. et al. Galaxy Zoo: passive red spirals, 2010, Monthly Notices of the Royal Astronomical Society, 405, 783

McConnell N. J., Ma C.-P. Revisiting the Scaling Relations of Black Hole Masses and Host Galaxy Properties, 2013, The Astrophysical Journal, 764, 184

McLure R. J., Dunlop J. S. On the black hole-bulge mass relation in active and inactive galaxies, 2002, Monthly Notices of the Royal Astronomical Society, 331, 795

McNamara B. R., Nulsen P. E. J. Heating Hot Atmospheres with Active Galactic Nuclei, 2007, Annual Review of Astronomy and Astrophysics, 45, 117

Meier D. L., Sunyaev R. A. Primeval galaxies, 1979, Scientific American, 241, 130

Merritt D. Relaxation and tidal stripping in rich clusters of galaxies. II. Evolution of the luminosity distribution, 1984, Astrophysical Journal, 276, 26

Meurer G. R., Heckman T. M., Calzetti D. Dust Absorption and the Ultraviolet Luminosity Density at z ˜ 3 as Calibrated by Local Starburst Galaxies, 1999, The Astrophysical Journal, 521, 64

Mihos J. C., Harding P., Rudick C. S., Feldmeier J. J. Stellar Populations in the Outer Halo of the Massive Elliptical M49, 2013, The Astrophysical Journal Letters, 764, L20

Mitchell P. D., Lacey C. G., Cole S., Baugh C. M. The evolution of the star-forming sequence in hierarchical galaxy formation models, 2014, Monthly Notices of the Royal Astronomical Society, 444, 2637

Momcheva I. G., Team D.-H. S. Near-infrared Grism Spectroscopy with the Wide Field Camera 3: Insights from the 3D-HST Survey, 2016, American Astronomical Society, 227, 222.05

Moore B., Lake G., Katz N. Morphological Transformation from Galaxy Harassment, 1998, The Astrophysical Journal, 495, 139

Morgan W. W., 1961, in Proceedings of the National Academy of Sciences of the United States of America, Yerkes Observatory, University of Chicago, pp. 905–906

Morgan W. W., Mayall N. U. A Spectral Classification of Galaxies, 1957, Publications of the Astronomical Society of the Pacific, 69, 291

Morishita T., Ichikawa T. The Fate of a Red Nugget: In Situ Star Formation of Satellites around a Massive Compact Galaxy, 2016, The Astrophysical Journal, 816, 87

Morselli L., Popesso P., Erfanianfar G., Concas A. Bulges and discs in the local Universe. Linking the galaxy structure to star formation activity, 2017, Astronomy & Astrophysics, 597, A97

Muñoz J. A., Peeples M. S. A framework for empirical galaxy phenomenology: the scatter in galaxy ages and stellar metallicities, 2015, Monthly Notices of the Royal Astronomical Society, 448, 1430

Murray N., Quataert E., Thompson T. A. On the Maximum Luminosity of Galaxies and Their Central Black Holes: Feedback from Momentum-driven Winds, 2005, The Astrophysical Journal, 618, 569

Muzzin A. et al. The Evolution of the Stellar Mass Functions of Star-forming and Quiescent Galaxies to z = 4 from the COSMOS/UltraVISTA Survey, 2013, The Astrophysical Journal, 777, 18

Neistein E., van den Bosch F. C., Dekel A. Natural downsizing in hierarchical galaxy formation, 2006, Monthly Notices of the Royal Astronomical Society, 372, 933

Nelson E. J. et al. Where Stars Form: Inside-out Growth and Coherent Star Formation from HST Hα Maps of 3200 Galaxies across the Main Sequence at 0.7 ¡ z ¡ 1.5, 2016, The Astrophysical Journal, 828, 27

Nieto J. L. Early-type galaxies., 1988, Bol. Acad. Nac. Cienc. Cordoba, 58, 239

Noeske K. G. et al. Star Formation in AEGIS Field Galaxies since z=1.1: Staged Galaxy Formation and a Model of Mass-dependent Gas Exhaustion, 2007, The Astrophysical Journal, 660, L47

Noguchi M. Early Evolution of Disk Galaxies : Formation of Bulges in Clumpy Young Galactic Disks, 1998, arXiv.org, 77

Nolan L. A., Dunlop J. S., Panter B., Jimenez R., Heavens A., Smith G. The star formation histories of elliptical galaxies across the Fundamental Plane, 2007, Monthly Notices of the Royal Astronomical Society, 375, 371

Nulsen P. E. J. Transport processes and the stripping of cluster galaxies, 1982, Monthly Notices of the Royal Astronomical Society, 198, 1007

Oemler A. J. The Systematic Properties of Clusters of Galaxies. Photometry of 15 Clusters, 1974, Astrophysical Journal, 194, 1

Oesch P. A. et al. A Remarkably Luminous Galaxy at z=11.1 Measured with Hubble Space Telescope Grism Spectroscopy, 2016, arXiv.org, 129

Overzier R. A. et al. Dust Attenuation in UV-selected Starbursts at High Redshift and Their Local Counterparts: Implications for the Cosmic Star Formation Rate Density, 2011, The Astrophysical Journal Letters, 726, L7

Pannella M. et al. GOODS-Herschel: Star Formation, Dust Attenuation, and the FIR-radio Correlation on the Main Sequence of Star-forming Galaxies up to z $\simeq$4, 2015, The Astrophysical Journal, 807, 141

Pannella M., Hopp U., Saglia R. P., Bender R., Drory N., Salvato M., Gabasch A., Feulner G. The evolution of the mass function split by morphology up to redshift 1 in the FORS Deep and the GOODS-S Fields, 2006, arXiv.org, L1

Park C., Choi Y.-Y., Vogeley M. S., Gott J. R. I., Blanton M. R., Collaboration S. Environmental Dependence of Properties of Galaxies in the Sloan Digital Sky Survey, 2007, The Astrophysical Journal, 658, 898

Partridge R. B., Peebles P. J. E. Are Young Galaxies Visible?, 1967, Astrophysical Journal, 147, 868

Peacock J. A. Cosmological Physics, 1999, Cosmological Physics, 704

Pedlar A., Ghataure H. S., Davies R. D., Harrison B. A., Perley R., Crane, P. C., Unger S. W. The Radio Structure of NGC1275, 1990, Monthly Notices of the Royal Astronomical Society, 246, 477

Peebles P. J. E. The origin of galaxies and clusters of galaxies, 1984, Science (ISSN 0036-8075), 224, 1385

Peng C. Using GALFIT to Classify Galaxies at High-z: Measuring Asymmetry Parametrically, 2010, American Astronomical Society, 215, 229.09

Peng C. Y., Ho L. C., Impey C. D., Rix H.-W. Detailed Structural Decomposition of Galaxy Images, 2002, The Astronomical Journal, 124, 266

Peng Y., Maiolino R., Cochrane R. Strangulation as the primary mechanism for shutting down star formation in galaxies, 2015, Nature, 521, 192

Penzias A. A., Wilson R. W. A Measurement of Excess Antenna Temperature at 4080 Mc/s., 1965, Astrophysical Journal, 142, 419

Peterson J. R., Fabian A. C. X-ray spectroscopy of cooling clusters, 2006, Physics Reports, 427, 1

Planck Collaboration P. et al. Planck 2015 results. XIII. Cosmological parameters, 2015, arXiv.org, A13

Poggianti B. M. et al. The Relation between Star Formation, Morphology, and Local Density in High-Redshift Clusters and Groups, 2008, The Astrophysical Journal, 684, 888

Poggianti B. M. et al. Jellyfish Galaxy Candidates at Low Redshift, 2016, The Astronomical Journal, 151, 78

Postman M., Geller M. J. The morphology-density relation - The group connection, 1984, Astrophysical Journal, 281, 95

Pozzetti L. et al. zCOSMOS - 10k-bright spectroscopic sample. The bimodality in the Galaxy Stellar Mass Function: exploring its evolution with redshift, 2009, arXiv.org, A13

Press W. H., Schechter P. Formation of Galaxies and Clusters of Galaxies by Self-Similar Gravitational Condensation, 1974, Astrophysical Journal, 187, 425

Proctor R. N., Sansom A. E. A comparison of stellar populations in galaxy spheroids across a wide range of Hubble types, 2002, Monthly Notices of the Royal Astronomical Society, 333, 517

Querejeta M., Eliche-Moral M. C., Tapia T., Borlaff A., Rodríguez-Pérez C., Zamorano J., Gallego J. Formation of S0 galaxies through mergers. Bulge-disc structural coupling resulting from major mergers, 2015, Astronomy & Astrophysics, 573, A78

Ramos B. H. F. et al. Evolution of Galaxy Luminosity Function Using Photometric Redshifts, 2011, The Astronomical Journal, 142, 41

Reddy N. A., Steidel C. C., Fadda D., Yan L., Pettini M., Shapley A. E., Erb D. K., Adelberger K. L. Star Formation and Extinction in Redshift z˜2 Galaxies: Inferences from Spitzer MIPS Observations, 2006, arXiv.org, 792

Rees M. J., Ostriker J. P. Cooling, dynamics and fragmentation of massive gas clouds - Clues to the masses and radii of galaxies and clusters, 1977, Monthly Notices of the Royal Astronomical Society, 179, 541

Renzini A., Peng Y.-j. An Objective Definition for the Main Sequence of Star-forming Galaxies, 2015, The Astrophysical Journal Letters, 801, L29

Rizzo F., Fraternali F., Iorio G. S0 galaxies are faded spirals: clues from their angular momentum content, 2017, arXiv.org, arXiv:1711.10499

Robaina A. R., Hoyle B., Gallazzi A., Jimenez R., van der Wel A., Verde L. The similar stellar populations of quiescent spiral and elliptical galaxies, 2012, Monthly Notices of the Royal Astronomical Society, 427, 3006

Robert C Kennicutt J. Star Formation in Galaxies Along the Hubble Sequence, 1998, arXiv.org, 189

Roberts M. S., Haynes M. P. Physical Parameters along the Hubble Sequence, 1994, Annual Review of Astronomy and Astrophysics, 32, 115

Rodighiero G. et al. The Lesser Role of Starbursts in Star Formation at z = 2, 2011, The Astrophysical Journal Letters, 739, L40

Roediger E., Hensler G. Ram pressure stripping of disk galaxies. From high to low density environments, 2005, Astronomy & Astrophysics, 433, 875

Rudick C. S., Mihos J. C., Harding P., Feldmeier J. J., Janowiecki S., Morrison H. L. Optical Colors of Intracluster Light in the Virgo Cluster Core, 2010, The Astrophysical Journal, 720, 569

Sadler E. M., Gerhard O. E. How common are 'dust-lanes' in early-type galaxies?, 1985, Monthly Notices of the Royal Astronomical Society (ISSN 0035-8711), 214, 177

Saintonge A. et al. Molecular and atomic gas along and across the main sequence of star-forming galaxies, 2016, arXiv.org, 1749

Salim S. et al. UV Star Formation Rates in the Local Universe, 2007, The Astrophysical Journal Supplement Series, 173, 267

Salmi F., Daddi E., Elbaz D., Sargent M., Dickinson M., Renzini A., Bethermin M., Le Borgne D. Dissecting the stellar mass-SFR correlation in z=1 star-forming disk galaxies, 2012, arXiv.org, L14

Sánchez S. F. et al. CALIFA, the Calar Alto Legacy Integral Field Area survey. I. Survey presentation, 2012, Astronomy & Astrophysics, 538, A8

Sandage A. The Hubble Atlas of Galaxies, 1961, Washington: Carnegie Institution

Santini P. et al. The dust content of high-z submillimeter galaxies revealed by Herschel, 2010, Astronomy & Astrophysics, 518, L154

Sargent M. T. et al. Regularity Underlying Complexity: A Redshift-independent Description of the Continuous Variation of Galaxy-scale Molecular Gas Properties in the Mass-star Formation Rate Plane, 2014, The Astrophysical Journal, 793, 19

Scannapieco C., Gadotti D. A., Jonsson P., White S. D. M. An observer's view of simulated galaxies: disc-to-total ratios, bars and (pseudo-)bulges, 2010, Monthly Notices of the Royal Astronomical Society: Letters, 407, L41

Scarlata C. et al. COSMOS Morphological Classification with the Zurich Estimator of Structural Types (ZEST) and the Evolution Since z = 1 of the Luminosity Function of Early, Disk, and Irregular Galaxies, 2007, The Astrophysical Journal Supplement Series, 172, 406

Schawinski K. et al. The green valley is a red herring: Galaxy Zoo reveals two evolutionary pathways towards quenching of star formation in early- and late-type galaxies, 2014, Monthly Notices of the Royal Astronomical Society, 440, 889

Schiminovich D. et al. The GALEX-VVDS Measurement of the Evolution of the Far-Ultraviolet Luminosity Density and the Cosmic Star Formation Rate, 2005, The Astrophysical Journal, 619, L47

Schiminovich D. et al. The UV-Optical Color Magnitude Diagram. II. Physical Properties and Morphological Evolution On and Off of a Star-forming Sequence, 2007, The Astrophysical Journal Supplement Series, 173, 315

Schreiber C. et al. The Herschel view of the dominant mode of galaxy growth from z = 4 to the present day, 2015, Astronomy & Astrophysics, 575, A74

Schweizer F., 1987, in IN: Structure and dynamics of elliptical galaxies; Proceedings of the IAU Symposium, Carnegie Institution of Washington, Washington, DC, pp. 109–122

Scoville N. et al. ISM Masses and Star Formation at z = 1 to 6 ALMA Observations of Dust Continuum in 180 Galaxies in COSMOS, 2015, arXiv.org, arXiv:1505.02159

Seares F. H. Color Photographs of Nebul&aelig, 1916a, Publications of the Astronomical Society of the Pacific, 28, 123

Seares F. H., 1916b, in Proceedings of the National Academy of Sciences of the United States of America, Mount Wilson Solar Observatory, Carnegie Institution of Washington, pp. 553–557

Sersic J. L. Atlas de Galaxias Australes, 1968, Cordoba

Seth A. C., Dalcanton J. J., de Jong R. S. A Study of Edge-On Galaxies with the Hubble Space Telescope Advanced Camera for Surveys. I. Initial Results, 2005, The Astronomical Journal, 129, 1331

Shao L. et al. Star formation in AGN hosts in GOODS-N, 2010, Astronomy & Astrophysics, 518, L26

Shimasaku K. et al. Statistical Properties of Bright Galaxies in the Sloan Digital Sky Survey Photometric System, 2001, The Astronomical Journal, 122, 1238

Silk J. On the fragmentation of cosmic gas clouds. I - The formation of galaxies and the first generation of stars, 1977, Astrophysical Journal, 211, 638

Silk J., Rees M. J. Quasars and galaxy formation, 1998, Astronomy & Astrophysics, 331, L1

Silverman J. D. et al. A Higher Efficiency of Converting Gas to Stars Pushes Galaxies at z ˜ 1.6 Well Above the Star-forming Main Sequence, 2015, The Astrophysical Journal Letters, 812, L23

Simard L. GIM2D: an IRAF package for the Quantitative Morphology Analysis of Distant Galaxies, 1998, Astronomical Data Analysis Software and Systems VII, 145, 108

Simard L., Mendel J. T., Patton D. R., Ellison S. L., McConnachie A. W. A Catalog of Bulge+disk Decompositions and Updated Photometry for 1.12 Million Galaxies in the Sloan Digital Sky Survey, 2011, The Astrophysical Journal Supplement, 196, 11

Simard L. et al. The DEEP Groth Strip Survey. II. Hubble Space Telescope Structural Parameters of Galaxies in the Groth Strip, 2002, The Astrophysical Journal Supplement Series, 142, 1

Skelton R. E. et al. 3D-HST WFC3-selected Photometric Catalogs in the Five CANDELS/3D-HST Fields: Photometry, Photometric Redshifts, and Stellar Masses, 2014, The Astrophysical Journal Supplement Series, 214, 24

Skibba R. A. et al. Galaxy Zoo: disentangling the environmental dependence of morphology and colour, 2009, Monthly Notices of the Royal Astronomical Society, 399, 966

Skibba R. A., Sheth R. K. A halo model of galaxy colours and clustering in the Sloan Digital Sky Survey, 2009, Monthly Notices of the Royal Astronomical Society, 392, 1080

Smethurst R. J. et al. Galaxy Zoo: evidence for diverse star formation histories through the green valley, 2015, Monthly Notices of the Royal Astronomical Society, 450, 435

Smith S. Some Notes on the Structure of Elliptical Nebulae, 1935, Astrophysical Journal, 82, 192

Sodré Jr L., da Silva A. R., Santos W. A. The nature of extremely red galaxies in the local universe, 2013, arXiv.org, 2503

Sparre M. et al. The star formation main sequence and stellar mass assembly of galaxies in the Illustris simulation, 2015, Monthly Notices of the Royal Astronomical Society, 447, 3548

Speagle J. S., Steinhardt C. L., Capak P. L., Silverman J. D. A Highly Consistent Framework for the Evolution of the Star-Forming ”Main Sequence” from z˜0-6, 2014, arXiv.org, 15

Spindler A. et al. SDSS-IV MaNGA: The Spatial Distribution of Star Formation and its Dependence on Mass, Structure and Environment, 2017, arXiv.org, arXiv:1710.05049

Strateva I. et al. Color Separation of Galaxy Types in the Sloan Digital Sky Survey Imaging Data, 2001, The Astronomical Journal, 122, 1861

Strauss M. A. et al. Spectroscopic Target Selection in the Sloan Digital Sky Survey: The Main Galaxy Sample, 2002, The Astronomical Journal, 124, 1810

Tabor G., Binney J. Elliptical Galaxy Cooling Flows Without Mass Drop-Out, 1993, Monthly Notices of the Royal Astronomical Society, 263, 323

Tacchella S. et al. Dust attenuation, bulge formation and inside-out cessation of star-formation in Star-Forming Main Sequence galaxies at z˜2, 2017, arXiv.org, arXiv:1704.00733

Tacchella S. et al. Evidence for mature bulges and an inside-out quenching phase 3 billion years after the Big Bang, 2015a, Science, 348, 314

Tacchella S., Dekel A., Carollo C. M., Ceverino D., DeGraf C., Lapiner S., Mandelker N., Primack J. R. The Confinement of Star-Forming Galaxies into a Main Sequence through Episodes of Gas Compaction, Depletion, and Replenishment, 2015b, arXiv.org, 2790

Tacchella S., Dekel A., Carollo C. M., Ceverino D., DeGraf C., Lapiner S., Mandelker N., Primack J. R. Evolution of density profiles in high-z galaxies: compaction and quenching inside-out, 2016, Monthly Notices of the Royal Astronomical Society, 458, 242

Tacchella S. et al. SINS/zC-SINF Survey of z ˜ 2 Galaxy Kinematics: Rest-frame Morphology, Structure, and Colors from Near-infrared Hubble Space Telescope Imaging, 2015c, The Astrophysical Journal, 802, 101

Tacchella S., Trenti M., Carollo C. M. A Physical Model for the 0 ¡˜ z ¡˜ 8 Redshift Evolution of the Galaxy Ultraviolet Luminosity and Stellar Mass Functions, 2013, The Astrophysical Journal Letters, 768, L37

Tal T., van Dokkum P. G., Franx M., Leja J., Wake D. A., Whitaker K. E. Galaxy Environments over Cosmic Time: The Non-evolving Radial Galaxy Distributions around Massive Galaxies since z = 1.6, 2013, The Astrophysical Journal, 769, 31

Tegmark M., Silk J., Rees M. J., Blanchard A., Abel T., Palla F. How Small Were the First Cosmological Objects?, 1997, Astrophysical Journal v.474, 474, 1

Tempel E., Saar E., Liivamägi L. J., Tamm A., Einasto J., Einasto M., Müller V. Galaxy morphology, luminosity, and environment in the SDSS DR7, 2011, Astronomy & Astrophysics, 529, A53

Terrazas B. A., Bell E. F., Woo J., Henriques B. M. B. Supermassive Black Holes as the Regulators of Star Formation in Central Galaxies, 2017, The Astrophysical Journal, 844, 170

Thomas D., Davies R. L. Rejuvenation of spiral bulges, 2006, Monthly Notices of the Royal Astronomical Society, 366, 510

Tojeiro R. et al. The different star formation histories of blue and red spiral and elliptical galaxies, 2013, Monthly Notices of the Royal Astronomical Society, 432, 359

Toomre A. Theories of spiral structure, 1977, In: Annual review of astronomy and astrophysics. Volume 15. (A78-16576 04-90) Palo Alto, 15, 437

Torrey P., Vogelsberger M., Genel S., Sijacki D., Springel V., Hernquist L. A model for cosmological simulations of galaxy formation physics: multi-epoch validation, 2014, Monthly Notices of the Royal Astronomical Society, 438, 1985

Tremaine S. et al. The Slope of the Black Hole Mass versus Velocity Dispersion Correlation, 2002, The Astrophysical Journal, 574, 740

Trujillo I., Graham A. W., Caon N. On the estimation of galaxy structural parameters: the Sérsic model, 2001, Monthly Notices of the Royal Astronomical Society, 326, 869

van der Wel A. The Dependence of Galaxy Morphology and Structure on Environment and Stellar Mass, 2008, The Astrophysical Journal Letters, 675, L13

van der Wel A. et al. Structural Parameters of Galaxies in CANDELS, 2012, The Astrophysical Journal Supplement, 203, 24

van der Wel A., Bell E. F., Holden B. P., Skibba R. A., Rix H.-W. The Physical Origins of the Morphology-Density Relation: Evidence for Gas Stripping from the Sloan Digital Sky Survey, 2010, The Astrophysical Journal, 714, 1779

Villalobos Á., De Lucia G., Borgani S., Murante G. Simulating the evolution of disc galaxies in a group environment - I. The influence of the global tidal field, 2012, Monthly Notices of the Royal Astronomical Society, 424, 2401

Vogelsberger M., Genel S., Sijacki D., Torrey P., Springel V., Hernquist L. A model for cosmological simulations of galaxy formation physics, 2013, Monthly Notices of the Royal Astronomical Society, 436, 3031

Vogt N. P., Haynes M. P., Giovanelli R., Herter T. M/L, Hα Rotation Curves, and H I Gas Measurements for 329 Nearby Cluster and Field Spirals. III. Evolution in Fundamental Galaxy Parameters, 2004, The Astronomical Journal, 127, 3325

Wang J. et al. An observational and theoretical view of the radial distribution of H I gas in galaxies, 2014, Monthly Notices of the Royal Astronomical Society, 441, 2159

Weinzirl T., Jogee S., Khochfar S., Burkert A., Kormendy J. Bulge n and B/T in High-Mass Galaxies: Constraints on the Origin of Bulges in Hierarchical Models, 2009, The Astrophysical Journal, 696, 411

Welikala N., Connolly A. J., Hopkins A. M., Scranton R., Conti A. Spatially Resolved Galaxy Star Formation and Its Environmental Dependence. I., 2008, The Astrophysical Journal, 677, 970

Whitaker K. E. et al. Constraining the Low-mass Slope of the Star Formation Sequence at 0.5 ¡ z ¡ 2.5, 2014, The Astrophysical Journal, 795, 104

Whitaker K. E., van Dokkum P. G., Brammer G., Franx M. The Star Formation Mass Sequence Out to z = 2.5, 2012, The Astrophysical Journal Letters, 754, L29

White S. D. M., Rees M. J. Core condensation in heavy halos - A two-stage theory for galaxy formation and clustering, 1978, Monthly Notices of the Royal Astronomical Society, 183, 341

Wijesinghe D. B., Hopkins A. M., Kelly B. C., Welikala N., Connolly A. J. Morphological classification of galaxies and its relation to physical properties, 2010, Monthly Notices of the Royal Astronomical Society, 404, 2077

Willett K., Lintott C. J., Bamford S. P., Masters K. L., Simmons B., Fortson L., Schawinski K., Simpson R. Galaxy Zoo 2: A Detailed Morphological Catalog of 295,000 Galaxies from SDSS, 2013, American Astronomical Society, 221

Willett K. W. et al. Galaxy Zoo: the dependence of the star formation-stellar mass relation on spiral disk morphology, 2015, arXiv.org, 820

Williams R. J., Quadri R. F., Franx M., van Dokkum P., Toft S., Kriek M., Labbé I. The Evolving Relations Between Size, Mass, Surface Density, and Star Formation in 3 x 10^4 Galaxies Since z = 2, 2010, The Astrophysical Journal, 713, 738

Wuyts S. et al. A CANDELS-3D-HST synergy: Resolved Star Formation Patterns at 0.7 ¡ z ¡ 1.5, 2013, The Astrophysical Journal, 779, 135

Wuyts S. et al. Galaxy Structure and Mode of Star Formation in the SFR-Mass Plane from z ˜ 2.5 to z ˜ 0.1, 2011a, The Astrophysical Journal, 742, 96

Wuyts S. et al. On Star Formation Rates and Star Formation Histories of Galaxies out to z ˜ 3, 2011b, arXiv.org, 106

Xia L., Zhou X., Yang Y., Ma J., Jiang Z. Evolution of the Galaxy Luminosity Function for Redshift and Density Environment at 0.03 ¡ z ¡ 0.5, 2006, The Astrophysical Journal, 652, 249

Yang X., Mo H. J., van den Bosch F. C. Galaxy Groups in the SDSS DR4. III. The Luminosity and Stellar Mass Functions, 2009, The Astrophysical Journal, 695, 900

Yang X., Mo H. J., van den Bosch F. C., Jing Y. P. A halo-based galaxy group finder: calibration and application to the 2dFGRS, 2005, Monthly Notices of the Royal Astronomical Society, 356, 1293

Yang X., Mo H. J., van den Bosch F. C., Pasquali A., Li C., Barden M. Galaxy Groups in the SDSS DR4. I. The Catalog and Basic Properties, 2007, The Astrophysical Journal, 671, 153

Yang X., Mo H. J., van den Bosch F. C., Zhang Y., Han J. Evolution of the Galaxy-Dark Matter Connection and the Assembly of Galaxies in Dark Matter Halos, 2012, The Astrophysical Journal, 752, 41

Zandivarez A., Martínez H. J., Merchán M. E. On the Luminosity Function of Galaxies in Groups in the Sloan Digital Sky Survey, 2006, The Astrophysical Journal, 650, 137

Zeldovich Y. B. A hypothesis, unifying the structure and the entropy of the Universe, 1972, Monthly Notices of the Royal Astronomical Society, 160, 1P

Zibetti S. Introducing ADAPTSMOOTH, a new code for the adaptive smoothing of astronomical images, 2009, arXiv.org, arXiv:0911.4956

Ziparo F. et al. The lack of star formation gradients in galaxy groups up to z ~ 1.6, 2013, Monthly Notices of the Royal Astronomical Society, 434, 3089

Zolotov A. et al. Compaction and quenching of high-z galaxies in cosmological simulations: blue and red nuggets, 2015, Monthly Notices of the Royal Astronomical Society, 450, 2327

Zwicky F. Clusters of Nebulae, 1942, Publications of the Astronomical Society of the Pacific, 54, 185